Improved Coherency-based Dynamic Equivalents

by

Feng Ma

A Dissertation Presented in Partial Fulfillment
of the Requirements for the Degree
Doctor of Philosophy

Approved October 2011 by the
Graduate Supervisory Committee:

Vijay Vittal, Chair
Daniel Tylavsky
Gerald Heydt
Jennie Si
Raja Ayyanar

ARIZONA STATE UNIVERSITY

December 2011

ABSTRACT

Due to restructuring and open access to the transmission system, modern electric power systems are being operated closer to their operational limits. Additionally, the secure operational limits of modern power systems have become increasingly difficult to evaluate as the scale of the network and the number of transactions between utilities increase. To account for these challenges associated with the rapid expansion of electric power systems, dynamic equivalents have been widely applied for the purpose of reducing the computational effort of simulation-based transient security assessment.

Dynamic equivalents are commonly developed using a coherency-based approach in which a retained area and an external area are first demarcated. Then the coherent generators in the external area are aggregated and replaced by equivalenced models, followed by network reduction and load aggregation. In this process, an improperly defined retained area can result in detrimental impacts on the effectiveness of the equivalents in preserving the dynamic characteristics of the original unreduced system.

In this dissertation, a comprehensive approach has been proposed to determine an appropriate retained area boundary by including the critical generators in the external area that are tightly coupled with the initial retained area. Furthermore, a systematic approach has also been investigated to efficiently predict the variation in generator slow coherency behavior when the system operating condition is subject to change. Based on this determination, the critical generators in the external area that are tightly coherent with the generators in the

initial retained area are retained, resulting in a new retained area boundary. Finally, a novel hybrid dynamic equivalent, consisting of both a coherency-based equivalent and an artificial neural network (ANN)-based equivalent, has been proposed and analyzed. The ANN-based equivalent complements the coherency-based equivalent at all the retained area boundary buses, and it is designed to compensate for the discrepancy between the full system and the conventional coherency-based equivalent. The approaches developed have been validated on a large portion of the Western Electricity Coordinating Council (WECC) system and on a test case including a significant portion of the eastern interconnection.

.

This dissertation is dedicated to my wife, Le Zheng, for her endless love and support and to my parents, Yunzhong Ma and Aimei Liu, for always being there for me.

ACKNOWLEDGMENTS

Firstly, I would like to express my grateful thanks to my advisor, Dr. Vijay Vittal for his tremendous academic guidance and encouragement throughout this work. I am always impressed by his great insight and dedication to perfection.

I am grateful to the members of my committee, Dr. Daniel Tylavsky, Dr. Gerald Heydt, Dr. Jennie Si, and Dr. Raja Ayyanar, for their valuable suggestions and comments.

I would also like to express my gratitude to the Power Systems Engineering Research Center (PSERC) and it industry members for the financial supports provided. My specific thanks go to Dr. Eugene Litvinov, Dr. Xioachuan Luo, and Dr. Slava Maslennikov at ISO New England Inc. for providing me with the opportunity to continue my research as a summer intern in 2010.

Last but not least, I would like to thank all my friends in the Power and Energy Engineering Group at Arizona State University. The joyful days we spent together made my life colorful and meaningful.

TABLE OF CONTENTS

CHAPTER Page

CHAPTER Page

LIST OF TABLES

LIST OF FIGURES

Figure Page

Figure Page

NOMENCLATURE

a_i	Rotor acceleration rate of generator i
a_{opt}	Optimal step length in the corrector step
b_{ij}	Primitive susceptance of the line from bus i to bus j
b_k	Bias of the k^{th} neuron
c_{ij}	Half line charging susceptance of the line from bus i to bus j
d_{ij}	Slow coherency index between generator i and generator j
g_{ij}	Primitive conductance of the line from bus i to bus j
m_i	Mean value of the i^{th} Gaussian distribution function
n_f	Time instant until which the responses are compared
n_g	Total number of generators
n_t	Total number of buses
p_{ki}	Participation factor of the k^{th} state variable in the i^{th} mode
t_f	Fault duration time
u_k	Summing junction output of the k^{th} neuron
w_{ki}	Weight from the i^{th} input to the k^{th} neuron
x_i	The i^{th} input of a neuron
x_{ij}	Primitive reactance of the line from bus i to bus j
x'_{di}	Transient reactance of generator i
y_{ij}	Primitive line admittance of the line from bus i to bus j
y_k	Output of the k^{th} neuron
$\mathbf{b}(i)$	Bias vector at the i^{th} layer of a neural network
$\mathbf{e}^k$	Prediction error at the k^{th} iteration

$\mathbf{f}$	Vector of differential equations of component dynamics
$\mathbf{f}_{\mathbf{x}}$	Partial derivative matrix of **f** with respect to **x**
$\mathbf{f}_{\mathbf{y}}$	Partial derivative matrix of **f** with respect to **y**
$\mathbf{f}_{\beta}$	Sensitivity vector of **f** with respect to β
$\mathbf{f}'_n$	Sensitivity vector of **f** with respect to $P_{ANNj,n}$ at the time instant n
$\mathbf{g}$	Vector of algebraic equations representing power flow equations
$\mathbf{g}_{\mathbf{x}}$	Partial derivative matrix of **g** with respect to **x**
$\mathbf{g}_{\mathbf{y}}$	Partial derivative matrix of **g** with respect to **y**
$\mathbf{g}_{\beta}$	Sensitivity vector of **g** with respect to β
$\mathbf{g}'_n$	Sensitivity vector of **g** with respect to $P_{ANNj,n}$ at the time instant n
$\mathbf{h}$	Vector of nonlinear functions representing the input-and-output mapping
$\mathbf{h}'$	Vector of simplified nonlinear functions based on **h**
$\mathbf{w}^k$	Matrix of neural network adjustable weights at the k^{th} iteration
$\mathbf{x}$	Vector of system state variables
$\mathbf{x}_n$	Vector of system state variables at the time instant n
$\mathbf{x}_n^{new}$	Vector of approximated **x** for new system parameters at the time instant n
$\mathbf{x}_{\beta,n}$	Sensitivity vector of **x** with respect to β at the time instant n
$\mathbf{x}'_n$	Sensitivity vector of **x** with respect to $P_{ANNj,n}$ at the time instant n
$\mathbf{y}$	Vector of system algebraic variables
$\mathbf{y}_n$	Vector of system algebraic variables at the time instant n
$\mathbf{y}_n^{new}$	Vector of **y** for new system parameters at the time instant n

$\mathbf{y}_{\beta,n}$	Sensitivity vector of $\mathbf{y}$ with respect to β at the time instant n
$\mathbf{y}'_n$	Sensitivity vector of $\mathbf{y}$ with respect to $P_{ANNj,n}$ at the time instant n
B	Set consisting of retained area boundary buses
B_{ij}	Imaginary part of the (i,j) element in the system admittance matrix
D_i	Damping coefficient of generator i
E_i	Voltage behind the transient reactance of generator i
E^k	Total cost function at the k^{th} iteration
G_{ij}	Real part of the (i,j) element in the system admittance matrix
H_{i}	Inertia constant of generator i
K_G	Set of dispatchable generators
K_L	Set of load buses subjected to changes
M_i	Inertia of generator i
$P_{ANNi,n}$	Active power injection of the ANN-based equivalent at bus i at the time instant n
$P'_{ANNi,n}$	Pre-processed $P_{ANNi,n}$
P_{Gi}	Electrical output power of generator i
P_{ij}	Active power flow over the line from bus i to bus j
P_{mi}	Mechanical input power of generator i
$PTDF_g^{ij}$	Power transfer distribution factor of generator g with respect to the line from bus i to bus j
$Q_{ANNi,n}$	Reactive power injection of the ANN-based equivalent at bus i at the time instant n
$Q'_{ANNi,n}$	Pre-processed $Q_{ANNi,n}$

Q_{Gi}	Reactive power output of generator *i*
T	Simulation duration time
$V_{ANNi,n}$	Voltage magnitude at bus *i* that is connected to the ANN-based equivalent at the time instant *n*
$V'_{ANNi,n}$	Pre-processed $V_{ANNi,n}$
V_i	Voltage magnitude at bus *i*
$\mathbf{A}_{sys}$	System state matrix
B	Node susceptance matrix in the DC power flow
D	Diagonal generator damping coefficient matrix
$\mathbf{H}^k$	Approximated the Hessian matrix of the total cost function at k^{th} iteration
$\mathbf{J}_{pf}$	Jacobian matrix in power flow computation
K	Synchronizing power coefficient matrix
M	Diagonal generator inertia coefficient matrix
$\mathbf{M}_{Gi}$	Vector with 1 at the entry of generator *i* and zeros elsewhere
$\mathbf{M}_l$	Vector of node-branch incidence
$\mathbf{M}_{PLi}$	Vector with 1 at the entry of load bus *i* and zeros elsewhere
$\mathbf{M}_{QLi}$	Vector with 1 at the entry of load bus *i* and zeros elsewhere
P	Vector of active power injection
Q	Vector of reactive power injection
S	Inverse of Jacobian matrix in AC power flow
$\mathbf{S}_{ANN,n}$	Power injection vector of the ANN-based equivalent at the time instant *n*

$\mathbf{V}$	Vector of voltage magnitude
$\mathbf{V}_{fi,n}$	Complex voltage at bus i in the full system at the time instant n
$\mathbf{V}_{ri,n}$	Complex voltage at bus i in the reduced system at the time instant n
$\mathbf{W}(i)$	Weight matrix at the i^{th} layer of a neural network
$\mathbf{Y}$	Full system admittance matrix augmented with the generator transient reactances
$\mathbf{Y}_A$	Self-admittance matrix for generator internal buses
$\mathbf{Y}_B$	Mutual admittance matrix between generator internal buses and external network buses
$\mathbf{Y}_C$	Mutual admittance matrix between external network buses and generator internal buses
$\mathbf{Y}_D$	Self-admittance matrix for external network buses
$\mathbf{Y}_{red}$	System admittance matrix reduced to generator internal buses
AI	Artificial intelligent
ANN	Artificial neural network
ATC	Available transfer capability
DAE	Differential algebraic equation
DSA	Dynamic security assessment
DYNRED	Dynamic reduction program
FRNN	Fully recurrent neural network
ISO	Independent system operator
ISO-NE	ISO-New England

LM	Levenberg-Marquardt training algorithm
LRNN	Locally recurrent neural network
MLP	Multilayer perceptron-based neural network
MSE	Mean square error
NB	New Brunswick
NR	Newton-Raphson
NS	Nova Scotia
NYISO	New York ISO
PI	Performance index for equivalencing accuracy evaluation
PMU	Synchronized phasor measurement unit
PSAT	Power system analysis toolbox
PSS	Power system stabilizer
PTDF	Power transfer distribution factor
RBF	Radial basis function-based neural network
RMSE	Root mean square error
SSAT	Small signal analysis tool
TSAT	Transient stability analysis tool
UTD	Unit time delay
WECC	Western Electricity Coordinating Council
β	System parameter subject to change
β_0	Initial value of the system parameter
δ_i	Rotor angle of generator i
η	Learning rate in backpropagation training algorithm

$\theta_{ANNi,n}$	Voltage phase angle at bus i that is connected to the ANN-based equivalent at the time instant n
$\theta'_{ANNi,n}$	Pre-processed $\theta_{ANNi,n}$
θ_i	Voltage phase angle at bus i
λ_i	Eigenvalue of the i^{th} mode
μ_i	Step in Levenberg-Marquardt training algorithm at the i^{th} iteration
σ_i^2	Variance of the i^{th} Gaussian basis function
ϕ_i	Activation function at the i^{th} layer of a neural network
ϕ_{ki}	The k^{th} element of the i^{th} right eigenvector
ψ_{ki}	The k^{th} element of the i^{th} left eigenvector
ω_i	Rotor speed of generator i (p.u.)
ω_R	Base frequency (376.99 rad/s)
ω_0	Initial value of the rotor speed of generator i (p.u.)
$\boldsymbol{\upsilon}_i$	Row of right eigenvector matrix corresponding to the rotor angle state of generator i
$\boldsymbol{\delta}$	Vector of generator rotor angle
$\boldsymbol{\theta}$	Vector of voltage phase angle
$\boldsymbol{\xi}$	Vector of initial value of the states
$\boldsymbol{\phi}_i$	Right eigenvector corresponding to the i^{th} mode
$\boldsymbol{\psi}_i$	Left eigenvector corresponding to the i^{th} mode
$\boldsymbol{\Phi}$	Matrix consisting of the right eigenvector of the modes of interest
$\boldsymbol{\omega}$	Vector of generator speed
Δt	Integration time step

$\Delta\mathbf{G}$	Vector of eigensolution estimation error
$()^{H}$	Conjugate transpose
$\|\|\ \|\|$	2-norm of a complex vector

Chapter 1

INTRODUCTION

With the evolution of heavily interconnected power systems, it has become computationally burdensome to represent the entire system in detail and to conduct numerous transient stability studies [1]. This is especially true for on-line power system transient stability assessment since there is a strict limitation on the size of the system that can be simulated in a near real-time setting. In addition, the generation, transmission, and distribution facilities can belong to different owners in the restructured environment [2]. This situation makes it difficult for a single entity to access detailed information about the network and equipment models within the entire system. Therefore, it is necessary to construct a reduced order system which preserves the dynamic property of the specific system that is of interest. To account for these challenges, power system dynamic equivalent techniques have been receiving renewed attention recently and have been widely implemented for the purpose of reducing the computational effort of simulation-based transient stability assessment of large-scale interconnected power systems.

1.1 Coherency-based Dynamic Equivalent

As shown in Fig. 1.1, three areas are commonly defined in the process of building a dynamic equivalent:

- *Study Area*: the core subsystem that is of direct interest and therefore must be retained in detail. For the reduced system to effectively represent the behavior of the full system, the power flow and dynamic responses in this area are supposed to be the same as in the full system representation.

- *Buffer Area*: the area that is geographically or electrically close to the retained area. It has significant impact on the study area due to its tight coupling with the study area. For better equivalencing accuracy, this area along with its component models is retained in detail.
- *External Area*: this is the portion of the original full system in which detailed information regarding the system responses is not required and the models can be replaced by proper equivalent models.

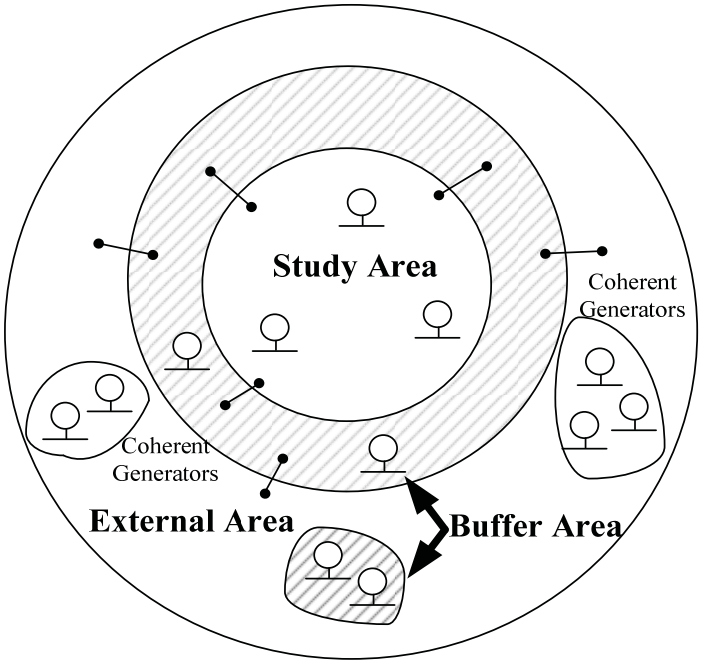

Fig. 1.1 Definition of study, buffer, and external areas.

For practical implementation, all the models in the study area and buffer area are retained; therefore both areas are denoted as the retained area in this dissertation. After the dynamic equivalent process is completed, the system consisting of both the retained area and equivalenced external area is denoted as the reduced system.

In the literature, coherency-based dynamic equivalents have been extensively investigated. The basic idea is to aggregate the generators in the external area that present similar dynamic characteristics. The extent of the similarity is measured by generator coherency. For example, if two generators present similar rotor angle responses following a system disturbance, they are tightly coherent. Otherwise, they are weakly coherent. To evaluate the generator coherency, a variety of methods have been proposed. The most intuitive approach is to compare the generator responses following certain system disturbances. Based on this idea, the authors in [3] proposed a linear simulation method. Specifically, two generators are considered to be tightly coherent when the maximum deviation of their rotor angle responses subject to a given disturbance is smaller than a specified threshold value. Although the classical generator models are used, the simulation-based method is still time-consuming if different system disturbances need to be studied. The weak-link method was firstly introduced in [4]. Unlike the linear simulation method, it directly measures the coupling of generators based on the system state matrix. A group of generators are considered to be tightly coherent if the coupling coefficients in the system state matrix among them are high [5]. In [6], the slow coherency (or two-time scale) technique based on singular perturbation theory was used to separate the slow and fast dynamics in large power systems to identify the coherent generators from the perspective of a slow dynamic process. As a simplified realization of the slow coherency method, the generator coherency was evaluated based on the similarity of their mode shapes associated with a set of specific slow modes within the system in [7]. A

recent study revealed that the excitation system can also exert impact on the generator coherency evaluation. Therefore the related index based on a detailed generator model was discussed in [8]. However, the improvement is relatively small considering the additional computational efforts that are required.

To build the equivalenced model for the external area, coherent generator aggregation and network reduction are applied sequentially. A typical procedure for aggregating a group of coherent generators is presented in Fig. 1.2.

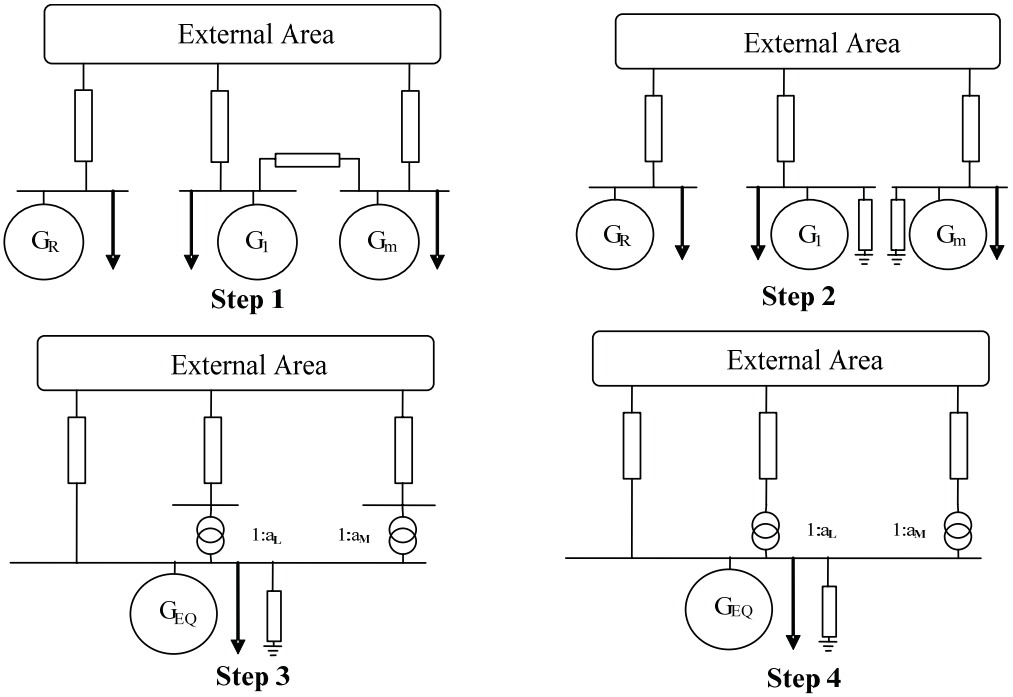

Fig. 1.2 Coherent generator aggregation.

In the procedure as shown in Fig. 1.2, the generator in a coherent group that has the largest capacity is chosen as the reference generator in Step 1, and the equivalent generator to be built will be placed at this bus. In Step 2, the branches among the coherent generators are replaced by equivalent shunts. In Step 3, all

coherent generator terminal buses, expect for the reference generator, are connected to the reference bus through the ideal phase-shifting transformers. In addition, the generation and load at each generator bus are also transferred to the reference bus. In the final step, all generator terminal buses are eliminated.

In Fig. 1.2, the parameters of the equivalent generator are aggregated from the individual generators that belong to the same coherent group. In the literature, the frequency-domain method [9] and the structure preserving method [10] have been proposed. When forming the equivalent generators modeled using detailed representation, however, these methods might lead to problematic parameters in certain cases. Therefore the classical aggregation method [11] is commonly used in practical applications. Specifically, the equivalent generator is represented using a classical model. Its inertia is the sum of individual generator inertias, and its transient reactance is the parallel combination of individual transient reactances. The equivalenced damping factor is determined based on the user-defined ratio of damping (D) to inertia (H).

The final step in building an equivalent system is to reduce the network within the external area. During this process, the load buses area are eliminated using Gaussian elimination, and the loads connected to the same bus are aggregated and replaced by appropriate equivalent load models.

1.2 Dynamic Reduction Program (DYNRED)

Consisting of a wide range of coherent generator identification, network reduction, and generator aggregation options, DYNRED has been developed and implemented successfully in various applications [12]-[14]. Recently, sponsored

by several independent system operators (ISOs) and utilities, DYNRED has been updated by the Electric Power Research Institute (EPRI) in an effort to incorporate the dynamic equivalencing technique into the on-line Dynamic Security Assessment (DSA) system. In this update, the following new features are provided:

- new graphical user interface
- enhancements of models supported (PTI PSS/E models and data formats in version 29 and 30)
- removal of some specific approaches (e.g. two time-scales and singular perturbation method and detailed generator aggregation method)
- new performance metrics for model validations (e.g. power flow, time-domain simulation, and small signal analysis).

1.3 Artificial Neural Network (ANN)

As one of the artificial intelligent (AI) methods, artificial neural network (ANN) has been investigated extensively since the 1980s. A neural network is a system with inputs and outputs and is composed of many simple processing units called neurons. Each neuron has a number of internal parameters called weights and biases. By adjusting these parameters, the behavior of the entire neural network can be modified. Theoretically, an ANN with appropriate structure can approximate any nonlinear function, and therefore they have the potential to solve many problems that cannot be handled well by traditional analytical approaches. The main advantages of the neural network method include:

- A neural network with an appropriate structure has the ability to approximate

arbitrary nonlinear mappings from input signals to output signals.

- A properly trained network has the ability to generalize the input-and-output mappings with the presence of the inputs that are not encountered during the learning procedure.
- A neural network inherently has a highly parallel structure. This feature makes neural networks ideally suited for parallel processing.

However, the following limitations of neural networks also need to be noted:

- There is no systematic approach to determine appropriate neural network structures for different applications. Instead, the trial-and-error method is usually needed in determining the number of layers to be used and the number of neurons to be included at each layer.
- For a neural network to be properly trained, sufficient training patterns need to be provided. The computational time for network training could become significantly long when a complex network structure is used.
- Neural networks inherently have a black box characteristic. Therefore, it is difficult to interpret the information stored within the network.

An electric power system can be characterized as a non-linear, large-scale, dynamic, and time-variant parameter system. Because of the advantages listed above, neural network provides an effective alternative to address various power system problems. The applications of neural networks in power system include [15],[16]:

1. System planning
    - Load forecasting

- Unit commitment
- Generation expansion and maintenance scheduling

2. Security assessment
   - Transient stability assessment
   - Voltage stability assessment
   - Contingency screening
3. Fault detection and diagnosis
   - Alarm processing
   - Component fault detection
   - Power system fault detection
4. Control
   - Machine and plant control
   - Voltage reactive power control
   - Power system stabilizer tuning
5. Analysis
   - Parameter and state estimation
   - Machine, plant, and system modeling
   - Load modeling

1.4 ANN-based Dynamic Equivalent

Recently, the ANN technique has been applied to the subject of dynamic equivalents due to its superior capability of capturing arbitrary input-and-output mappings. The ANN-based equivalent, represented by a set of neural networks, is a “black box” in nature. It only needs the measurements at the retained area

boundary buses instead of the detailed model information about the external area. This feature is desired for the on-line DSA applications as the responses at the buses on the retained area boundary can be readily accessed with the help of the synchronized phasor measurement unit (PMU).

In [17], the authors used a bottleneck neural network and a recurrent neural network to build the equivalent model. A virtual state vector is defined in the recurrent neural network; while the bottleneck network converts the power injections from ANN-based equivalent to the state vector at the input side and the state vector to the power injections at the next time instant at the output side. It is to be noted that the proposed model did not take into account the voltage responses at the connection buses. Therefore, a complex neural network has to be used to fully capture the characteristics of the external area. In [18], the authors applied a grey-box neural network to form an equivalent system. However, the proposed network must have the same number of state variables as in the coherency-based equivalent system. Therefore the training process could become exhaustive when the scale of the external area is relatively large. The authors in [19] proposed a fully recurrent neural network-based equivalent. In this model, the voltages at the connection buses together with the feedback of the previous current injections are used as the inputs; while its outputs are the current injections at the present time instant. The study in [20] proposed a two-network model that theoretically has a similar structure to the dynamic system described by a set of differential algebraic equations (DAEs). Similar to [19], the feasibility

of the proposed method could become questionable as the scale of the external area increases in practical implementation.

1.5 Problem Statement

In the coherency-based equivalent, the definition of the retained area can impart a significant impact on the effectiveness of the reduced system in preserving the dynamic characteristics of the study area. As more components are included in the retained area, more information about the dynamic characteristics of the study area can be preserved. Further study is needed to provide a systematic approach to identify an appropriate retained area boundary that not only includes the critical generators in the external area but also limits the scale of the corresponding reduced system after the dynamic equivalent is formed.

It is also noted that the system operating conditions change constantly in a realistic setting. Generator coherency information obtained under one operating condition might not be applicable to another condition. For a new operating condition, generator coherency needs to be re-evaluated. This is a time-consuming process, especially for large-scale power systems. Therefore significant strides in developing improved dynamic equivalents can be made if an efficient technique is developed to predict the variations in coherency behavior as the system condition changes.

In the conventional dynamic equivalent, the errors resulting from the generator aggregation process cannot be completely eliminated. This is true especially for the classical generator aggregation method. The errors will significantly affect the equivalencing accuracy of the reduced system as the

simulation evolves following a system disturbance. This drawback becomes more significant in the present setting as the models in the external area might be inaccessible to a single entity in the restructured environment. Therefore, the equivalent system based on the planning cases might lead to inaccurate evaluation results. Further study focused on the improvement of the coherency-based equivalent for on-line DSA is needed. Specifically, approaches to improve the equivalencing accuracy with the incorporation of PMU samplings need to be investigated. In [21] the frequency dependent network equivalent is appended to the coherency-based dynamic equivalent to improve the equivalencing accuracy for real-time digital simulators. However, because only the high frequency components of the full system response are compensated in the reduced system, a relatively large discrepancy can be observed for the period dominated by the slow oscillation modes.

1.6 Dissertation Organization

In this dissertation, the methods to improve the feasibility of the coherency-based dynamic equivalents have been studied and validated. A brief introduction has been presented in Chapter 1. The remainder of this dissertation is organized as follows:

In Chapter 2, the method to identify the critical generators in the initial external area has been proposed. Three criteria, consisting of the power transfer distribution factors (PTDFs), the estimated generator rotor acceleration during fault duration, and the mode participation factors, are detailed. The effectiveness

of the proposed method in forming appropriate retained area boundary has been verified on the test system representing the entire eastern interconnection system.

In Chapter 3, a systematic approach to predict the changing patterns of generator slow coherency for different operating conditions has been proposed. Based on the predicted coherency patterns, the retained area boundary is adjusted by including the critical generators in the external area which become tightly coherent with the generators in the study area. This approach has been tested on a 5186-bus representation of a portion of the WECC system. The results validate the efficacy of the proposed approach in forming the improved dynamic equivalents.

In Chapter 4, the concept of hybrid dynamic equivalents has been developed. The details about the training set formulation, the neural network structure, and the integration of the ANN-based equivalent into the existing transient simulation software packages are discussed. To this end, the feasibility of the proposed algorithm is also tested on a portion of the WECC system. The accuracy of the hybrid reduced system in preserving the dynamic characteristics of the retained area has been verified.

Finally, the conclusions and contributions are summarized in Chapter 5 where the directions for future research work are also provided.

Chapter 2

RIGHT-SIZED DYNAMIC EQUIVALENTS

2.1 Background

In conventional dynamic equivalents, the study area is often demarcated on the basis of ownership or geographic considerations. Under certain conditions, however, the generators in the external area could have significant influences on the dynamic performance of the study area and including them in the equivalents might lead to mismatches in simulations. To account for this discrepancy, it is necessary to adjust the study area boundary and retain these critical generators and associated buses for better equivalencing accuracy.

In this chapter, the equivalencing accuracies of the ISO-New England (ISO-NE) system are compared using different retained area definitions for the system representing the entire US/Canada eastern interconnection. In addition, an analytical approach has been proposed to identify the proper extent of the retained area boundary to accurately preserve the dynamic characteristics of the ISO-NE system.

2.2 Impacts of Retained Area Adjustment

A large-scale power system with the detailed representation of the US/Canada eastern interconnection and the simplified representation of the neighboring systems is used. In this test system as shown in Fig. 2.1, the area comprised of ISO-NE, New Brunswick (NB), and Nova Scotia (NS) is treated as the study area. The detailed generator models with exciters, governors, and power system stabilizers (PSS) are used for all machines in the study area.

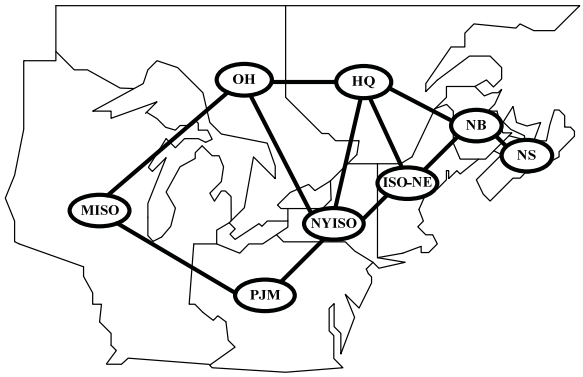

Fig. 2.1 Diagram of the main portion of the test system [5].

For the specified study area, three buffer areas of different sizes are designated manually in Task 1, 2, and 3. The details about the areas included in the buffer area are given in Table 2-1.

Table 2-1 Retained area definitions in Task 1-3

	Study area	Buffer area	External area
Task 1	ISO-NE, NB, NS	----------	Remaining syst.
Task 2	ISO-NE, NB, NS	NYISO	Remaining syst.
Task 3	ISO-NE, NB, NS	NYISO, OH, HQ	Remaining syst.

To identify the groups of coherent generators, both the weak-link method and the tolerance method available as options in DYNRED are tested. For the tolerance-based method, the right eigenvectors associated with the inter-area modes (< 1Hz) are calculated using the small signal analysis tool (SSAT) and then imported into DYNRED. Experience with large systems has shown that a threshold of 0.98 or higher may be needed to achieve adequate results using the tolerance-based method [22]. With a tolerance threshold of 0.995 being selected, a total of 226 coherent groups and 487 ungrouped generators are formed. By contrast, 461 coherent groups and 264 ungrouped generators are identified using the weak-link method. Compared to the tolerance-based method, it can be seen

that the weak-link method tends to identify more coherent groups but fewer ungrouped generators.

In addition to the study area and buffer area, all the slack nodes and the high voltage direct current lines within the external area are also retained in forming the reduced system. Then all the coherent generators in the external area are aggregated to the equivalent generator models defined by the classical representation. It is found that the best results are obtained when D is equal to 0.8 times H. In the study area and buffer area, the generators along with all associated controls are completely retained. Based on different combinations of the buffer areas and the generator coherency identification methods, six reduced systems are constructed in DYNRED. In Table 2-2, the number of buses and generators in the different reduced system are summarized. All the cases are designated using a self-explanatory convention. For instance, W1 denotes Task 1 with the weak-link method, and T2 is Task 2 with the tolerance-based method.

Table 2-2 Summary of reduced systems

Case	Buses		Generators	
	#	% of full syst.	#	% of full syst.
Full syst.	43609	100.0%	2490	100.0%
W1	8074	18.5%	1112	44.7%
W2	9595	22.0%	1243	49.9%
W3	13641	31.3%	1508	60.6%
T1	8075	18.5%	1139	45.7%
T2	9658	22.2%	1312	52.7%
T3	13598	31.2%	1518	61.0%

As can be seen from Table 2-2, the bus reduction ratio for different cases ranges from 18.5% to 31.3%, and the generator reduction ratio varies in the range

from 44.7% to 61.0%. For the same task, the reduced systems based on two different coherency identification methods give similar results in terms of the bus and generator reduction ratios, e.g. W1 and T1.

2.2.1 Equivalencing Accuracy Verification

To validate the efficacy of the different reduced systems in the time-domain simulation, a three-phase fault is applied on a 345 kV bus that is located in the southern part of the ISO-NE system at 0.5 s. After 8 cycles, the fault is cleared by opening two 345 kV transmission lines connected to the faulted bus. The entire simulation duration is 20 s. On an Intel i5 CPU (2.4GHz) PC with 2 GB of RAM and using the transient stability analysis tool (TSAT), the simulation execution time of the full system and reduced systems are summarized in Table 2-3. It is seen that a significant reduction in the execution time can be achieved when the reduced systems are used. As the size of the retained area increases from Task 1 to Task 3, the execution time increases accordingly. However, a saving of 74.0% of the full system execution time can still be achieved in case T3. It is also worth noting that the difference resulting from the coherency identification methods is also found relatively small for each task. As a performance metric for time-domain simulation, the following performance index (PI) [22] is defined:

$$\text{PI}=\frac{1}{\Delta x_f}\sqrt{\int_0^T \left(x_f - x_r\right)^2 dt}\times 100\% \tag{2.1}$$

where f and r denote the full system and the reduced system, respectively, x is the system state of interest, Δx_f is the maximum peak-to-peak value of x in the full system, and T is the simulation duration.

For different reduced systems, the largest PI of the generator rotor angle states and the corresponding generator are also listed in Table 2-3.

Table 2-3 Comparison of execution time and the largest PI

Case	Simulation time (s)/ % of full syst.	Largest PI of rotor angle / Bus #
Full	273 / 100%	------
W1	48 / 17.6%	35.03% / gen. 71126
W2	55 / 20.1%	16.02% / gen. 71126
W3	69 / 25.3%	17.40% / gen. 71126
T1	45 / 16.5%	33.23% / gen. 71126
T2	57 / 20.9%	15.80% / gen. 71126
T3	71 / 26.0%	16.24% / gen. 71126

In Table 2-3, it shows that the reduced systems in both Task 2 and Task 3 can achieve a substantial reduction in the largest PI. As shown in Fig. 2.1, the NYISO system is tightly coupled with the study area through the inter-area tie lines, and the simulated fault location is close to the New York–New England interface. Therefore, including the NYISO system into the buffer area is beneficial for the preservation of the dynamic performance of the ISO-NE system. The same conclusions can also be drawn from the responses of the relative rotor angle and terminal voltage of generator 71126, as shown in Fig. 2.2 and Fig. 2.3 respectively. Compared to Task 1, it can be seen that the discrepancy between the responses in the full system and reduced system has been reduced considerably in Task 2. This is true especially for the short period after the disturbance.

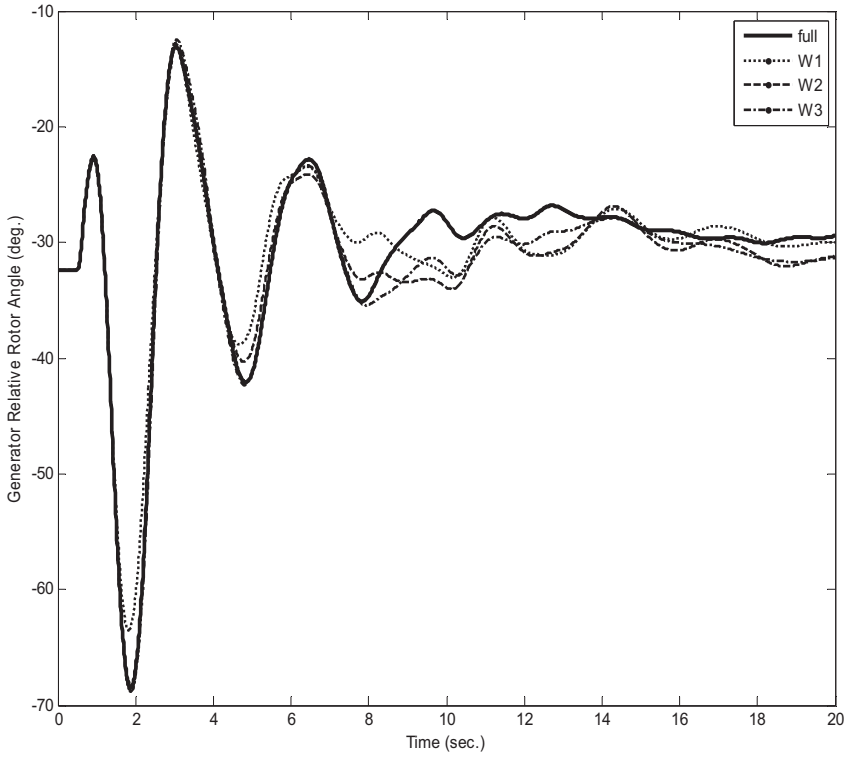

(a) Relative rotor angle response of generator 71126

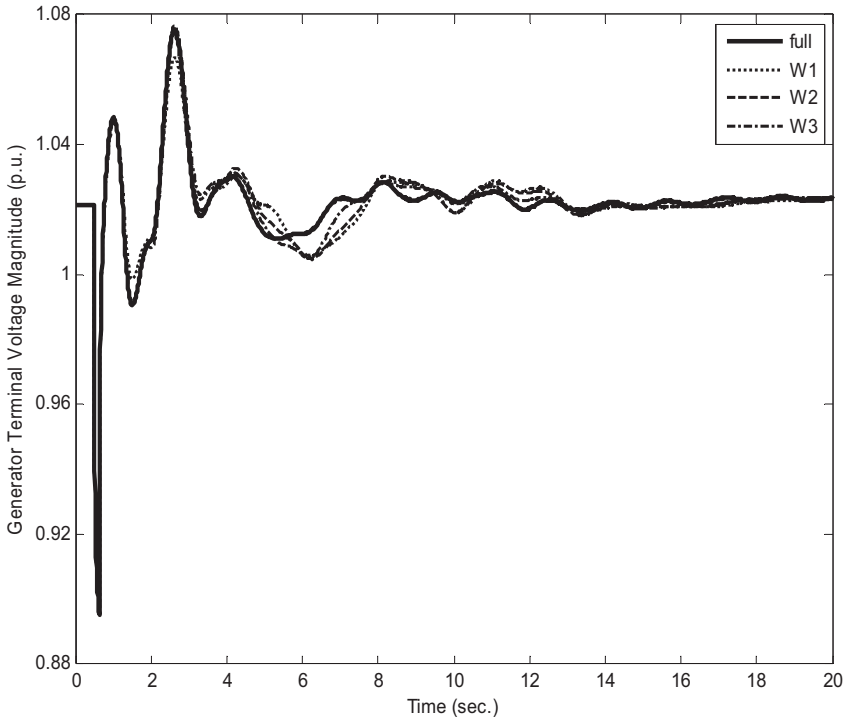

(b) Terminal voltage response of generator 71126

Fig. 2.2 Responses in Task 1-3 using the weak-link method.

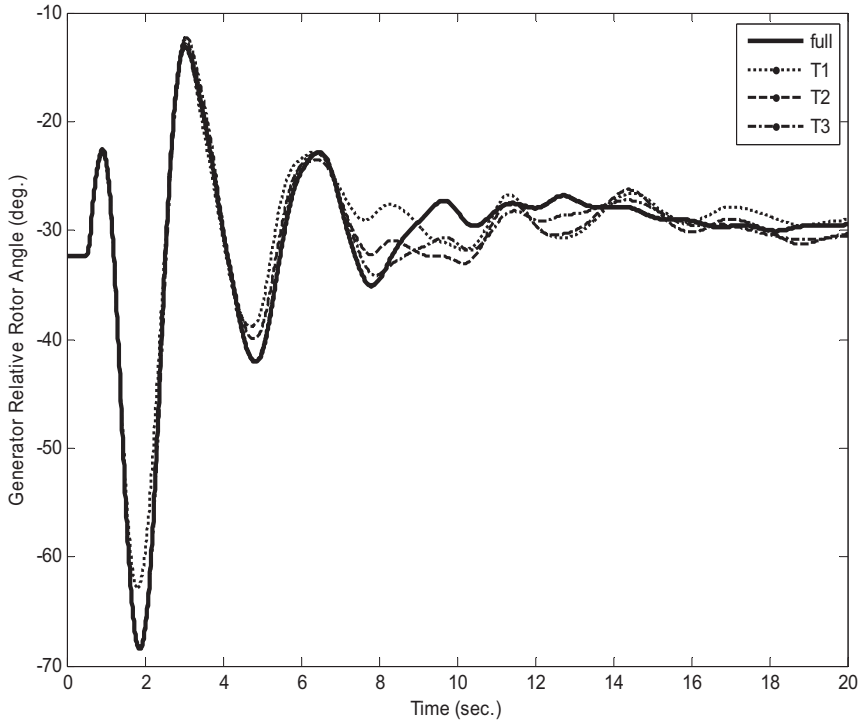

(a) Relative rotor angle response of generator 71126

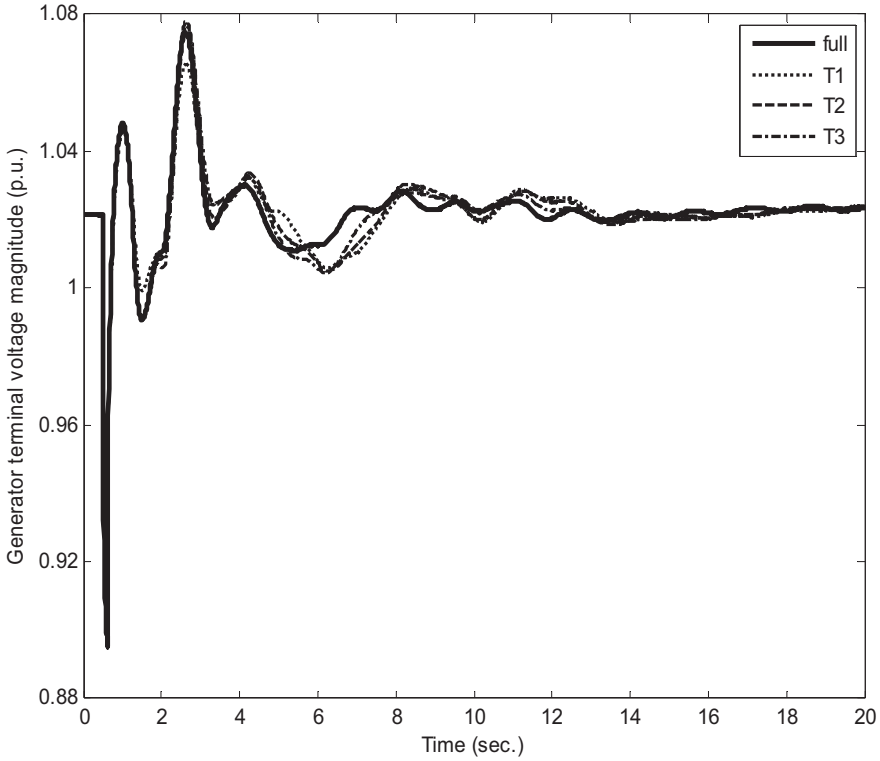

(b) Terminal voltage response of generator 71126

Fig. 2.3 Responses in Task 1-3 using the tolerance-based method.

However, this improvement is insignificant when the largest buffer area in Task 3 is used. Because the detailed models of generators, exciters, PSSs, and governors in the external area have already been neglected during the aggregation process, the discrepancy becomes large as the simulation evolves in all reduced systems.

It is to be noted that although the largest PI in Task 2 is smaller than that in Task 3, the reduced system in Task 2 is not necessarily better than the one obtained in Task 3 in terms of representing the dynamics of the ISO-NE system throughout the entire simulation duration. In fact, the response obtained from the reduced system in Task 3 is closer to the full system response than in Task 2 during the period ranging from 4 s to 12 s, as shown in Fig. 2.2 (a) and Fig. 2.3 (a). By ignoring the minor difference between the largest PIs of the tolerance-based method and the weak-link method for a specific task, it can be concluded that both methods are effective in identifying the coherent generators for forming dynamic equivalents.

2.2.2 Small Signal Analysis Verification

The inter-area modes in the full system and reduced systems are calculated using the package SSAT and summarized in Table 2-4 and Table 2-5.

Table 2-4 Modal analysis of W1- 3

Full system freq. (Hz)/ damping	Weak-link method		
	W1	W2	W3
0.37 / 8.5%	0.35 / 9.1%	0.35 / 8.6%	0.34 / 8.5%
0.54 / 2.3%	0.53 / 3.4%	0.53 / 3.4%	0.53 / 3.3%
0.56 / 8.1%	0.55 / 7.7%	0.55 / 7.2%	0.55 / 7.5%
0.70 / 8.8%	0.71 / 4.5%	0.71 / 4.5%	0.71 / 4.5%

Table 2-5 Modal analysis of T1 - 3

Full system freq. (Hz)/ damping	Tolerance-based method		
	T1	T2	T3
0.37 / 8.5%	0.34 / 9.7%	0.34 / 8.9%	0.34 / 8.6%
0.54 / 2.3%	0.53 / 3.6%	0.53 / 3.5%	0.53 / 3.4%
0.56 / 8.1%	0.54 / 7.5%	0.54 / 7.1%	0.54 / 7.5%
0.70 / 8.8%	0.70 / 4.6%	0.70 / 4.6%	0.70 / 4.6%

It can be concluded from Table 2-4 and Table 2-5 that the selected inter-area modes are preserved in the reduced systems. However, the mismatches in both oscillation frequency and damping ratio are observed. This discrepancy mainly results from neglecting the detailed generator models in the classical aggregation process, and it varies depending on different inter-area modes. Compared to the full system, for instance, Mode 2 in the reduced systems for all cases is over-damped; while a lower damping ratio of Mode 4 can be found. By retaining more participating generators in the remote area, the reduced systems in W3 and T3 provides more accurate modal information. However, this improvement is relatively small considering the substantial number of generators that need to be additionally retained. It is also worth noting that the modal information for a specific task does not vary significantly in the reduced systems based on the weak-link method and the tolerance-based method.

2.3 Buffer Area Determination Approach

In previous tasks, the reduced systems based on different buffer areas have been studied. For large-scale power systems, it is time-consuming to exhaustively test various buffer areas in order to obtain an appropriate reduced system model

for stability assessment. Therefore an analytical approach is desirable in practical applications to determine the proper extent of the buffer area. To address this challenge, the algorithm as shown in Fig. 2.4 is proposed.

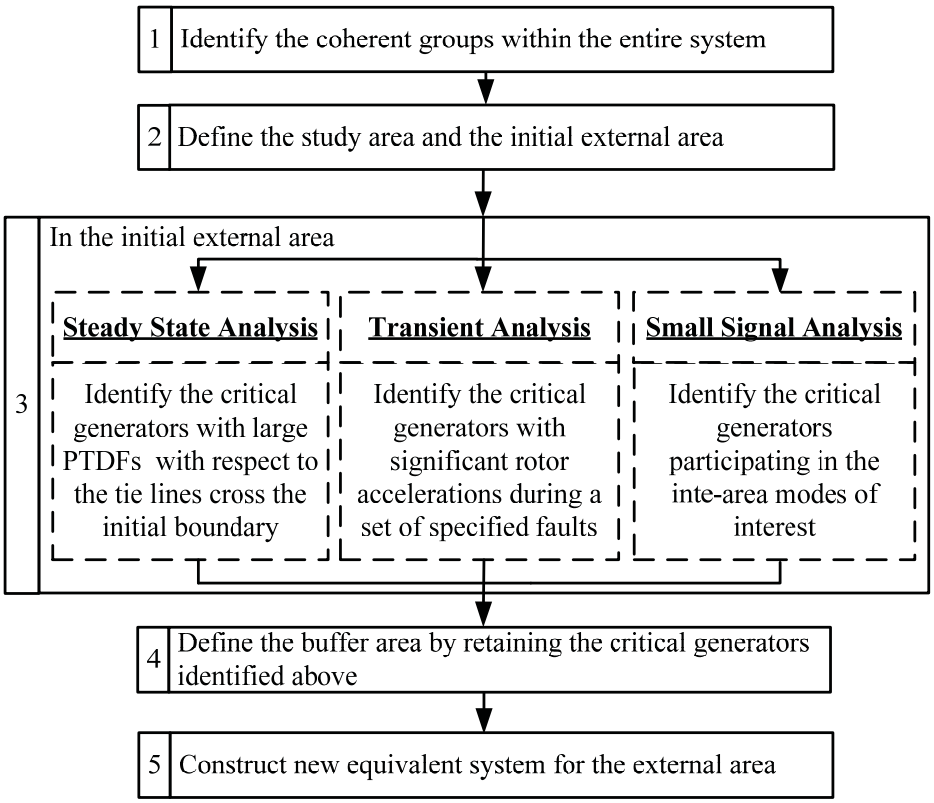

Fig. 2.4 Buffer area determination approach.

In the proposed algorithm, the entire area, except for the study area, is treated as the initial external area at the start of the algorithm. Then three criteria based on PTDFs, the generator rotor acceleration during fault duration, and the mode participation factors are validated to identify the generators that are critical to the dynamic performance of the study area. With the buffer area consisting of the identified generators being retained, new equivalent model of the external area can be formed in DYNRED.

2.3.1 PTDF-based Criterion

In dynamic equivalents, the study area is connected to the initial external area through the tie-line interfaces. Therefore the study area can be equivalenced into a dynamic system using the tie-line flows as the inputs. In the initial external area, the generators having more significant impacts on the tie-line flows are expected to be more critical to the study area in both the steady state and dynamic performance. In the proposed algorithm, this impact is evaluated by the DC power flow-based PTDFs. By definition, the active power flow over the line from bus *i* to bus *j* due to the generation change at bus *g* can be approximated by [23]:

$$PTDF_g^{ij} = \frac{\mathbf{M}_l^T \mathbf{B}^{-1} \mathbf{M}_{Gg}}{x_{ij}} \tag{2.2}$$

where **B** is the node susceptance matrix, $\mathbf{M}_l$ is the node-branch incidence vector, $\mathbf{M}_{Gg}$ is the vector with 1 at the entry corresponding to generator *g* and zeros elsewhere, and x_{ij} is the primitive line reactance.

Although PTDF is a steady state index, it provides in-depth insight into the system mutual impacts, and it can be used to judge the effect on dynamic performance.

2.3.2 Generator Rotor Acceleration-based Criterion

For a specific contingency in the study area, generator response in terms of rotor acceleration decrease in magnitude as it is located electrically far away from the disturbance. Therefore this impact can be interpreted as a measure of the electrical connections among the generators in the initial external area and in the study area.

In the proposed algorithm, the classical generator model neglecting the damping coefficient is implemented. A three-phase fault is assumed to be applied on the critical bus in the study area. For a n_G-generator system, the bus admittance matrix is reduced to the generator internal buses. During this process, the faulted bus is also retained. Under the pre-fault condition, the electrical power output of generator i is given by:

$$P_{Gi}(t_0) = \sum_{\substack{j=1 \\ j \neq i}}^{n_G} E_{i0} E_{j0} B_{ij} \sin\left(\delta_{i0} - \delta_{j0}\right) + E_{i0} V_{f0} B_{ij} \sin\left(\delta_{i0} - \theta_{f0}\right) \tag{2.3}$$

where $E_{i0}\angle\delta_{i0}$ is the internal voltage of generator i, $V_{f0}\angle\theta_{f0}$ is the voltage of the faulted bus f, B_{ij} is the equivalent admittance between the internal buses of generator i and generator j, B_{if} is the equivalent admittance between the faulted bus f and the internal bus of generator i, and n_G is the total number of generators.

At $t = t_0^+$, a three-phase fault is applied on bus f and it is assumed that the generator internal voltages remain constant. Because $V_{f0}^+ = 0$, the acceleration power on the generator i is:

$$\Delta P_{Gi} = P_{Gi}\left(t_0\right) - P_{Gi}(t_0^+) = E_{i0} V_{f0} B_{if} \sin\left(\delta_{i0} - \theta_{f0}\right) \tag{2.4}$$

The acceleration of the generator i during the fault is:

$$a_i = \Delta P_{Gi} / M_i \tag{2.5}$$

where the generator inertia $M_i = 2H_i/\omega_R$, H_i is inertia constant of generator i in s, and ω_R is the base frequency in radians per second (376.99 rad/s).

Assuming that the fault duration time is t_f and the acceleration remains constant, the rotor angle deviation of generator i is given by:

$$\Delta\delta_i = \frac{1}{2}|a_i|t_f^2 = \frac{1}{2M_i}\left|E_{i0}V_{f0}B_{if}\sin\left(\delta_{i0}-\theta_{f0}\right)\right|t_f^2 \tag{2.6}$$

In the initial external area, the generators having large rotor angle deviations tend to have tight electrical coupling with the faulted area. Therefore retaining these generators is helpful in preserving the dynamic performance of the study area. It is noted that the selected generators are very sensitive to the fault location. To obtain trustworthy results, multiple faults across the study area ought to be tested.

2.3.3 Mode Participation-based Criterion

As shown in Section 2.2, certain modal information varies in different reduced systems. In order to preserve the modes that are critical to the stability analysis of the study area, the participating generators in the initial external area need to be retained. In general, a power system can be represented by a set of DAEs:

$$\begin{aligned}\dot{\mathbf{x}} &= \mathbf{f}(\mathbf{x},\mathbf{y})\\ \mathbf{0} &= \mathbf{g}(\mathbf{x},\mathbf{y})\end{aligned} \tag{2.7}$$

where **x** is the system state variable vector, **y** is the network variable vector, **f** is a function vector representing the system component dynamics, and **g** is a function vector representing the network constraints. At the equilibrium point, (2.7) can be linearized as:

$$\begin{aligned}\Delta\dot{\mathbf{x}} &= \mathbf{f}_\mathbf{x}\Delta\mathbf{x} + \mathbf{f}_\mathbf{y}\Delta\mathbf{y}\\ \mathbf{0} &= \mathbf{g}_\mathbf{x}\Delta\mathbf{x} + \mathbf{g}_\mathbf{y}\Delta\mathbf{y}\end{aligned} \tag{2.8}$$

where $\mathbf{f}_\mathbf{x}=\partial\mathbf{f}/\partial\mathbf{x}$, $\mathbf{f}_\mathbf{y}=\partial\mathbf{f}/\partial\mathbf{y}$, $\mathbf{g}_\mathbf{x}=\partial\mathbf{g}/\partial\mathbf{x}$, and $\mathbf{g}_\mathbf{y}=\partial\mathbf{g}/\partial\mathbf{y}$ are partial derivatives matrices evaluated at the equilibrium point. Eliminating $\Delta\mathbf{y}$ in (2.8) gives:

$$\Delta\dot{\mathbf{x}} = \mathbf{A}_{sys}\Delta\mathbf{x} \tag{2.9}$$

where $\mathbf{A}_{sys}$ is the system state matrix defined as $\mathbf{A}_{sys} = \mathbf{f_x} - \mathbf{f_y}\,\mathbf{g_y}^{-1}\mathbf{g_x}$. For the system state matrix $\mathbf{A}_{sys}$, the eigenvalues can be obtained by solving:

$$\det\left(s\mathbf{I} - \mathbf{A}_{sys}\right) = 0 \tag{2.10}$$

Assuming that λ_i is the i^{th} eigenvalue of $\mathbf{A}_{sys}$, the corresponding right and left eigenvectors can be obtained by solving:

$$\left(\mathbf{A}_{sys} - \lambda_i\mathbf{I}\right)\boldsymbol{\phi}_i = \mathbf{0} \tag{2.11}$$

$$\boldsymbol{\psi}_i\left(\mathbf{A}_{sys} - \lambda_i\mathbf{I}\right) = \mathbf{0} \tag{2.12}$$

where $\boldsymbol{\phi}_i$ and $\boldsymbol{\psi}_i$ are the corresponding right and left eigenvectors, respectively.

The k^{th} element of right eigenvector, namely ϕ_{ki}, measures the activity of Δx_k in the i^{th} mode, and the k^{th} element of the left eigenvector, namely ψ_{ki}, weights the contribution of the activity of Δx_k to the i^{th} mode. With the combination of the information contained in the right and left eigenvectors, the mode participation factor can be defined as [24]:

$$p_{ki} = \phi_{ki}\psi_{ki} \tag{2.13}$$

The participation factor measures the association between the k^{th} mode and the i^{th} state variable. It can be easily proven that the sum of the participation factors associated with any mode $\sum_i p_{ki}$ or with any state variable $\sum_k p_{ki}$ is equal to 1.

In the proposed algorithm, the participation factor of the generator rotor angle state in the inter-area mode is calculated. It is to be noted that some of the

identified generators might not be located in the sub-system that is adjacent to the study area. It is also possible that the resulting improvement might not be observable from the time-domain simulation if the persevered modes are not properly excited by the specific contingency.

The proposed algorithm is applied to the same test system as in Section 2.2. In the initial external area, the generators having a capacity greater than 50MVA are selected as the candidates. Among these candidates, different criteria are implemented to identify the critical generators to be included in the buffer area. For different combinations of the criteria, two revised reduced systems, namely ExdCase1 and ExdCase2, are formed as shown in Table 2-6. ExdCase1 uses both PTDF and rotor acceleration criteria, while ExdCase2 uses all the three criteria. When using the mode participation criterion, only the inter-area modes with a frequency less than 0.9 Hz are considered.

Table 2-6 Summary of the revised buffer areas

Criteria		ExdCase1	ExdCase2
PTDF	Threshold	3.0%	3.0%
	Generator number	45 (*37)	45 (*37)
Rotor acceleration	Threshold	0.2 degree	0.2 degree
	Generator number	66 (*57)	66 (*57)
Mode participation	Threshold	-------	0.5
	Generator number	-------	73 (*1)
Total	Generator number	67	137

* denotes the number of generators that are located in the buffer area of Task 2 in Section 2.2.

In Section 2.2, a total of 233 generators are retained in the buffer area specified in Task 2. Using the proposed algorithm, this number decreases to 67 and 137 in ExdCase1 and ExdCase2, respectively. When using PTDF and rotor

acceleration as the criteria, it is seen from Table 2-6 that most of the identified generators have already been included in the buffer area in Task 2. It is consistent with the finding that compared to Task 1 and Task 3, the reduced system in Task 2 achieved both good equivalencing accuracy and appropriate system complexity. Using the mode participation-based criterion, most of the identified generators are located in the remote subsystems.

To build the reduced system, the identified generators are included into the buffer area, and the network outside of the retained area is reduced except for the terminals of the tie lines across the retained area boundary. For the sake of simplicity, only the weak-link method is tested. The scales of new reduced systems are summarized in Table 2-7, and the responses of generator 71126 in different reduced systems to the same contingency as in Section 2.2 are compared in Fig. 2.5.

Table 2-7 Summary of the new reduced systems

	Buses		Generators		Rotor angle PI of gen. 71126
	#	% of full syst.	#	% of full syst.	
Full syst.	43609	-----	2490	------	------
W2	9595	22.0%	1243	49.9%	16.02%
ExdCase1	8191	18.8%	1115	44.8%	23.11%
ExdCase2	8292	19.0%	1207	48.5%	20.70%

Table 2-7 shows that fewer buses and generators are retained in ExdCase1 and ExdCase2 than in Task 2. The PIs of generator 71126 in ExdCase1 and ExdCase2 are reduced significantly from that in W1, both of which are close to the corresponding PI value obtained from W2.

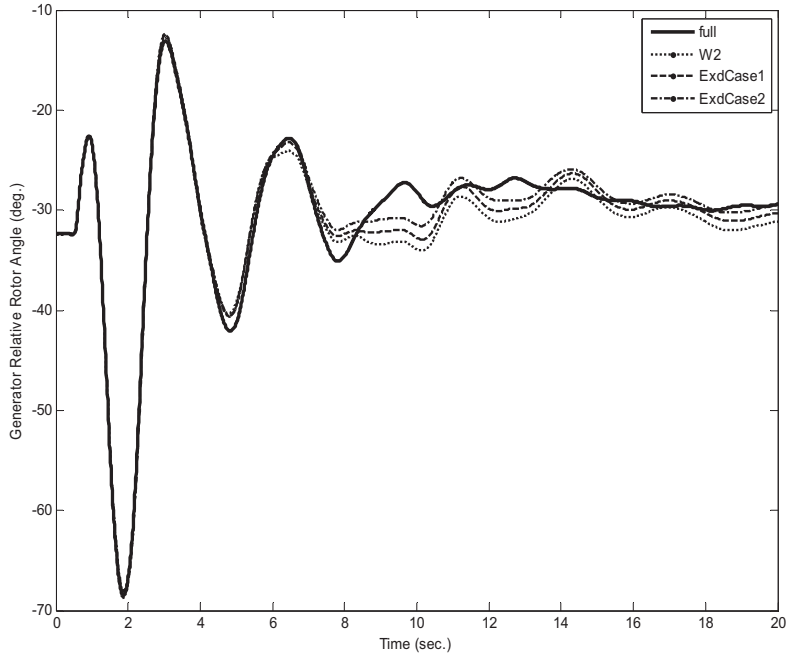

(a) Relative rotor angle response of generator 71126

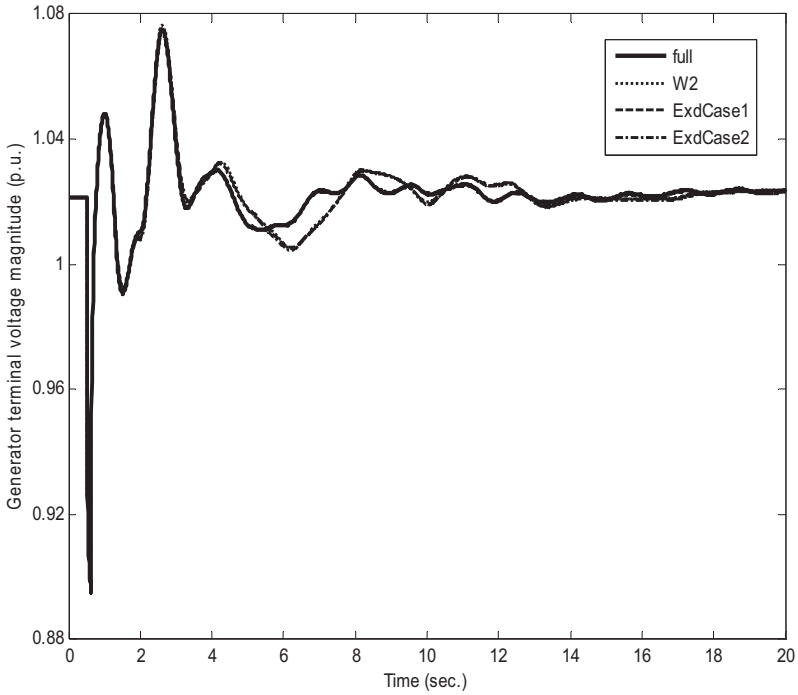

(b) Terminal voltage response of generator 71126

Fig. 2.5 Response comparison of new reduced systems.

It is seen from Fig. 2.5 that the responses of the reduced systems using the new buffer areas are close to W2. The frequencies and damping ratios of the selected inter-area modes in ExdCase1 and ExdCase2 are summarized in Table 2-8.

Table 2-8 Inter-area modes in new reduced systems

Mode #		1	2	3	4
Mode freq. (Hz) / damping ratio	Full syst.	0.37 / 8.5%	0.54 / 2.3%	0.56 / 8.1%	0.70 / 8.8%
	W2	0.35 / 8.6%	0.53 / 3.4%	0.55 / 7.2%	0.71 / 4.5%
	ExdCase1	0.35 / 8.9%	0.53 / 3.4%	0.55 / 7.2%	0.71 / 4.5%
	ExdCase2	0.36 / 8.0%	0.54 / 2.7%	0.55 / 7.3%	0.71 / 4.6%

From Table 2-8, it can be concluded that the reduced system in ExdCase1 provides the same modal information as in W2. As more participating generators in the remote area are included into the buffer area, the mismatch between the full system and ExdCase2, especially for Mode 2, is reduced considerably.

2.4 Conclusion

In this chapter, the efficacy of the new version of DYNRED has been validated based on the test system representing the entire US/Canada eastern interconnection. The results reveal that both the weak-link method and the tolerance-based method are effective in identifying the coherent generators to be aggregated. In addition, the proposed algorithm is able to identify the critical generators to be included in the buffer area, and the resultant reduced system can achieve a good balance between equivalencing accuracy and system complexity.

Chapter 3

DYNAMIC EQUIVALENTS CONSIDERING SYSTEM CONDITION CHANGE

3.1 Background

In conventional dynamic equivalents, the same equivalent model of the external area is typically used for various operating conditions. Under certain conditions, however, it is necessary to adjust the study area boundary and retain these critical generators and associated buses for better equivalencing accuracy. In the literature, generator coherency is used to measure the similarity of generator responses following a disturbance. The coherent generators are tightly coupled and therefore have significant electromechanical interactions. It is reasonable to expect that the generators in the external area presenting tight coherency with the study area are critical to accurately preserving the dynamic performance of the study area.

In this chapter, a systematic approach is developed to predict the variation in generator slow coherency behavior when the system condition is subject to change. The innovative step developed is depicted in Fig. 3.1. Instead of re-evaluating the slow coherency patterns from scratch under a new system condition, the critical generators in the initial external area that are predicted to become tightly coherent with the retained generators in the initial study area are identified. Based on this determination, the revised retained area boundary is formed leading to new equivalent model.

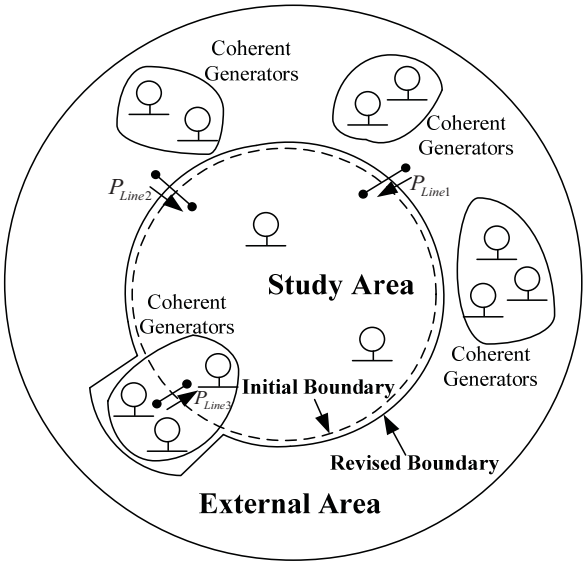

Fig. 3.1 Illustration of the proposed algorithm.

3.2 Slow Coherency Index

Generator slow coherency provides an in-depth insight into the system dynamic behavior. By inspecting the mode shapes associated with the specific slow modes based on the linearized power system model, slow coherency among generators can be evaluated. Because slow modes are insensitive to the details of generator models and the size of disturbance, the slow coherency-based method is suitable for generator coherency identification in large-scale power systems [25]. Prior to the introduction of the slow coherency index, the following assumptions are made:

- Coherent groups are independent of the size of the disturbance. Therefore, slow coherency can be determined by considering a linearized system model.
- Coherent groups are independent of the amount of details in the generating models. Because excitation and governor systems only modify the damping of the transients but do not change the natural frequencies and mode shapes, the

slow coherency pattern can be evaluated using a classical representation of the synchronous generators.

Based on the above assumptions, a n_G-generator power system is represented as:

$$\begin{aligned} \dot{\delta}_i &= (\omega_i - \omega_0)\omega_R \\ 2H_i\dot{\omega}_i &= -D_i(\omega_i - \omega_0) + (P_{mi} - P_{Gi}),\ i = 1,2,...,n_G \end{aligned} \tag{3.1}$$

where δ_i is rotor angle, ω_i is rotor speed, ω_0 is reference speed, ω_R is base frequency, P_{mi} is mechanical input power and assumed to be constant, P_{Gi} is electrical output power, H_i is the generator inertia coefficient, and D_i is the damping coefficient.

All the loads within the system are modeled as the constant-impedance type. Then the system admittance matrix is reduced to the generator internal buses. Correspondingly, the electrical output power of generator i in (3.1) is given by:

$$P_{Gi} = E_i^2 G_{ii} + \sum_{j=1, j\neq i}^{n_G} E_i E_j \left[G_{ij}\cos(\delta_i - \delta_j) + B_{ij}\sin(\delta_i - \delta_j) \right] \tag{3.2}$$

where E_i is the voltage behind transient reactance of generator i, G_{ij}, and B_{ij} are the real and imaginary parts of the (i,j) element of the system admittance matrix reduced to the generator internal buses, respectively. Linearizing (3.1) at the equilibrium point gives:

$$\begin{bmatrix} \Delta\dot{\boldsymbol{\delta}} \\ \Delta\dot{\boldsymbol{\omega}} \end{bmatrix} = \begin{bmatrix} \mathbf{0} & \mathbf{I} \\ -\mathbf{M}^{-1}\mathbf{K} & -\mathbf{M}^{-1}\mathbf{D} \end{bmatrix} \begin{bmatrix} \Delta\boldsymbol{\delta} \\ \Delta\boldsymbol{\omega} \end{bmatrix} \tag{3.3}$$

where $\Delta\boldsymbol{\delta}$ is the generator rotor angle deviation vector, $\Delta\boldsymbol{\omega}$ is the generator speed deviation vector, $\mathbf{K}$ is the synchronizing power coefficient matrix, $\mathbf{M}$ is the

diagonal inertia coefficient matrix, and **D** is the diagonal damping coefficient matrix that can be ignored without loss of accuracy in slow coherency evaluation. In (3.3), the coefficient matrix is referred to as the system state matrix $\mathbf{A}_{sys}$:

$$\mathbf{A}_{sys} = \begin{bmatrix} \mathbf{0} & \mathbf{I} \\ -\mathbf{M}^{-1}\mathbf{K} & -\mathbf{M}^{-1}\mathbf{D} \end{bmatrix} \tag{3.4}$$

Given the initial value of $[\Delta\mathbf{x}^{\mathrm{T}}\ \Delta\mathbf{y}^{\mathrm{T}}]^{\mathrm{T}}$ in (3.3) following a system disturbance, namely $\boldsymbol{\xi}$, the rotor angle deviations of generator *i* and generator *j* are formed as:

$$\Delta\delta_i(t) = e^{\lambda_1}\phi_{i1}\left(\boldsymbol{\psi}_1\boldsymbol{\xi}\right) + e^{\lambda_2}\phi_{i2}\left(\boldsymbol{\psi}_2\boldsymbol{\xi}\right) + \ldots + e^{\lambda_{2n_G}}\phi_{i2n_G}\left(\boldsymbol{\psi}_{2n_G}\boldsymbol{\xi}\right) \tag{3.5}$$

$$\Delta\delta_j(t) = e^{\lambda_1}\phi_{j1}\left(\boldsymbol{\psi}_1\boldsymbol{\xi}\right) + e^{\lambda_2}\phi_{j2}\left(\boldsymbol{\psi}_2\boldsymbol{\xi}\right) + \ldots + e^{\lambda_{2n_G}}\phi_{j2n_G}\left(\boldsymbol{\psi}_{2n_G}\boldsymbol{\xi}\right) \tag{3.6}$$

where ϕ_{ik} is the i^{th} element of $\boldsymbol{\phi}_k$.

It is shown in (3.5) and (3.6) that the generator rotor angle response can be represented as a linear combination of all system modes. For a given disturbance, $\boldsymbol{\xi}$ has the same impact on all state solutions through the left eigenvectors. In (3.5), ϕ_{ij} indicates the contribution of the j^{th} mode on $\Delta\delta_i(t)$. If the right eigenvector elements, namely $[\phi_{i1},\ldots,\phi_{i2n_G}]$ and $[\phi_{j1},\ldots,\phi_{j2n_G}]$, are identical, the same generator responses in terms of $\Delta\delta_i(t)$ and $\Delta\delta_j(t)$ can be observed.

It is a general principle in generator slow coherency evaluation that only the slow modes representing the inherent structural characteristics of the system are of concern. It is a common practice to choose a specific number of the slowest modes in the system. This number primarily depends on the number of coherent groups to be formed. Suppose that the matrix $\boldsymbol{\Phi}$ consists of the right eigenvectors associated with *k* slowest modes:

$$\Phi = [\phi_1, ..., \phi_k] \tag{3.7}$$

Then the slow coherency index between generator *i* and generator *j* can be defined as:

$$d_{ij} = \frac{\upsilon_i \upsilon_j^H}{\|\upsilon_i\| \|\upsilon_j\|} \tag{3.8}$$

where $\upsilon_i = [\phi_{i1,...,} \phi_{ik}]$ and $\upsilon_j = [\phi_{j1,...,} \phi_{jk}]$ are the rows of Φ corresponding to the rotor angle states of generator *i* and generator *j*, respectively. || || denotes the 2-norm of a complex vector, and *H* denotes the conjugate transpose.

In (3.8), the scalar d_{ij} provides a numeric measure of the generator coherency with respect to the selected slow modes in the system.

3.3 Slow Coherency Index for Changed Conditions

The mains steps of the proposed algorithm to identify a properly retained area boundary for the changed operating condition include several aspects and are depicted by the flowchart in Fig. 3.2. The PTDFs are only used to identify the generator candidates in the initial external area. For certain cases, this step can be skipped. Then all the generators in the initial external area will be screened. The subsequent steps are detailed in the following sections.

3.3.1 System Variable Perturbation

To obtain the system state matrix perturbation for a new system condition, the perturbation of network variables needs to be determined first.

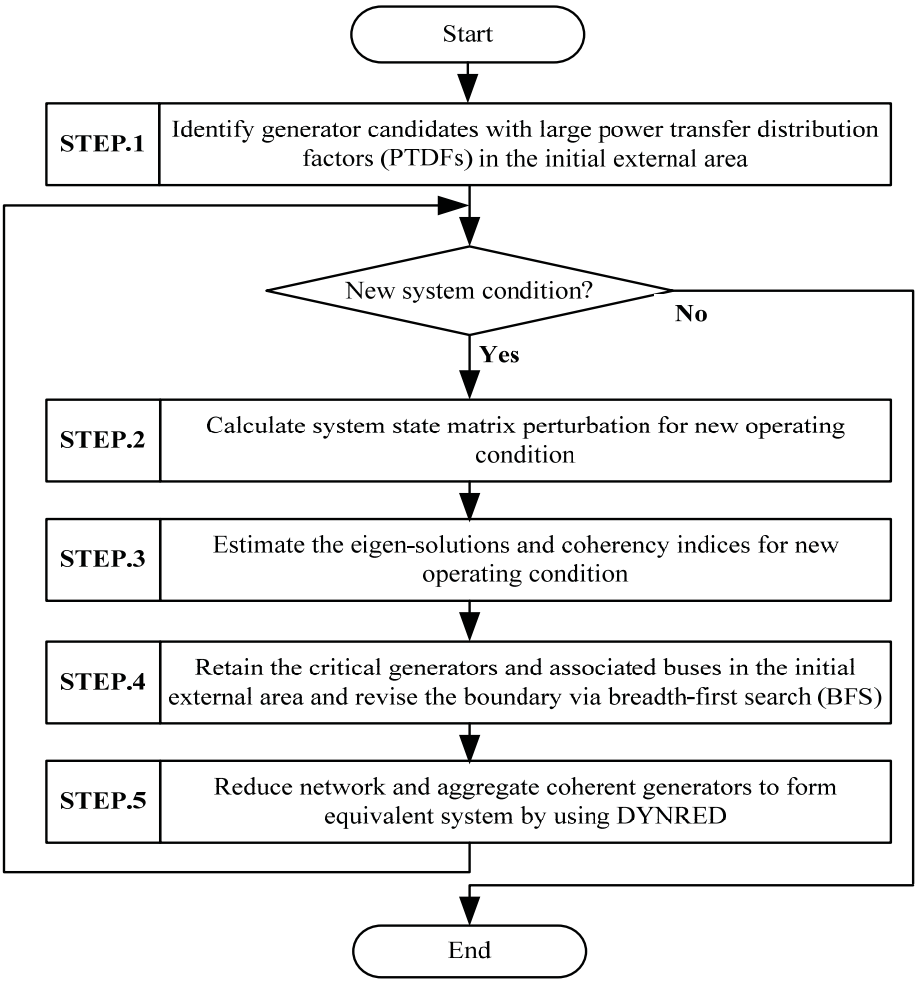

Fig. 3.2 Flowchart of retained area definition algorithm.

Assuming that the Jacobian matrix at the base case is $\mathbf{J}_{pf}$, the equation in polar coordinates relating power injection perturbation with voltage perturbation is as follow:

$$\begin{bmatrix} \Delta\mathbf{P} \\ \Delta\mathbf{Q} \end{bmatrix} = \mathbf{J}_{pf} \begin{bmatrix} \Delta\boldsymbol{\theta} \\ \Delta\mathbf{V}/\mathbf{V} \end{bmatrix} \tag{3.9}$$

where $\Delta\mathbf{P} = [\Delta\mathbf{P}_G{}^{\mathrm{T}}\ \Delta\mathbf{P}_L{}^{\mathrm{T}}]^{\mathrm{T}}$ is the active power injection perturbation vector, $\Delta\boldsymbol{\theta} = [\Delta\boldsymbol{\theta}_G{}^{\mathrm{T}}\ \Delta\boldsymbol{\theta}_L{}^{\mathrm{T}}]^{\mathrm{T}}$ is the bus voltage phase angle perturbation vector, and the subscripts G and L denote the generator and load buses, respectively. $\Delta\mathbf{Q} = \Delta\mathbf{Q}_L$ and $\Delta\mathbf{V}/\mathbf{V} = \Delta\mathbf{V}_L/\mathbf{V}_L$ are the reactive power injection perturbation vector and the voltage

magnitude perturbation vector at load buses, respectively. In (3.9), the generator bus that violates the reactive power limit is converted to a *P*-*Q* bus. Defining the sensitivity matrix as $\mathbf{S} = \mathbf{J}_{pf}^{-1}$, the bus voltage perturbation is given by:

$$\begin{bmatrix} \Delta\boldsymbol{\theta} \\ \Delta\mathbf{V}/\mathbf{V} \end{bmatrix} = \mathbf{S}\begin{bmatrix} \Delta\mathbf{P} \\ \Delta\mathbf{Q} \end{bmatrix} \tag{3.10}$$

Then the reactive power injection perturbation at generator *i* can be obtained by:

$$\Delta Q_{Gi} = \frac{\partial Q_{Gi}}{\partial \boldsymbol{\theta}}\Delta\boldsymbol{\theta} + \frac{\partial Q_{Gi}}{\partial \mathbf{V}/\mathbf{V}}\left(\Delta\mathbf{V}/\mathbf{V}\right) \tag{3.11}$$

where $\Delta\boldsymbol{\theta}$ and $\Delta\mathbf{V}/\mathbf{V}$ can be obtained from (3.10). $\partial Q_{Gi}/\partial\boldsymbol{\theta}$ and $\partial Q_{Gi}/(\partial\mathbf{V}/\mathbf{V})$ are the Jacobian matrix elements related to the reactive power injection at generator *i*.

In the classical generator model, the internal voltage behind the transient reactance of generator *i*, namely $E_i\angle\delta_i$, is defined as:

$$E_i = \sqrt{\left(V_i + Q_{Gi}x'_{di}/V_i\right)^2 + \left(P_{Gi}x'_{di}/V_i\right)^2} \tag{3.12}$$

$$\delta_i = \theta_i + \tan^{-1}\left[\left(P_{Gi}x'_{di}/V_i\right)/\left(V_i + Q_{Gi}x'_{di}/V_i\right)\right] \tag{3.13}$$

where x'_{di} is the generator transient reactance, $V_i\angle\theta_i$ is the generator terminal voltage, P_{Gi} and Q_{Gi} are the active and reactive power injections, respectively. Linearizing (3.12) and (3.13) with V_i being held constant gives:

$$\Delta E_i = \frac{P_{Gi}x'^2_{di}}{E_iV_i^2}\Delta P_{Gi} + \frac{V_i^2x'_{di} + Q_{Gi}x'^2_{di}}{E_iV_i^2}\Delta Q_{Gi} \tag{3.14}$$

$$\Delta\delta_i = \Delta\theta_i + \frac{V_i^2x'_{di} + Q_{Gi}x'^2_{di}}{E_i^2V_i^2}\Delta P_{Gi} - \frac{P_{Gi}x'^2_{di}}{E_i^2V_i^2}\Delta Q_{Gi} \tag{3.15}$$

As shown in (3.14) and (3.15), the perturbations of generator internal

voltage and rotor angle can be determined once $\Delta\mathbf{P}_G$, $\Delta\mathbf{P}_L$, and $\Delta\mathbf{Q}_L$ for different system conditions are properly defined. It is also noted that in (3.14) and (3.15) only the static transition is considered and the dynamics from one operating condition to another condition will not be taken into account. The approach to define the power injection perturbation vector for different operating condition is detailed as follows:

- **Generation Change**

Assuming the active power outputs at a set of generators are rescheduled under a new operating condition. Its impact on the remainder of the system can be simulated by setting $\Delta\mathbf{P}_G$ as:

$$\Delta\mathbf{P}_G = \sum_{i \in K_G} \mathbf{M}_{Gi} \Delta P_{Gi} \tag{3.16}$$

where K_G is the set of dispatchable generators, $\mathbf{M}_{Gi}$ is the vector with 1 at the entry corresponding to generator i and zeros elsewhere, and ΔP_{Gi} is the amount of power generation change. In (3.16), ΔP_{Gi} is determined by the scheduling methodology for the selected generators when active power imbalance within the system occurs.

- **Load Change**

The following adjustments to $\Delta\mathbf{P}_L$ and $\Delta\mathbf{Q}_L$ are also made when a set of loads are subject to changes:

$$\Delta\mathbf{P}_L = -\sum_{i \in K_L} \mathbf{M}_{PLi} \Delta P_{Li} \tag{3.17}$$

$$\Delta\mathbf{Q}_L = -\sum_{i \in K_L} \mathbf{M}_{QLi} \Delta Q_{Li} \tag{3.18}$$

where K_L is the set of changed load buses, $\mathbf{M}_{PLi}$ and $\mathbf{M}_{QLi}$ are the vectors with 1 at the entry corresponding to load bus i and zeros elsewhere, and ΔP_{Gi} and ΔQ_{Gi} are the changing amount of active and reactive power consumption at load bus i, respectively.

- **Line Outage**

The line outage simulation is commonly implemented for the available transfer capability (ATC) evaluation that investigates the impacts of line outage on the power flow distribution within a power grid. The sensitivity-based method [26] for ATC assessment is applied for its simplicity and accuracy, and the basic idea is to simulate the impacts of line outage by adding an appropriate set of power injection perturbations at the line terminals in the pre-outage condition. Fig. 3.3 depicts the pre-outage, post-outage, and equivalent representations when the line from bus i to bus j is tripped. From Fig. 3.3 (a) and (c), the active power flow balance at bus i gives:

$$P_i = P_{ia} + P_{ij} \tag{3.19}$$

$$P'_i = P'_{ia} + P'_{ij} \tag{3.20}$$

Then the change in the net active power flow at bus i is:

$$\Delta P_i = P'_i - P_i = \left(P'_{ia} - P_{ia}\right) + \left(P'_{ij} - P_{ij}\right) = \Delta P_{ia} + \Delta P_{ij} \tag{3.21}$$

Comparing Fig. 3.3 (a) and (b) gives:

$$P_i = P_{ia} + P_{ij} = P'_{ia} \tag{3.22}$$

which is equivalent to:

$$\Delta P_{ia} = P'_{ia} - P_{ia} = P_{ij} \tag{3.23}$$

Substituting (3.23) into (3.21) gives:

$$\Delta P_{ij} = \Delta P_i - P_{ij} \tag{3.24}$$

where ΔP_i is the equivalent power injection perturbation added at bus i for the purpose of simulating the impacts of line outage on the remaining system. After ΔP_i is appended to bus i, the equivalent system can be formed, as shown in Fig. 3.3(c). It is desirable that the equivalent system can present a good match in the active power flow over the line from bus i to bus j compared to the post-outage system. In (3.24), ΔP_{ij} can be approximated by a linear combination of all power injection perturbations at the line terminals defined by:

$$\Delta P_{ij} = \frac{\partial P_{ij}}{\partial P_i}\Delta P_i + \frac{\partial P_{ij}}{\partial P_j}\Delta P_j + \frac{\partial P_{ij}}{\partial Q_i}\Delta Q_i + \frac{\partial P_{ij}}{\partial Q_j}\Delta Q_j \tag{3.25}$$

Substituting (3.25) into (3.24) gives:

$$\left(\frac{\partial P_{ij}}{\partial P_i} - 1\right)\Delta P_i + \frac{\partial P_{ij}}{\partial P_j}\Delta P_j + \frac{\partial P_{ij}}{\partial Q_i}\Delta Q_i + \frac{\partial P_{ij}}{\partial Q_j}\Delta Q_j = -P_{ij} \tag{3.26}$$

The same algorithm is applied to bus j. Then the following equation is solved for the equivalent power injection perturbations at the line terminal buses:

$$\begin{bmatrix} \frac{\partial P_{ij}}{\partial P_i} - 1 & \frac{\partial P_{ij}}{\partial P_j} & \frac{\partial P_{ij}}{\partial Q_i} & \frac{\partial P_{ij}}{\partial Q_j} \\ \frac{\partial P_{ji}}{\partial P_i} & \frac{\partial P_{ji}}{\partial P_j} - 1 & \frac{\partial P_{ji}}{\partial Q_i} & \frac{\partial P_{ji}}{\partial Q_j} \\ \frac{\partial Q_{ij}}{\partial P_i} & \frac{\partial Q_{ij}}{\partial P_j} & \frac{\partial Q_{ij}}{\partial Q_i} - 1 & \frac{\partial Q_{ij}}{\partial Q_j} \\ \frac{\partial Q_{ji}}{\partial P_i} & \frac{\partial Q_{ji}}{\partial P_j} & \frac{\partial Q_{ji}}{\partial Q_i} & \frac{\partial Q_{ji}}{\partial Q_j} - 1 \end{bmatrix} \begin{bmatrix} \Delta P_i \\ \Delta P_j \\ \Delta Q_i \\ \Delta Q_j \end{bmatrix} = \begin{bmatrix} -P_{ij} \\ -P_{ji} \\ -Q_{ij} \\ -Q_{ji} \end{bmatrix} \tag{3.27}$$

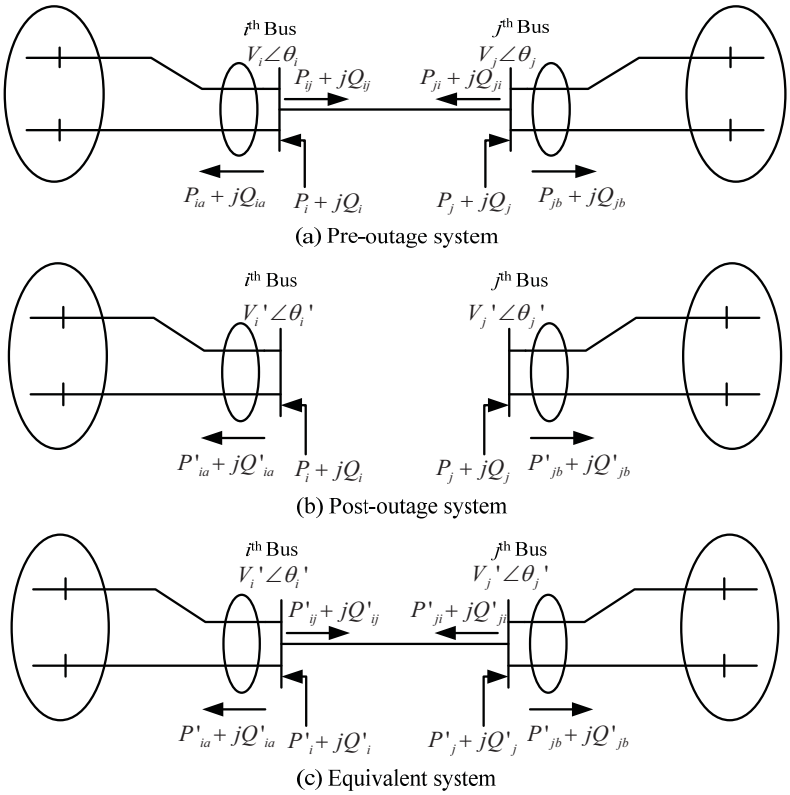

Fig. 3.3 Simulation of line outage.

Because the structure of the equivalent system is identical to that in the pre-outage system, the elements of the coefficient matrix in (3.27) can be obtained directly from the pre-outage system. For instance, at the base case, the active power over the line from bus *i* to bus *j* measured at bus *i* is:

$$P_{ij} = V_i^2 g_{ij} - V_i V_j \left(g_{ij} \cos\theta_{ij} + b_{ij} \sin\theta_{ij} \right) \tag{3.28}$$

where g_{ij} and b_{ij} are the primitive line conductance and susceptance, respectively. Obtaining the partial derivative of (3.28) with respect to P_i gives:

$$\frac{\partial P_{ij}}{\partial P_i} = \left(\frac{\partial P_{ij}}{\partial \theta_i}\right)\left(\frac{\partial \theta_i}{\partial P_i}\right) + \left(\frac{\partial P_{ij}}{\partial \theta_j}\right)\left(\frac{\partial \theta_j}{\partial P_i}\right) + \left(\frac{\partial P_{ij}}{\partial V_i / V_i}\right)\left(\frac{\partial V_i / V_i}{\partial P_i}\right) + \left(\frac{\partial P_{ij}}{\partial V_j / V_j}\right)\left(\frac{\partial V_j / V_j}{\partial P_i}\right) \tag{3.29}$$

where $\partial\theta_i/\partial P_i$, $\partial\theta_j/\partial P_i$, $(\partial V_i/V_i)/\partial P_i$, and $(\partial V_j/V_j)/\partial P_i$ can be readily obtained from **S** in (3.10). $\partial P_{ij}/\partial\theta_i$, $\partial P_{ij}/\partial\theta_j$, $\partial P_{ij}/(\partial V_i/V_i)$, and $\partial P_{ij}/(\partial V_j/V_j)$ can be calculated with the line parameters and terminal voltages at the base case known.

Because the line terminals are modeled as load buses in stability analysis, the power injection perturbations obtained from (3.27) are then appended to the corresponding buses in the same manner as shown in (3.17) and (3.18).

- **Line Addition**

An identical procedure as in the line outage case can be developed for the case of line addition. The approach to estimate the new system state after the line from bus *i* to bus *j* is closed is depicted in Fig. 3.4. As seen from Fig. 3.4(a) and (c), the active power flow balance at bus *i* gives:

$$P_i = P_{ia} \tag{3.30}$$

$$P'_i = P'_{ia} \tag{3.31}$$

The changes in the net active power injection at the bus *i* is:

$$\Delta P_i = P'_i - P_i = \left(P'_{ia} - P_{ia}\right) = \Delta P_{ia} \tag{3.32}$$

Comparing Fig. 3.4(a) and (b) gives:

$$P'_{ia} + P'_{ij} = P_i = P_{ia} \tag{3.33}$$

which is equivalent to:

$$\Delta P_{ia} = P'_{ia} - P_{ia} = -P'_{ij} \tag{3.34}$$

Substituting (3.34) into (3.32) gives:

$$\Delta P_i = -P'_{ij} \tag{3.35}$$

In Fig. 3.4(b), the active power flow measured at bus *i* is:

$$P'_{ij} = P_{ij0} + \Delta P_{ij0} \tag{3.36}$$

It can be seen that P'_{ij} can be divided into the following components:

- P_{ij0} is a hypothetical quantity representing the active power over the line if it is in service as shown in Fig. 3.4(a) which is defined as:

$$P_{ij0} = V_i^2 g_{ij} - V_i V_j \left(g_{ij} \cos\theta_{ij} + b_{ij} \sin\theta_{ij} \right) \tag{3.37}$$

- ΔP_{ij0} is a hypothetical quantity that represents the perturbation of line active power flow resulting from the voltage deviations at bus *i* and bus *j* as the line is closed. This hypothetical quantity is modeled as the equivalent power injection perturbation to the original system in the following form:

$$\Delta P_{ij0} = \frac{\partial P_{ij0}}{\partial P_i}\Delta P_i + \frac{\partial P_{ij0}}{\partial P_j}\Delta P_j + \frac{\partial P_{ij0}}{\partial Q_i}\Delta Q_i + \frac{\partial P_{ij0}}{\partial Q_j}\Delta Q_j \tag{3.38}$$

Substituting (3.36), (3.37), and (3.38) into (3.32) gives:

$$\left(\frac{\partial P_{ij0}}{\partial P_i} + 1 \right)\Delta P_i + \frac{\partial P_{ij0}}{\partial P_j}\Delta P_j + \frac{\partial P_{ij0}}{\partial Q_i}\Delta Q_i + \frac{\partial P_{ij0}}{\partial Q_j}\Delta Q_j = -P_{ij0} \tag{3.39}$$

A similar algorithm is applied to bus *j*. Then the following equation is solved for the equivalent power injection perturbations at the line terminals:

$$\begin{bmatrix} \frac{\partial P_{ij0}}{\partial P_i}+1 & \frac{\partial P_{ij0}}{\partial P_j} & \frac{\partial P_{ij0}}{\partial Q_i} & \frac{\partial P_{ij0}}{\partial Q_j} \\ \frac{\partial P_{ji0}}{\partial P_i} & \frac{\partial P_{ji0}}{\partial P_j}+1 & \frac{\partial P_{ji0}}{\partial Q_i} & \frac{\partial P_{ji0}}{\partial Q_j} \\ \frac{\partial Q_{ij0}}{\partial P_i} & \frac{\partial Q_{ij0}}{\partial P_j} & \frac{\partial Q_{ij0}}{\partial Q_i}+1 & \frac{\partial Q_{ij0}}{\partial Q_j} \\ \frac{\partial Q_{ji0}}{\partial P_i} & \frac{\partial Q_{ji0}}{\partial P_j} & \frac{\partial Q_{ji0}}{\partial Q_i} & \frac{\partial Q_{ji0}}{\partial Q_j}+1 \end{bmatrix} \begin{bmatrix} \Delta P_i \\ \Delta P_j \\ \Delta Q_i \\ \Delta Q_j \end{bmatrix} = \begin{bmatrix} -P_{ij0} \\ -P_{ji0} \\ -Q_{ij0} \\ -Q_{ji0} \end{bmatrix} \tag{3.40}$$

Similar to the case of line outage, all the elements in the coefficient matrix in (3.40) can be obtained from the base case.

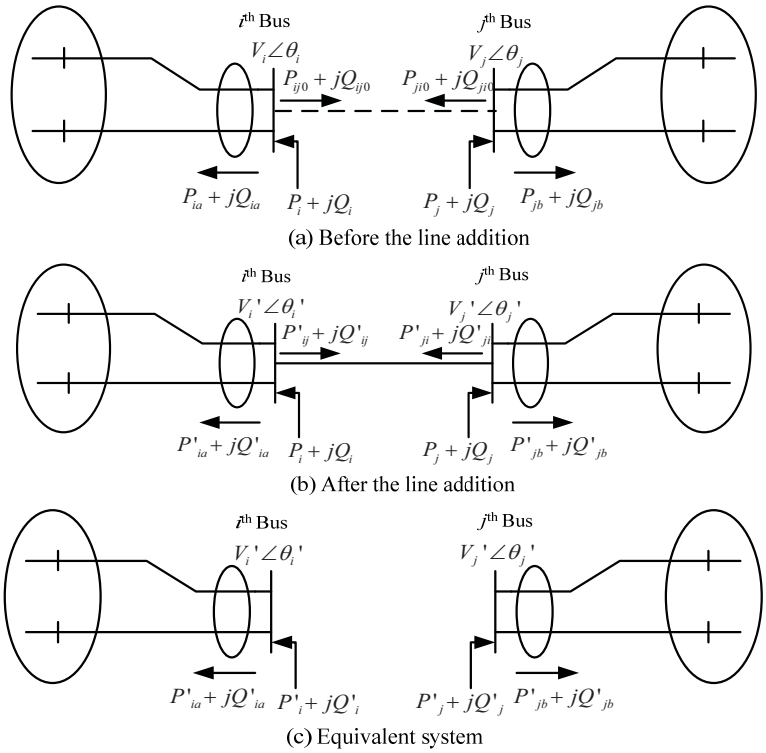

Fig. 3.4 Simulation of line addition.

3.3.2 System Admittance Matrix Perturbation

For a system topology change, a procedure based on the Householder's theorem [27] is also applied to evaluate the perturbation of the system admittance matrix that is reduced to the generator internal buses. When augmenting the network admittance matrix with the generator transient reactances, the full system admittance matrix can be written as:

$$\mathbf{Y}=\begin{bmatrix}\mathbf{Y}_A & \mathbf{Y}_B\\ \mathbf{Y}_C & \mathbf{Y}_D\end{bmatrix}=\left[\begin{array}{c|c|c}\mathbf{Y}_{II} & \mathbf{Y}_{IG} & \mathbf{0}\\ \hline \mathbf{Y}_{GI} & \mathbf{Y}_{GG}' & \mathbf{Y}_{GL}\\ \hline \mathbf{0} & \mathbf{Y}_{LG} & \mathbf{Y}_{LL}\end{array}\right] \tag{3.41}$$

where subscript *I*, *G*, and *L* denote to the generator internal buses, the generator terminal buses, and the load buses. Then the system admittance matrix reduced to generator internal buses is:

$$\mathbf{Y}_{red} = \mathbf{Y}_A - \mathbf{Y}_B \mathbf{Y}_D^{-1} \mathbf{Y}_C \tag{3.42}$$

The system typology change can be represented by the modification to $\mathbf{Y}_D$, which can be expressed as:

$$\Delta \mathbf{Y}_D = \mathbf{KDL} \tag{3.43}$$

Suppose the line from bus *i* to bus *j* is modified, **K**, **D**, and **L** in (3.43) are defined as:

$$\mathbf{L} = \mathbf{K}^T = \begin{bmatrix} 0 & 1 & 0 & \ldots & 0 & 1 & 0 \\ 0 & 1 & 0 & \ldots & 0 & -1 & 0 \end{bmatrix} \tag{3.44}$$

$$\uparrow i^{th}\ element \quad \uparrow j^{th}\ element$$

$$\mathbf{D} = \begin{cases} diag\left(\dfrac{-2y_{ij} - c_{ij}}{2}, \quad \dfrac{-c_{ij}}{2} \right) & \text{for line outage} \\ diag\left(\dfrac{2y_{ij} + c_{ij}}{2}, \quad \dfrac{c_{ij}}{2} \right) & \text{for line addition} \end{cases} \tag{3.45}$$

where y_{ij} is the primitive line admittance, and c_{ij} is the half line charging susceptance. Then the perturbation of $\mathbf{Y}_{red}$ associated with the system typology change is given by:

$$\Delta \mathbf{Y}_{red} = \mathbf{Y}_B \mathbf{Y}_D^{-1} \mathbf{K} \left(\mathbf{D}^{-1} + \mathbf{L} \mathbf{Y}_D^{-1} \mathbf{K} \right)^{-1} \mathbf{L} \mathbf{Y}_D^{-1} \mathbf{Y}_C \tag{3.46}$$

Because $\mathbf{Y}_B$, $\mathbf{Y}_C$, and $\mathbf{Y}_D$ are the same as in the base case, the impact of system topology change on the reduced system admittance matrix can be easily determined from (3.46).

3.3.3 System State Matrix Perturbation

As the perturbations of the system variables (e.g. generator internal voltage and rotor angle) and the perturbation of reduced system admittance matrix are known, the perturbation of the synchronizing power coefficient matrix ***K*** can be obtained by ignoring the higher order terms of the Taylor series:

$$\begin{aligned}\Delta K_{ij}\big|_{i\neq j} = &-\left(\Delta E_i E_j + E_i \Delta E_j\right)\left(-G_{ij}\sin\delta_{ij} + B_{ij}\cos\delta_{ij}\right) \\ &- E_i E_j\left(-G_{ij}\cos\delta_{ij} - B_{ij}\sin\delta_{ij}\right)\left(\Delta\delta_i - \Delta\delta_j\right) \\ &- E_i E_j\left(-\Delta G_{ij}\sin\delta_{ij} + \Delta B_{ij}\cos\delta_{ij}\right)\end{aligned} \tag{3.47}$$

$$\Delta K_{ii} = -\sum_{j=1, j\neq i}^{n_G} \Delta K_{ij} \tag{3.48}$$

Then the perturbation of the system state matrix for the new system condition is:

$$\Delta \mathbf{A}_{sys} = \begin{bmatrix} \mathbf{0} & \mathbf{0} \\ -\mathbf{M}^{-1}\Delta\mathbf{K} & \mathbf{0} \end{bmatrix} \tag{3.49}$$

3.3.4 Slow Coherency Index Perturbation

For different operating conditions, the key to predicting the changes in generator slow coherency is to estimate the new right eigenvectors associated with the slow modes selected. As $\Delta\mathbf{A}_{sys}$ is known from previous steps, a predictor and corrector based approach is applied.

- **Predictor**

Given $\Delta\mathbf{A}_{sys}$ in (3.49), the sensitivities of the eigenvalue and right eigenvector of the i^{th} slow mode are given by [28]:

$$\Delta\lambda_i = \boldsymbol{\psi}_i \Delta\mathbf{A}_{sys}\boldsymbol{\phi}_i \tag{3.50}$$

$$\Delta\boldsymbol{\phi}_i = -\left(\mathbf{A}_{sys} - \lambda_i\mathbf{I} + \boldsymbol{\phi}_i\boldsymbol{\phi}_i^H\right)\left(\Delta\mathbf{A}_{sys} + \Delta\lambda_i\mathbf{I}\right)\boldsymbol{\phi}_i \tag{3.51}$$

Then the new eigensolution can be approximated by:

$$\lambda'_i = \lambda_i + \Delta\lambda_i \tag{3.52}$$

$$\boldsymbol{\phi}'_i = \boldsymbol{\phi}_i + \Delta\boldsymbol{\phi}_i \tag{3.53}$$

It can be seen that a unit step length along the direction of $\Delta\lambda_i$ and $\Delta\boldsymbol{\phi}_i$ is used in (3.52) and (3.53). Assuming that the system state matrix under the new operating condition is $\mathbf{A}'_{sys} = \mathbf{A}_{sys}+\Delta\mathbf{A}_{sys}$, the following mismatch of the predictor procedure needs to be justified:

$$\Delta\mathbf{G} = \mathbf{A}'_{sys}\boldsymbol{\phi}'_i - \lambda'_i\boldsymbol{\phi}'_i \tag{3.54}$$

- **Corrector**

To drive (3.54) to zero, the first-order estimate is applied as follows:

$$\left(\mathbf{A}'_{sys} - \lambda'_i\mathbf{I}\right)\Delta\boldsymbol{\phi}'_i - \boldsymbol{\phi}'_i\Delta\lambda'_i + \Delta\mathbf{G} = \mathbf{0} \tag{3.55}$$

For the unit normalization constraint on the right eigenvector, the following equation also holds:

$$\boldsymbol{\phi}'^H_i\Delta\boldsymbol{\phi}'_i = 0 \tag{3.56}$$

Combining (3.55) and (3.56), a set of complex equations is formed to solve for the eigensolution sensitivities indicating the descent direction for $\Delta\mathbf{G}$, which is given by:

$$\begin{bmatrix} \mathbf{A}'_{sys} - \lambda'_i\mathbf{I} & -\boldsymbol{\phi}'_i \\ \boldsymbol{\phi}'^H_i & 0 \end{bmatrix}\begin{bmatrix} \Delta\boldsymbol{\phi}'_i \\ \Delta\lambda'_i \end{bmatrix} = \begin{bmatrix} -\Delta\mathbf{G} \\ 0 \end{bmatrix} \tag{3.57}$$

Assuming that the step length along the direction of $\Delta\boldsymbol{\phi}'_i$ and $\Delta\lambda'_i$ is a, the best estimate of the new eigensolution can be achieved when the following norm function is minimized:

$$f(a) = \left\| \mathbf{A}'_{sys} \left(\boldsymbol{\phi}'_i + \Delta\boldsymbol{\phi}'_i a \right) - \left(\lambda'_i + \Delta\lambda'_i a \right) \left(\boldsymbol{\phi}'_i + \Delta\boldsymbol{\phi}'_i a \right) \right\|^2 \tag{3.58}$$

Neglecting the higher order term of $(\Delta\lambda'_i a)(\Delta\boldsymbol{\phi}'_i a)$ gives:

$$f(a) = \left(\Delta\mathbf{G} + \mathbf{e}_i a \right)^H \left(\Delta\mathbf{G} + \mathbf{e}_i a \right) \tag{3.59}$$

where $\mathbf{e}_i = \mathbf{A}'_{\text{sys}}\Delta\boldsymbol{\phi}'_i - \lambda'_i\,\Delta\boldsymbol{\phi}'_i - \Delta\lambda'_i\,\boldsymbol{\phi}'_i$. To minimize (3.59), the following necessary condition needs to be satisfied:

$$\frac{\partial}{\partial a}\left(\left(\Delta\mathbf{G} + \mathbf{e}_i a \right)^H \left(\Delta\mathbf{G} + \mathbf{e}_i a \right) \right) = 0 \tag{3.60}$$

Then the optimal step length a_{opt} that minimizes f (a) in (3.59) is:

$$a_{opt} = -\left(\mathbf{e}_i^H \mathbf{e}_i \right)^{-1} \text{Re}\left(\Delta\mathbf{G}^H \mathbf{e}_i \right) \tag{3.61}$$

From (3.59) and (3.61), it can be easily proven that $\mathbf{e}_i = -\Delta\mathbf{G}$ and $a_{opt} = 1.0$. Then the updated estimate of the new eigensolutions can be formed as:

$$\lambda''_i = \lambda'_i + a_{opt}\Delta\lambda'_i = \lambda'_i + \Delta\lambda'_i \tag{3.62}$$

$$\boldsymbol{\phi}''_i = \boldsymbol{\phi}'_i + a_{opt}\Delta\boldsymbol{\phi}'_i = \boldsymbol{\phi}'_i + \Delta\boldsymbol{\phi}'_i \tag{3.63}$$

It is to be noted that the above estimate may not necessarily lead to the minimum error term defined in (3.58) due to the approximation made in (3.59). Then the corrector procedure needs to be conducted iteratively until the norm of $\Delta\mathbf{G}$ decreases to an acceptable value. In each iteration, λ'_i and $\boldsymbol{\phi}'_i$ in (3.54) and (3.57) are substituted by λ''_i and $\boldsymbol{\phi}''_i$ from (3.62) and (3.63), respectively. Because the

estimate from the predictor procedure is very close to the exact solution, only a few iterations will be needed.

As the best estimates of the right eigenvectors are known, the new generator slow coherency indices within the system can be calculated. The critical generators in the initial external area that become slowly coherent with the initially retained generators in the study area can be identified.

3.3.5 Boundary Adjustment Algorithm

When determining an appropriate retained area boundary, the breath-first-search (BFS) algorithm [29] is applied to search for the paths consisting of the minimum set of buses connecting the identified critical generators to the study area. An example of the proposed algorithm is illustrated in Fig. 3.5.

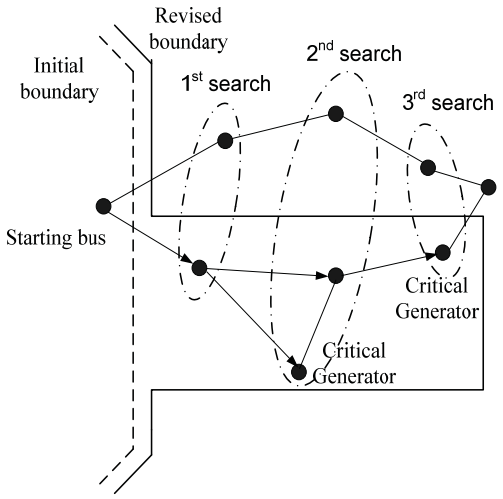

Fig. 3.5 BFS-based boundary determination method.

As shown in Fig. 3.5, the path searching algorithm starts from a specified bus in the study area. At each search step, all the subsequent buses directly connected to the non-targeted buses that are found at the previous step are identified. The searching procedure terminates when all the targeted buses are

found. Finally, all the buses in the successful paths from the starting buses to the targeted buses are retained, leading to new retained area boundary. This approach has the advantage of limiting the size of the subsystem to be retained. For the application to large-scale power systems, this advantage is a desired feature in dynamic equivalents when a high reduction ratio is required.

In the final step, the network and coherent generators in the newly defined external area are equivalenced in DYNRED, and the specific equivalent model that corresponds to the new operating condition can be formed.

3.4 Test Case Verification

A portion of the WECC system consisting of 5186 buses is used to verify the effectiveness of the proposed algorithm. The simplified representation of the test system is shown in Fig. 3.6.

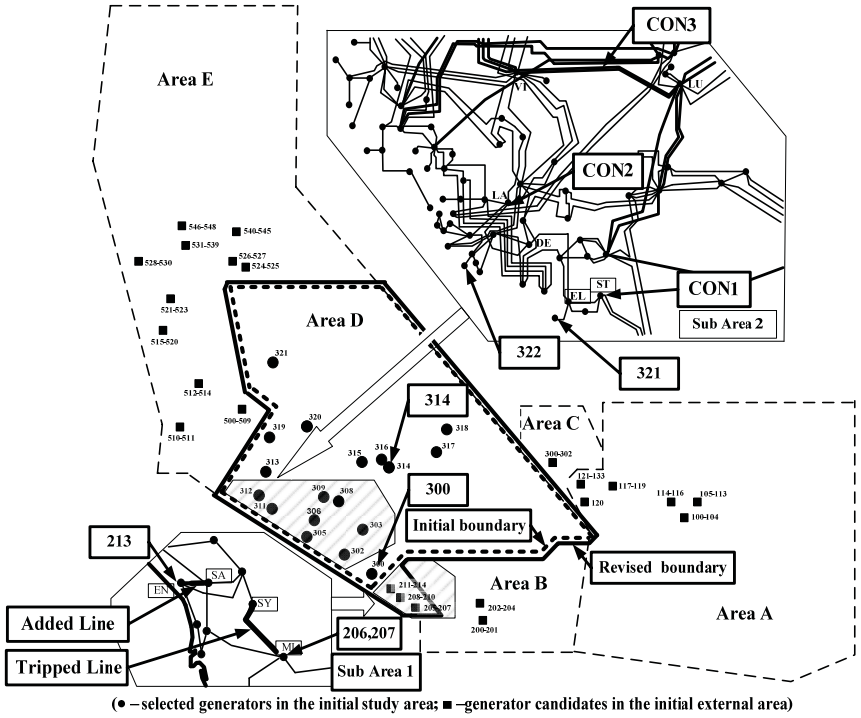

Fig. 3.6 Diagram of WECC test system [30].

The system has a total generation of 78170 MW and 9374 MVAr and a total load of 75972 MW and 11666 MVAr. The detailed generator models with exciters, governors, and PSSs are used if applicable. Area D is defined as the initial study area, and the remaining system is referred to as the initial external area. For evaluating the generator slow coherency, a total of 45 slowest modes are selected.

3.4.1 Slow Coherency Index Estimation Accuracy

Four cases are analyzed to verify the accuracy of the slow coherency index estimation. The exact (evaluated by repeat calculation) and estimated (evaluated by applying the proposed procedure) slow coherency indices of generator 213 with respect to the selected generators in the study area are compared in Fig. 3.7-Fig. 3.10.

- *Case1*: The loads in Sub Area 1 increase by 250 MW, and the generation of generator 213 and 206 increases by 100 MW and 150 MW, respectively.

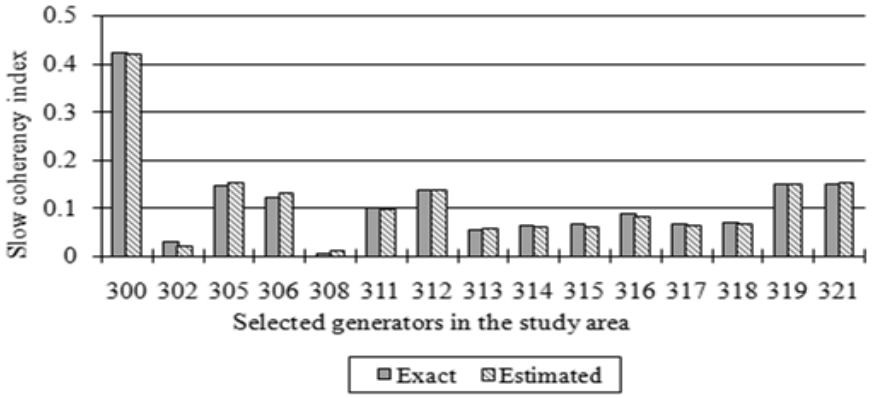

Fig. 3.7 Slow coherency indices of generator 213 for Case 1

- *Case2*: the generation of generator 213 reduces by 200 MW, and both generator 206 and 207 pick up this change equally.

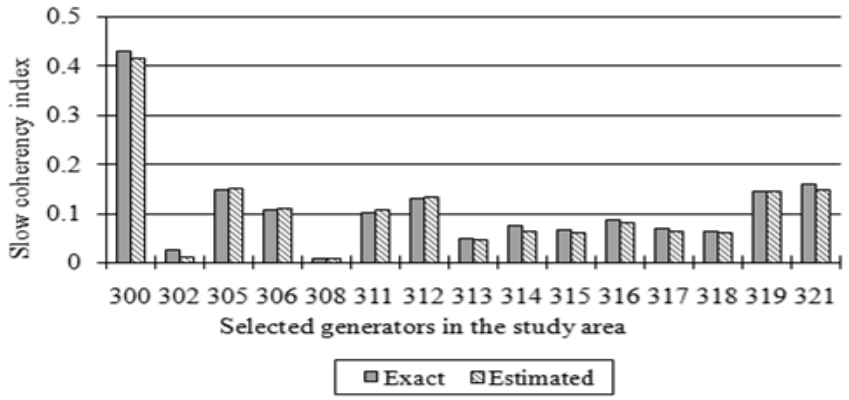

Fig. 3.8 Slow coherency indices of generator 213 for Case 2.

- *Case3*: The 230 kV transmission line from bus SY to bus MI is tripped.

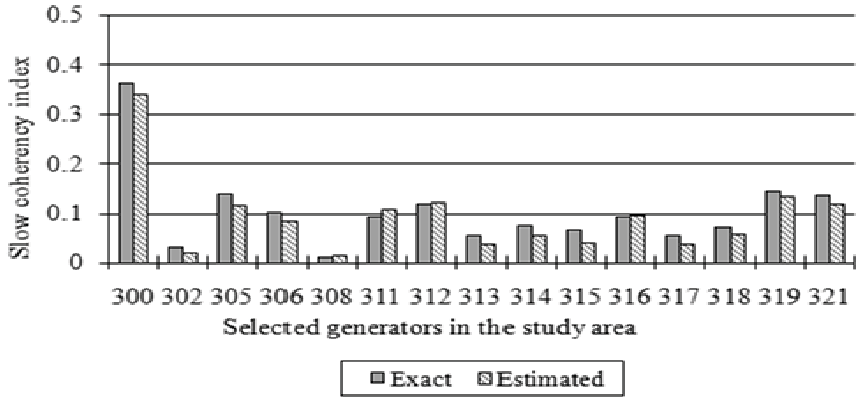

Fig. 3.9 Slow coherency indices of generator 213 for Case 3.

- *Case4*: The 230 kV transmission line from bus EN to bus SA is added.

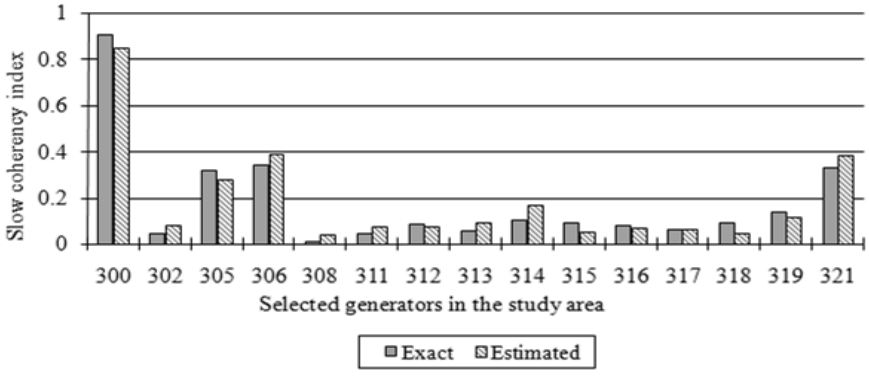

Fig. 3.10 Slow coherency indices of generator 213 for Case 4.

From the test cases, it can be concluded that the proposed approach is effective in capturing the significant changes in generator slow coherency. In Case 4, for example, the prediction of the slow coherency indices of generator 300, 305, 306, and 321 shows a good match compared to the exact values. The relatively larger errors in the line outage and addition cases are mainly due to the nonlinearity presented by the system that is ignored in the proposed algorithm. However, the estimation is still accurate enough to identify the critical generators.

3.4.2 Verification of Retained Area Adjustment

Considering Case 4 in the previous section, the proposed approach is applied. As shown in Fig. 3.6, the generators having PTDFs greater than 0.35 and the capacity greater than 50MVA are selected as the candidates in the initial external area. Using 0.80 as the threshold, generator 205-214 with a total capacity of 1935 MVA are found to become slowly coherent with the generators in the initial study area after the line EN-SA is added. After running BFS-based program to determine the expanded retained area, 26 buses located in the initial external area are identified, leading to the revised retained area boundary, as shown in Fig. 3.6. Accordingly, a new equivalent system is formed. The scale of the new equivalent system is summarized in Table 3-1.

Table 3-1 Summary of new equivalent system

	Buses	Lines	Loads	Generators in entire syst.	Generators in external area
Full syst.	5186	6953	2794	567	431
New equivalent syst.	1208	2253	574	264	119
% of full syst.	23.3%	32.4%	20.5%	46.6%	27.6%

From Table 3-1, it is observed that a significant reduction in the system size can be achieved when the new equivalent system is applied. For example, 53.4% of the generators in the full system representation have been successfully eliminated after dynamic equivalencing. This reduction ratio is even higher when only the generators in the external area are considered. As the number of generators decreases in the equivalent system, the computational effort required for the time-domain simulation ought to be reduced. The computational time for completing the proposed approach is compared to formation of the equivalent from the start in DYNRED, as listed in Table 3-2.

Table 3-2 Comparison of building dynamic equivalents

Steps	Proposed method	DYNRED
Form and calculate state matrix	3.8 s	11.0 s
Group coherent generators	1.1 s	2.3 s
Build equivalent system	2.4 s	2.4s
Total	7.3 s	15.7s

It can be seen from Table 3-2 that the proposed method allows a saving of 65.5% of the computational time in comparison to DYNRED when forming the system state matrix and solving for the eigensolutions on an Intel Core2 Duo Processor T6700 (2.66GHz) PC with 2 GB of RAM. Because the calculation of each mode is independent of other modes in the proposed approach, further improvement can be achieved using parallel computation. The iteration count for calculating each slow mode of interest in the corrector step is shown in Fig. 3.11.

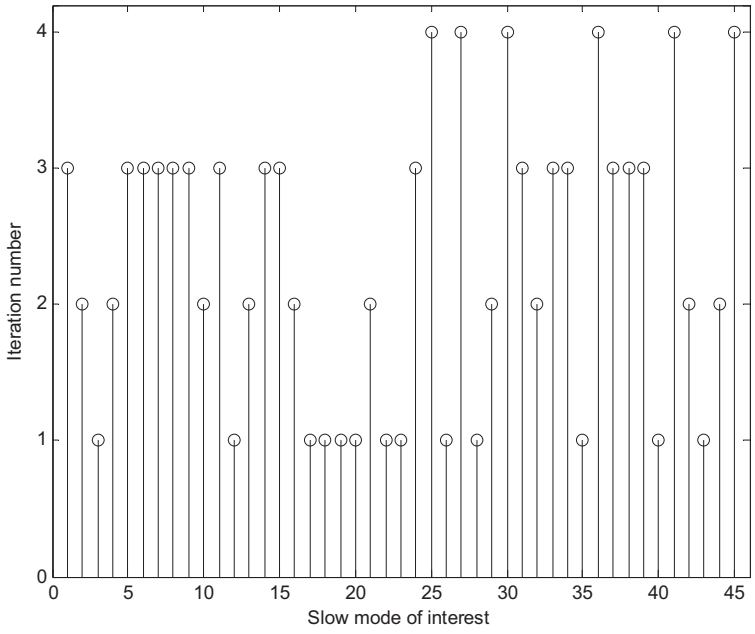

Fig. 3.11 Iteration count in the corrector step.

It can be concluded from Fig. 3.11 that for half the slow modes, the eigensolutions can be obtained in less two iterations; and even in the worst cases, four iterations are required at the most. To verify the equivalencing accuracy, the following three 20-second simulations are conducted:

- *CON1*: a three-phase fault is applied on the ST 230 kV bus in Sub Area 2 at 1 s, and it is cleared after 12 cycles by tripping the 230 kV line from ST to EL;
- *CON2*: a three-phase fault is applied on the LA 230 kV bus in Sub Area 2 at 1 s, and it is cleared after 12 cycles by tripping the 230 kV line from LA to DE;
- *CON3*: a three-phase to ground fault is applied at the middle of the 500 kV line from VI to LU at 1 s, and it is cleared after 4 cycles by tripping the entire line.

For each scenario, the root mean square error (RMSE) [8] is calculated to measure the response mismatch between the full system and equivalent system. For generator *i*, the RMSE is defined as:

$$RMSE = \sqrt{\frac{1}{T}\int_0^T \left|\Delta\delta_i^{full}(t) - \Delta\delta_i^{equ}(t)\right|^2 dt} \quad (in \text{ deg.}) \tag{3.64}$$

where $\Delta\delta_i^{full}$ and $\Delta\delta_i^{equ}$ are the relative rotor angle deviations of generator *i* obtained from the full system and equivalent system, respectively, and *T* is the simulation duration time.

For the tested contingencies, the RMSEs of the selected generators are summarized in Table 3-3. The initial equivalent system is formed using the initial study area definition, as shown in Fig. 3.6.

Table 3-3 Comparison of RMSEs

Generator number		300	314	320	321	322
RMSEs for CON1	Initial equivalent syst.	4.33	1.79	0.57	0.79	1.54
	New equivalent syst.	1.60	0.73	0.55	0.30	0.87
RMSEs for CON2	Initial equivalent syst.	1.79	0.85	0.55	0.39	0.98
	New equivalent syst.	0.97	0.83	0.46	0.21	0.90
RMSEs for CON3	Initial equivalent syst.	1.09	0.99	0.63	0.29	0.78
	New equivalent syst.	0.95	0.96	0.58	0.24	0.76

From Table 3-3, it is seen that an improvement in the equivalencing accuracy can be obtained when the new equivalent system based on the revised retained area boundary is used. However, this improvement varies for different contingencies. For CON1, the largest reduction in RMSEs is 2.73 for generator 300; while for CON2 and CON3, the improvements are not significant. This finding is consistent with the fact that CON1 is much closer to the revised

retained area boundary than other contingences. In addition, the generators close to the revised study area boundary, such as generator 300, 321, and 322, are found to be more sensitive to the study area boundary adjustment for CON1. The relative rotor angle responses of generator 300 and 322 to the system disturbance defined in CON1 are also compared in Fig. 3.12 . A remote generator in Sub Area 2 is chosen as the reference.

The simulations indicate that the generator responses in both equivalent systems match the full system for the first few seconds after the contingency. As dynamic responses evolve, the new equivalent system provides better accuracy than the initial equivalent system later in the simulation. It is also seen from Fig. 3.12 (a) that the new equivalent system presents a more accurate response in terms of damping the rotor angle oscillation of generator 300 than the initial equivalent system. On the same PC as described before, the simulation execution time for CON1 has been reduced from 20.2 s using the full system representation to 9.3 s using the new equivalent system. This improvement can accumulate to a significant time saving when multiple runs of time-domain simulations are needed for on-line DSA.

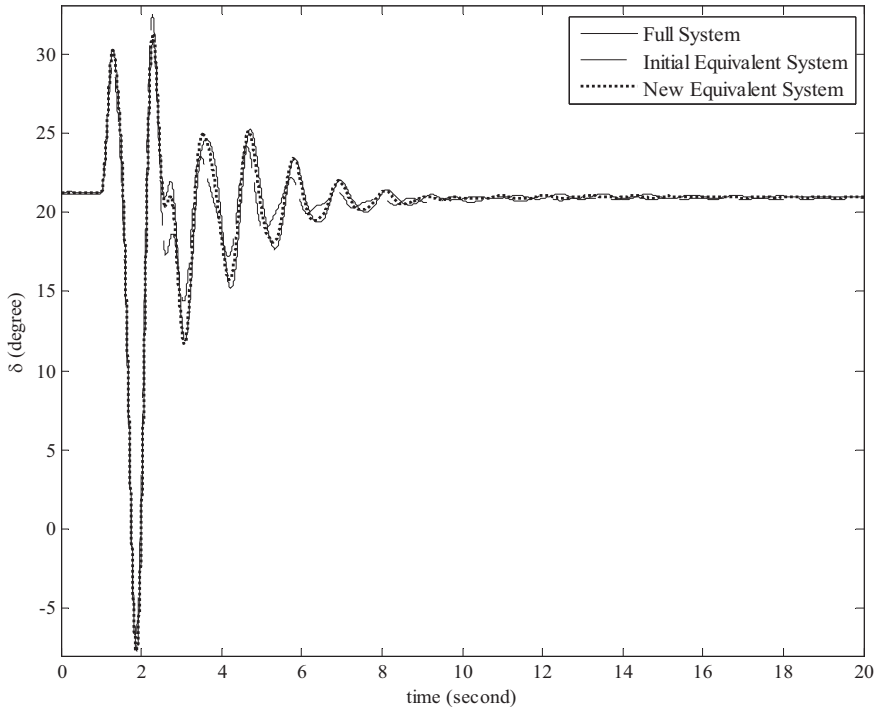

Fig. 3.12 Relative rotor angle responses of generator 300 for CON1

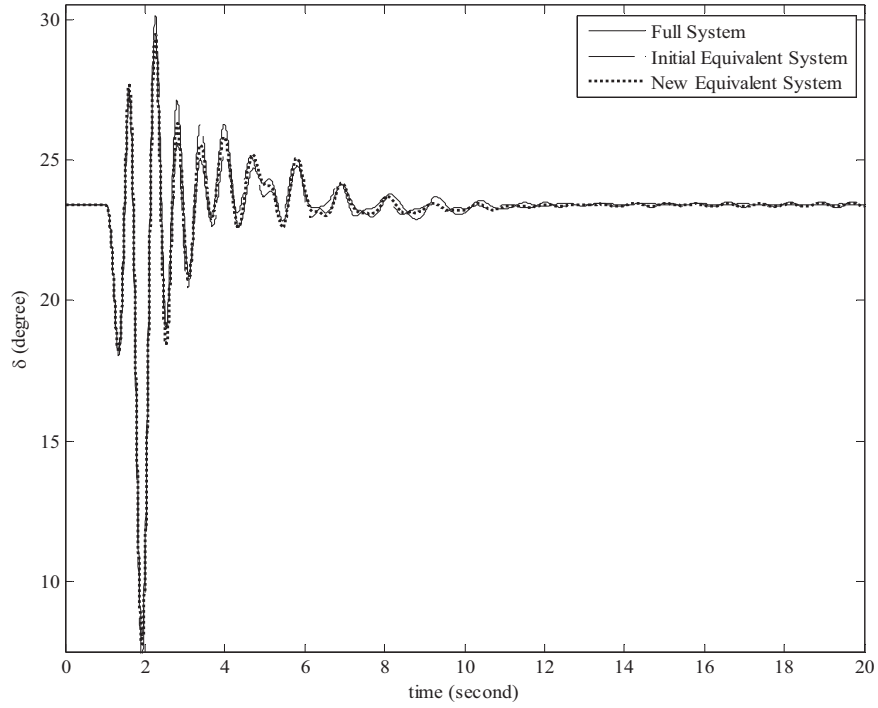

Fig. 3.13 Relative rotor angle responses of generator 322 for CON1

3.5 Conclusion

In this chapter, an eigensensitivity-based approach is proposed to evaluate the changing patterns of generator slow coherency as system operating condition varies. The impacts of load change, generation change, line outage, and line addition have been considered. The critical generators in the initial external area that become slowly coherent with the initial study area are identified and then retained to form a new equivalent system. Without the need to reconstruct system state matrix and calculate eigensolutions from scratch, the proposed approach provides an efficient means to identify the critical operating condition changes that make the adjustment of retained area definition a necessity for better equivalencing accuracy. In addition, the proposed approach also provides an efficient means to capture the changes in coherent generator groups. Therefore, the proposed approach is computationally efficient to form the adaptive dynamic equivalent for different operating conditions.

Chapter 4

HYBRID DYNAMIC EQUIVALENTS

4.1 Background

In forming conventional dynamic equivalents, the coherent generators in the external area are aggregated and replaced by appropriate equivalenced generator models. In this process, there are two factors that mainly contribute to the errors accumulated. First, the dynamic performances of the coherent generators in each group are not necessarily identical. Most of the coherency identification methods are based on the generators modeled with the classical representation, and this simplification might lead weakly coherent generators to be mistakenly grouped into a single group. The authors in [8] pointed out that the excitation system can significantly affect generator dynamic responses following a system disturbance, and more accurate grouping result can be achieved when the effects of exciters and other control systems are taken into account. Second, it is common in a realistic setting that the generators in a given coherent group have different types of exciters, governors, and PSSs. Therefore, it is theoretically infeasible to form a single equivalent generator that is able to represent all the dynamic characteristics of the coherent generators. This is especially true for the classical generator aggregation method [9] because the detailed representations of the available generators are neglected in forming the equivalent generator models. To account for the errors accumulated throughout the coherency identification and generator aggregation process, a large retained area is commonly specified in order to achieve adequate equivalencing accuracy. To address this challenge, two

comprehensive approaches have been proposed in Chapter 2 and 3. However, the test results indicate that the improvement of equivalencing accuracy becomes insignificant when the retained area is already large enough. The accuracy of the equivalent models of the external area could be even more questionable presently as detailed information about the network and component models in the entire system is often inaccessible to a single entity in the restructured environment.

Recently, the ANN technique has been successfully applied to the subject of dynamic equivalents because of its superior capability of capturing arbitrary input-and-output mappings stored in the training samples. The ANN-based equivalent, represented by a set of neural networks, is a "black box" in nature. It only needs the measurements at the retained area boundary buses instead of the detailed model information in the external area. In references [17],[18], [20], and [31], different types of neural networks, such as bottleneck networks and recurrent networks, have been studied. In an attempt to effectively capture the dynamic characteristics of the external area, these efforts show the need for a complicated neural network structure in order to obtain reasonable equivalencing accuracy.

In this chapter, a new hybrid dynamic equivalent model is developed and analyzed as efforts to improve the feasibility of the conventional coherency-based equivalents and at the same time to overcome the disadvantage of complicated structure in ANN-based equivalents. In the proposed hybrid model, the ANN-based equivalent works in conjunction with the coherency-based equivalent and is expected to improve performance of the coherency-based equivalent by providing

desirable supplementary compensation in terms of power injections at all the boundary buses.

4.2 Training Data for ANN-based Equivalent

In Fig. 4.1, the evolution of the proposed hybrid dynamic equivalent is presented. Using the boundary bus voltages as inputs, the ANN-based equivalent dynamically adjusts its power injections at the boundary buses to minimize the voltage response mismatch at the boundary buses between the full system and the conventionally reduced system.

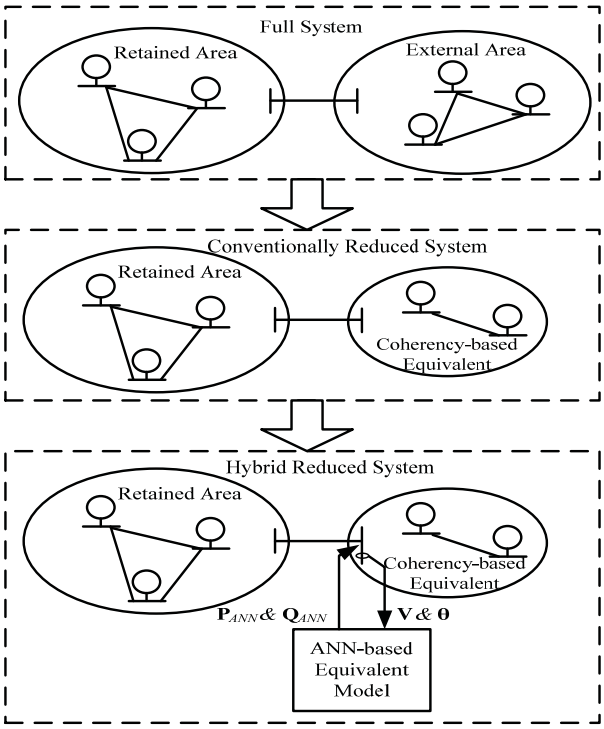

Fig. 4.1 Evolution of the hybrid equivalents.

With a properly trained neural network, the hybrid equivalent is expected to more accurately represent the dynamic characteristics of the external area. It is noted that in the hybrid reduced system, the coherency-based equivalent still plays a dominant role, and the ANN-based equivalent is only used to capture additional

dynamic characteristics that have not been represented in the conventionally reduced system. In addition, the connection configuration of the equivalent allows great flexibility for practical implementation. For example, the hybrid reduced system can convert back to a conventionally reduced system when the ANN-based equivalent is bypassed.

To build the ANN-based equivalent, the voltages at the boundary buses together with the required power injections need to be determined at each time instant. In the literature, the trajectory sensitivity method [32],[33] provides an efficient approach to estimate system variable deviations with respect to system parameter changes without extensively increasing the computational burden. When computing the appropriate power injections of the ANN-based equivalent, the trajectory sensitivity method is applied to determine the gradient direction that reduces the observed mismatch of the boundary voltage responses between the full system and the conventionally reduced system.

4.2.1 Power System Models

A power system can be represented by a set of DAEs as shown below:

$$\begin{cases} \dot{\mathbf{x}} = \mathbf{f}(\mathbf{x}, \mathbf{y}, \beta) \\ \mathbf{0} = \mathbf{g}(\mathbf{x}, \mathbf{y}, \beta) \end{cases} \tag{4.1}$$

where $\mathbf{x}$ is the state variable vector, $\mathbf{y}$ is the algebraic variable vector, and β is a system parameter subject to changes (e.g. load level or generation level). Initially β is set to β_0. The differential equation vector $\mathbf{f}$ represents the dynamics of the system components, and the algebraic equation vector $\mathbf{g}$ represents the power flow balance equation at each bus within the system.

To numerically solve the DAEs in (4.1) for a time-domain simulation, an implicit method like the trapezoidal rule [24] is applied. The application of the trapezoidal rule is as follows. At the time instant n, the following equations need to be solved to determine $\mathbf{x}_n$ and $\mathbf{y}_n$:

$$\begin{cases} \mathbf{F}(\mathbf{x}_n, \mathbf{y}_n) = \mathbf{x}_n - \mathbf{x}_{n-1} - \dfrac{1}{2}\Delta t\left[\mathbf{f}(\mathbf{x}_n, \mathbf{y}_n, \beta) + \mathbf{f}(\mathbf{x}_{n-1}, \mathbf{y}_{n-1}, \beta)\right] = \mathbf{0} \\ \mathbf{G}(\mathbf{x}_n, \mathbf{y}_n) = \mathbf{g}(\mathbf{x}_n, \mathbf{y}_n, \beta) = \mathbf{0} \end{cases} \tag{4.2}$$

where $\mathbf{x}_n$ and $\mathbf{y}_n$ are the state and algebraic variable vectors calculated at the time instant n. Δt is the integration time step. To solve the nonlinear equations in (4.2), the Newton-Raphson (NR) iterative algorithm is used. At the time instant n, the solution derived at the k^{th} iteration is:

$$\begin{bmatrix} \mathbf{x}_n^{k+1} \\ \mathbf{y}_n^{k+1} \end{bmatrix} = \begin{bmatrix} \mathbf{x}_n^{k} \\ \mathbf{y}_n^{k} \end{bmatrix} + \begin{bmatrix} \Delta\mathbf{x}_n^{k} \\ \Delta\mathbf{y}_n^{k} \end{bmatrix} \tag{4.3}$$

In (4.3), $\Delta\mathbf{x}_n^k$ and $\Delta\mathbf{y}_n^k$ are the variable increments at the k^{th} iteration and calculated in the following equation:

$$\begin{bmatrix} \mathbf{I} - \dfrac{\Delta t}{2}\mathbf{f}_{\mathbf{x}}^k & -\dfrac{\Delta t}{2}\mathbf{f}_{\mathbf{y}}^k \\ \mathbf{g}_{\mathbf{x}}^k & \mathbf{g}_{\mathbf{y}}^k \end{bmatrix} \begin{bmatrix} \Delta\mathbf{x}_n^k \\ \Delta\mathbf{y}_n^k \end{bmatrix} = \begin{bmatrix} -\mathbf{F}(\mathbf{x}_n^k, \mathbf{y}_n^k) \\ -\mathbf{G}(\mathbf{x}_n^k, \mathbf{y}_n^k) \end{bmatrix} \tag{4.4}$$

where $\mathbf{f}_{\mathbf{x}}^k = \partial\mathbf{f}/\partial\mathbf{x}$, $\mathbf{f}_{\mathbf{y}}^k = \partial\mathbf{f}/\partial\mathbf{y}$, $\mathbf{g}_{\mathbf{x}}^k = \partial\mathbf{g}/\partial\mathbf{x}$, and $\mathbf{g}_{\mathbf{y}}^k = \partial\mathbf{g}/\partial\mathbf{y}$ are the partial derivative matrices calculated at $\mathbf{x}=\mathbf{x}^k$ and $\mathbf{y}=\mathbf{y}^k$.

The entire iterative process terminates when the increments in (4.4) are smaller than a specified tolerance. It is assumed that the solution converges to $\mathbf{x}=\mathbf{x}_n$ and $\mathbf{y}=\mathbf{y}_n$ after the k^{th} iteration. Then the elements of the coefficient matrices in (4.4) can be denoted as:

$$\mathbf{f}_{\mathbf{x},n} = \left.\frac{\partial \mathbf{f}}{\partial \mathbf{x}}\right|_{\mathbf{x}=\mathbf{x}_n,\mathbf{y}=\mathbf{y}_n} \tag{4.5}$$

$$\mathbf{f}_{\mathbf{y},n} = \left.\frac{\partial \mathbf{f}}{\partial \mathbf{y}}\right|_{\mathbf{x}=\mathbf{x}_n,\mathbf{y}=\mathbf{y}_n} \tag{4.6}$$

$$\mathbf{g}_{\mathbf{x},n} = \left.\frac{\partial \mathbf{g}}{\partial \mathbf{x}}\right|_{\mathbf{x}=\mathbf{x}_n,\mathbf{y}=\mathbf{y}_n} \tag{4.7}$$

$$\mathbf{g}_{\mathbf{y},n} = \left.\frac{\partial \mathbf{g}}{\partial \mathbf{y}}\right|_{\mathbf{x}=\mathbf{x}_n,\mathbf{y}=\mathbf{y}_n} \tag{4.8}$$

4.2.2 Trajectory Sensitivity for Single Parameter

For the initial parameter, namely β_0, the corresponding DAEs in (4.1) have a unique trajectory following a specific system disturbance. Then for any β that is sufficiently close to β_0, the perturbed trajectory solution can be determined by taking the derivatives of the system state and algebraic variables with respect to β, as shown below:

$$\begin{cases} \dfrac{d}{dt}\left(\dfrac{\partial \mathbf{x}}{\partial \beta}\right) = \left(\dfrac{\partial \mathbf{f}}{\partial \mathbf{x}}\right)\left(\dfrac{\partial \mathbf{x}}{\partial \beta}\right) + \left(\dfrac{\partial \mathbf{f}}{\partial \mathbf{y}}\right)\left(\dfrac{\partial \mathbf{y}}{\partial \beta}\right) + \left(\dfrac{\partial \mathbf{f}}{\partial \beta}\right) \\ \mathbf{0} = \left(\dfrac{\partial \mathbf{g}}{\partial \mathbf{x}}\right)\left(\dfrac{\partial \mathbf{x}}{\partial \beta}\right) + \left(\dfrac{\partial \mathbf{g}}{\partial \mathbf{y}}\right)\left(\dfrac{\partial \mathbf{y}}{\partial \beta}\right) + \left(\dfrac{\partial \mathbf{g}}{\partial \beta}\right) \end{cases} \tag{4.9}$$

Assume that $\mathbf{x}_\beta = \partial\mathbf{x}/\partial\beta$, $\mathbf{y}_\beta = \partial\mathbf{y}/\partial_\beta$, $\mathbf{f}_\mathbf{x} = \partial\mathbf{f}/\partial\mathbf{x}$, $\mathbf{f}_\mathbf{y} = \partial\mathbf{f}/\partial\mathbf{y}$, $\mathbf{f}_\beta = \partial\mathbf{f}/\partial\beta$, $\mathbf{g}_\mathbf{x} = \partial\mathbf{g}/\partial\mathbf{x}$, $\mathbf{g}_\mathbf{y} = \partial\mathbf{g}/\partial\mathbf{y}$, and $\mathbf{g}_\beta = \partial\mathbf{g}/\partial\beta$, then (4.9) can be written in a compact form as shown below:

$$\begin{cases} \dot{\mathbf{x}}_\beta = \mathbf{f}_\mathbf{x}\mathbf{x}_\beta + \mathbf{f}_\mathbf{y}\mathbf{y}_\beta + \mathbf{f}_\beta \\ \mathbf{0} = \mathbf{g}_\mathbf{x}\mathbf{x}_\beta + \mathbf{g}_\mathbf{y}\mathbf{y}_\beta + \mathbf{g}_\beta \end{cases} \tag{4.10}$$

It is seen in (4.10) that the sensitivities of **x** and **y** with respect to β at $\beta = \beta_0$ are described by a set of linear DAEs. As in the case of (4.1), the trapezoidal rule is also applied to solve the DAEs in (4.10). Then the sensitivities at the time instant n are given by:

$$\begin{cases} \mathbf{x}_{\beta,n} - \mathbf{x}_{\beta,n-1} - \dfrac{\Delta t}{2}\left[\mathbf{f}_{\mathbf{x},n}\mathbf{x}_{\beta,n} + \mathbf{f}_{\mathbf{y},n}\mathbf{y}_{\beta,n} + \mathbf{f}_{\beta,n} + \mathbf{f}_{\mathbf{x},n-1}\mathbf{x}_{\beta,n-1} + \mathbf{f}_{\mathbf{y},n-1}\mathbf{y}_{\beta,n-1} + \mathbf{f}_{\beta,n-1}\right] = \mathbf{0} \\ \mathbf{g}_{\mathbf{x},n}\mathbf{x}_{\beta,n} + \mathbf{g}_{\mathbf{y},n}\mathbf{y}_{\beta,n} + \mathbf{g}_{\beta,n} = \mathbf{0} \end{cases} \tag{4.11}$$

where $\mathbf{f}_{\mathbf{x},n}$, $\mathbf{f}_{\mathbf{y},n}$, $\mathbf{g}_{\mathbf{x},n}$, and $\mathbf{g}_{\mathbf{y},n}$ are the partial derivative matrices formed at the last iteration in (4.5) - (4.8). To determine the unknowns, namely $\mathbf{x}_{\beta,n}$ and $\mathbf{y}_{\beta,n}$, (4.11) can be re-formulated as:

$$\begin{bmatrix} \mathbf{I} - \dfrac{\Delta t}{2}\mathbf{f}_{\mathbf{x},n} & -\dfrac{\Delta t}{2}\mathbf{f}_{\mathbf{y},n} \\ \mathbf{g}_{\mathbf{x},n} & \mathbf{g}_{\mathbf{y},n} \end{bmatrix} \begin{bmatrix} \mathbf{x}_{\beta,n} \\ \mathbf{y}_{\beta,n} \end{bmatrix} = \begin{bmatrix} \mathbf{x}_{\beta,n-1} + \dfrac{\Delta t}{2}\mathbf{f}_{\beta,n} + \dfrac{\Delta t}{2}\left(\mathbf{f}_{\mathbf{x},n-1}\mathbf{x}_{\beta,n-1} + \mathbf{f}_{\mathbf{y},n-1}\mathbf{y}_{\beta,n-1} + \mathbf{f}_{\beta,n-1}\right) \\ -\mathbf{g}_{\beta,n} \end{bmatrix} \tag{4.12}$$

It is seen from (4.12) that the additional computational effort for trajectory sensitivity calculation is manageable as (1) it is a linear equation; and (2) all the coefficients on the left-hand side can be directly obtained when calculating the initial trajectory with $\beta = \beta_0$ at the same time instant. Based on the specified changing pattern of β, the remaining coefficients can be determined accordingly, which is detailed in Section 4.2.4.

With the variable sensitivities at the time instant n known, the system state and algebraic variables for $\beta = \beta_0 + \Delta\beta$ can be approximated by:

$$\begin{cases} \mathbf{x}_n^{new} = \mathbf{x}_n + \mathbf{x}_{\beta,n}\Delta\beta \\ \mathbf{y}_n^{new} = \mathbf{y}_n + \mathbf{y}_{\beta,n}\Delta\beta \end{cases} \tag{4.13}$$

where $\mathbf{x}_n^{new}$ and $\mathbf{y}_n^{new}$ are the approximations of the system variables for $\beta = \beta_0 + \Delta\beta$.

4.2.3 Trajectory Sensitivity for Multiple Parameters

In a realistic setting, the system operating condition changes constantly in different manners (e.g. generator scheduling, load curtailment, line outage, etc.). Assuming that two system parameters, namely β_1 and β_2, are subject to change simultaneously, the trajectory sensitivity for each system parameter is determined by:

$$\begin{cases} \dot{\mathbf{x}}_{\beta_1} = \mathbf{f}_{\mathbf{x}}\mathbf{x}_{\beta_1} + \mathbf{f}_{\mathbf{y}}\mathbf{y}_{\beta_1} + \mathbf{f}_{\beta_1} \\ \mathbf{0} = \mathbf{g}_{\mathbf{x}}\mathbf{x}_{\beta_1} + \mathbf{g}_{\mathbf{y}}\mathbf{y}_{\beta_1} + \mathbf{g}_{\beta_1} \end{cases} \tag{4.14}$$

$$\begin{cases} \dot{\mathbf{x}}_{\beta_2} = \mathbf{f}_{\mathbf{x}}\mathbf{x}_{\beta_2} + \mathbf{f}_{\mathbf{y}}\mathbf{y}_{\beta_2} + \mathbf{f}_{\beta_2} \\ \mathbf{0} = \mathbf{g}_{\mathbf{x}}\mathbf{x}_{\beta_2} + \mathbf{g}_{\mathbf{y}}\mathbf{y}_{\beta_2} + \mathbf{g}_{\beta_2} \end{cases} \tag{4.15}$$

When the new system parameters are close to their initial values, the higher order terms of the Taylor series of the new system variables can be neglected. Then the approximations of new system variables at the time instant n are given by:

$$\begin{cases} \mathbf{x}_n^{new} = \mathbf{x}_n + \mathbf{x}_{\beta_1,n}\Delta\beta_1 + \mathbf{x}_{\beta_2,n}\Delta\beta_2 \\ \mathbf{y}_n^{new} = \mathbf{y}_n + \mathbf{y}_{\beta_1,n}\Delta\beta_1 + \mathbf{x}_{\beta_2,n}\Delta\beta_2 \end{cases} \tag{4.16}$$

where $\Delta\beta_1$ and $\Delta\beta_2$ are the deviations of the parameter β_1 and β_2, respectively.

4.2.4 Training Set Formulation

As shown in Fig. 4.1, the proposed hybrid dynamic equivalent consists of two parts: the coherency-based equivalent and the ANN-based equivalent. The ANN-based equivalent is designed to compensate for the discrepancy between the full system and the conventionally reduced system formed in DYNRED by providing appropriate power injections at all the boundary buses. To form the

training set for the ANN-based equivalent, the voltages at the connection buses together with the required power injections need to be determined at each time instant. Without loss of generality, it is assumed that the ANN-based equivalent is connected to bus i ($i \in B$ where B denotes the set comprising the boundary buses). An example of how the training data is formulated is depicted in Fig. 4.2.

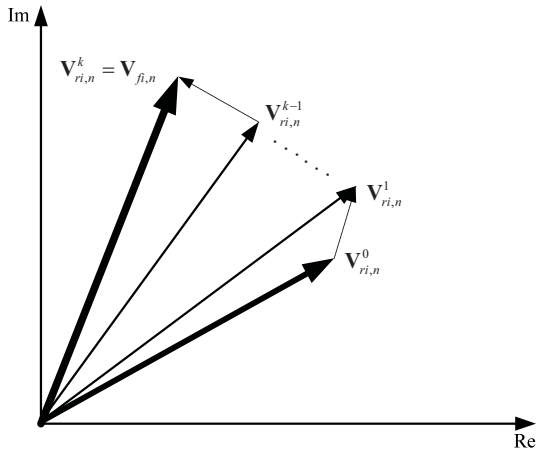

Fig. 4.2 Formulation process of training data.

In Fig. 4.2, $\mathbf{V}_{ri,n}$ and $\mathbf{V}_{fi,n}$ are the complex voltage at bus i at the time instant n, and the subscript r and f denote the reduced system and full system, respectively. At the beginning of the iterative process, the power injections of the ANN-based equivalent at the time instant n are initialized at the values obtained at the time instant n-1. Then the power injections of the ANN-based equivalent are updated in the direction that reduces the observed mismatch of the boundary bus voltage responses between the full system and reduced system. At the k^{th} iteration for instance, the power injections of the ANN-based equivalent at the boundary buses can be determined in the following form:

$$\begin{bmatrix} \mathbf{P}_{ANN,n}^{k+1} \\ \mathbf{Q}_{ANN,n}^{k+1} \end{bmatrix} = \begin{bmatrix} \mathbf{P}_{ANN,n}^{k} \\ \mathbf{Q}_{ANN,n}^{k} \end{bmatrix} + \begin{bmatrix} \Delta\mathbf{P}_{ANN,n}^{k} \\ \Delta\mathbf{Q}_{ANN,n}^{k} \end{bmatrix} \tag{4.17}$$

where $\mathbf{P}_{ANN,n}^{k}$ and $\mathbf{Q}_{ANN,n}^{k}$ are the column vectors that are constituted with $P_{ANNi,n}^{k}$ and $Q_{ANNi,n}^{k}$ ($i \in B$), respectively. The power injection increments of the ANN-based equivalent can be determined uniquely by solving the following linear equation:

$$\begin{bmatrix} \Delta\mathbf{P}_{ANN,n}^{k} \\ \Delta\mathbf{Q}_{ANN,n}^{k} \end{bmatrix} = \begin{bmatrix} \dfrac{\partial \mathbf{V}_{r,n}}{\partial \mathbf{P}_{ANN,n}} & \dfrac{\partial \mathbf{V}_{r,n}}{\partial \mathbf{Q}_{ANN,n}} \\ \dfrac{\partial \boldsymbol{\theta}_{r,n}}{\partial \mathbf{P}_{ANN,n}} & \dfrac{\partial \boldsymbol{\theta}_{r,n}}{\partial \mathbf{Q}_{ANN,n}} \end{bmatrix}^{-1} \begin{bmatrix} \mathbf{V}_{f,n} - \mathbf{V}_{r,n}^{k} \\ \boldsymbol{\theta}_{f,n} - \boldsymbol{\theta}_{r,n}^{k} \end{bmatrix} \tag{4.18}$$

where $\mathbf{V}_{f,n}$ and $\boldsymbol{\theta}_{f,n}$ are the voltage magnitude and phase angle vectors at the boundary buses in the full system sorted in the same order as in $\mathbf{P}_{ANN,n}^{k}$ and $\mathbf{Q}_{ANN,n}^{k}$. At the k^{th} iteration, the same voltage vectors in the reduced system are denoted as $\mathbf{V}_{r,n}^{k}$ and $\boldsymbol{\theta}_{r,n}^{k}$, respectively. In (4.18), $\partial\mathbf{V}_{r,n}/\partial\mathbf{P}_{ANN,n}$, $\partial\mathbf{V}_{r,n}/\partial\mathbf{Q}_{ANN,n}$, $\partial\boldsymbol{\theta}_{r,n}/\partial\mathbf{P}_{ANN,n}$, and $\partial\boldsymbol{\theta}_{r,n}/\partial\mathbf{Q}_{ANN,n}$ are the sensitivities of $\mathbf{V}_{r,n}$ and $\boldsymbol{\theta}_{r,n}$ calculated at $\mathbf{P}_{ANN,n} = \mathbf{P}_{ANN,n}^{k}$ and $\mathbf{Q}_{ANN,n} = \mathbf{Q}_{ANN,n}^{k}$. Assume that bus i and bus j are two arbitrary buses in B, then $\partial V_{ri,n}/\partial P_{ANNj,n}$ and $\partial \theta_{ri,n}/\partial P_{ANNj,n}$ can be obtained by solving (4.12) in which $P_{ANNj,n}$ is treated as a system parameter. Let $\mathbf{x}'_n = \partial\mathbf{x}/\partial P_{ANNj,n}$ and $\mathbf{y}'_n = \partial\mathbf{y}/\partial P_{ANNj,n}$ computed at the time instant n, (4.12) can be re-written as:

$$\begin{bmatrix} \mathbf{I} - \dfrac{\Delta t}{2}\mathbf{f}_{\mathbf{x},n} & -\dfrac{\Delta t}{2}\mathbf{f}_{\mathbf{y},n} \\ \mathbf{g}_{\mathbf{x},n} & \mathbf{g}_{\mathbf{y},n} \end{bmatrix} \begin{bmatrix} \mathbf{x}'_n \\ \mathbf{y}'_n \end{bmatrix} = \begin{bmatrix} \mathbf{x}'_{n-1} + \dfrac{\Delta t}{2}\mathbf{f}'_n + \dfrac{\Delta t}{2}\left(\mathbf{f}_{\mathbf{x},n-1}\mathbf{x}'_{n-1} + \mathbf{f}_{\mathbf{y},n-1}\mathbf{y}'_{n-1} + \mathbf{f}'_{n-1}\right) \\ -\mathbf{g}'_n \end{bmatrix} \tag{4.19}$$

where $\mathbf{f}'_n$ and $\mathbf{g}'_n$ denote $\partial\mathbf{f}/\partial P_{ANNj,n}$ and $\partial\mathbf{g}/\partial P_{ANNj,n}$ computed at the time instant n, respectively.

In (4.19), it is noted that $P_{ANNj,n}$ is defined specifically for the present time instant n, and it does not affect the system dynamics at previous time instants. Therefore at the time instant n-1, $\partial\mathbf{x}/\partial P_{ANNj,n}=\mathbf{0}$, $\partial\mathbf{y}/\partial P_{ANNj,n}=\mathbf{0}$, and $\partial\mathbf{f}/\partial P_{ANNj,n}=\mathbf{0}$. Correspondingly, it can be shown that in (4.19) $\mathbf{x}'_{n-1}=\mathbf{0}$, $\mathbf{y}'_{n-1}=\mathbf{0}$, and $\mathbf{f}'_{n-1}=\mathbf{0}$. Then (4.19) can be simplified as:

$$\begin{bmatrix} \mathbf{I}-\dfrac{\Delta t}{2}\mathbf{f}_{\mathbf{x},n} & -\dfrac{\Delta t}{2}\mathbf{f}_{\mathbf{y},n} \\ \mathbf{g}_{\mathbf{x},n} & \mathbf{g}_{\mathbf{y},n} \end{bmatrix} \begin{bmatrix} \mathbf{x}'_n \\ \mathbf{y}'_n \end{bmatrix} = \begin{bmatrix} \dfrac{\Delta t}{2}\mathbf{f}'_n \\ -\mathbf{g}'_n \end{bmatrix} \tag{4.20}$$

To solve for $\mathbf{x}'_n$ and $\mathbf{y}'_n$ in (4.20), $\mathbf{f}'_n$ and $\mathbf{g}'_n$ need to be defined properly.

- $\mathbf{f}'_n$ are the derivatives of $\mathbf{f}$ with respect to $P_{ANNj,n}$ at the time instant n. Because $P_{ANNj,n}$ is independent of any dynamic component that is represented by $\mathbf{f}$ and is only modeled as an additional power injection at bus j, it can be proven that $\mathbf{f}'_n=\mathbf{0}$.
- $\mathbf{g}'_n$ are the derivatives of $\mathbf{g}$ with respect to $P_{ANNj,n}$ at the time instant n. At bus j, the following active power balance equation holds:

$$g_{Pj}=P_{j,n}+P_{ANNj,n}-\sum_{k=1}^{n_t}V_{j,n}V_{k,n}\left(G_{jk}\cos\theta_{jk,n}+B_{jk}\sin\theta_{jk,n}\right)=0 \tag{4.21}$$

  where $P_{j,n}$ is the existing power injection at bus j, $V_{j,n}\angle\theta_{j,n}$ and $V_{k,n}\angle\theta_{k,n}$ are the voltages at bus j and bus k, respectively. $G_{jk}+jB_{jk}$ are (j,k) element of the system admittance matrix, and n_t is the total number of buses in the system. It can be proven that $\mathbf{g}'_n$ is a column vector with 1 at the entry corresponding to g_{pj} and zeros elsewhere.

With $\mathbf{f}'_n$ and $\mathbf{g}'_n$ known and using the partial derivative matrices computed in (4.5) - (4.8), (4.20) can be re-written in the following form:

$$\begin{bmatrix} \mathbf{x}'_n \\ \mathbf{y}'_n \end{bmatrix} = \begin{bmatrix} \mathbf{I} - \frac{\Delta t}{2}\mathbf{f}_{\mathbf{x},n} & -\frac{\Delta t}{2}\mathbf{f}_{\mathbf{y},n} \\ \mathbf{g}_{\mathbf{x},n} & \mathbf{g}_{\mathbf{y},n} \end{bmatrix}^{-1} \begin{bmatrix} \mathbf{0} \\ -\mathbf{g}'_n \end{bmatrix} \tag{4.22}$$

It is noted in (4.22) that only the elements in $\mathbf{y}'_n$ that correspond to $\partial V_{i,n}/\partial P_{ANNj,n}$ and $\partial \theta_{i,n}/\partial P_{ANNj,n}$ need to be determined. The sensitivities of the boundary bus voltages with respect to the reactive power injections of the ANN-based equivalent, namely $\partial V_i/\partial Q_{ANNj,n}$ and $\partial \theta_i/\partial \mathrm{Q}_{ANNj,n}$, can also be obtained in a similar manner. The only difference is that $\mathbf{g}'_n$ in (4.22) now becomes a column vector with 1 at the entry corresponding to the reactive power balance equation of bus *j* and zeros elsewhere. The iterative procedure terminates when the voltage difference in (4.18) is smaller than a specified tolerance.

To minimize the number of modifications to the existing transient simulation software packages, the proposed method is implemented in accordance with the flowchart, as shown in Fig. 4.3.

The proposed method has been successfully incorporated into the dynamic simulation software package named the Power System Analysis Toolbox (PSAT) [34] developed in MATLAB environment. Prior to running this routine, the voltage responses at the boundary buses in the full system representation are simulated for the same system disturbance of interest. The obtained responses are then used as the reference in determining the proper power injections of the ANN-based equivalent.

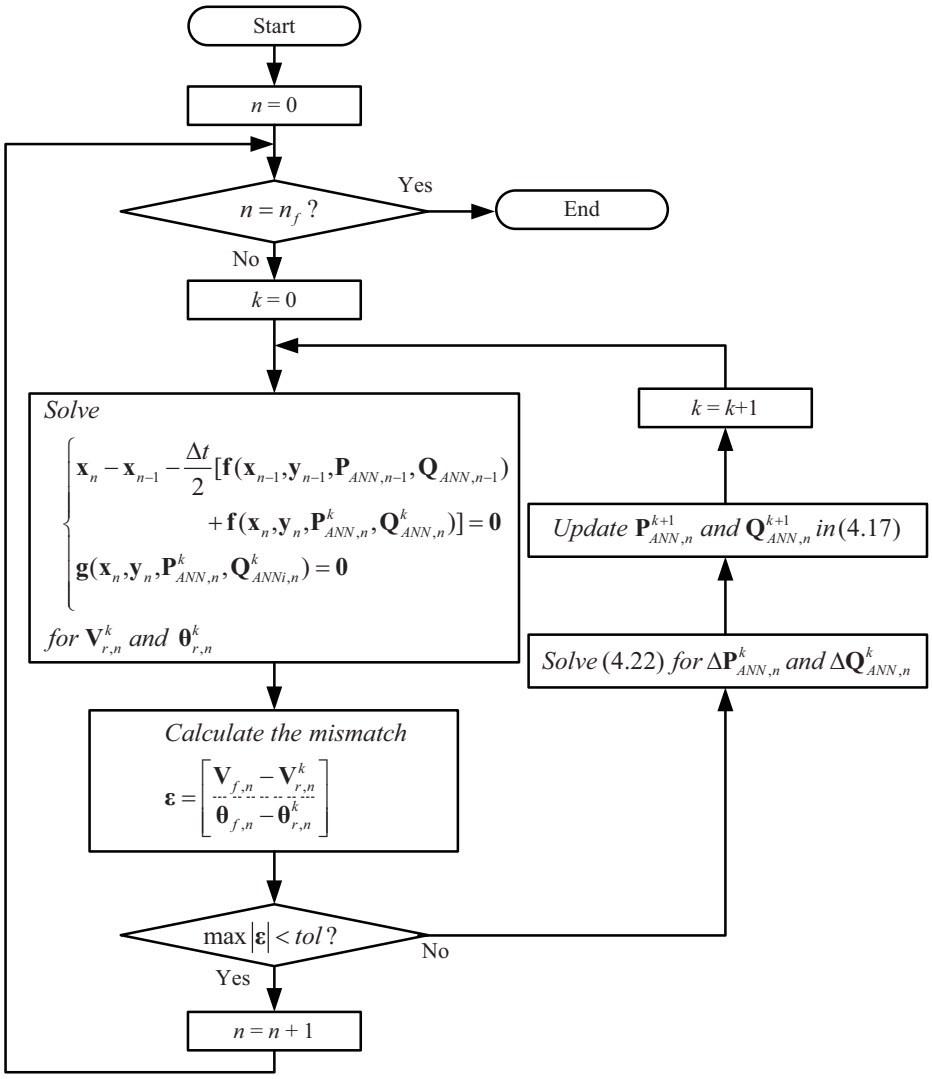

Fig. 4.3 Flowchart for building an ANN training set.

After running the proposed routine, the following training set for a given disturbance can be formed:

$$Training\ Set = \left(\begin{bmatrix} \mathbf{V}_{r,n} \\ \boldsymbol{\theta}_{r,n} \end{bmatrix}, \begin{bmatrix} \mathbf{P}_{ANN,n} \\ \mathbf{Q}_{ANN,n} \end{bmatrix} \right),\ n = 0,...,n_f \tag{4.23}$$

where n_f is the time instant until which the responses are compared.

In order to provide sufficient training samples for the ANN-based equivalent, different contingencies need to be investigated using the identical

approach as shown in Fig. 4.3. It can be seen that the proposed algorithm is a type of boundary matching technique specifically for time-domain simulation. During the simulation duration, the trajectory sensitivity is computed without extensively increasing the computational burden. In addition, the trajectory sensitivity with respect to a specific system parameter is independent of the other parameters. Therefore, the computational efficiency can be further improved with the use of a parallel or cluster computation technique. For instance, the trajectory sensitivities of the boundary voltages with respect to the active and reactive power injections in (4.18) can be computed simultaneously on different computing units in a cluster. Another advantage of the proposed method is that real-time data collected by the PMUs installed at the boundary buses can be directly used as the reference in forming the training set. In this way, it allows the ANN-based equivalent to capture the discrepancy between the planning models that are used for building the conventionally reduced system and the exact system models under realistic operating condition, leading to improved models for on-line DSA.

4.3 ANN-based Equivalent Formulation

Given the training samples formed in the previous section, an appropriate neural network, simulating the input-and-output mapping stored in the training set, needs to be determined. This section starts with a brief introduction to the ANN theory.

4.3.1 Introduction to ANN

The development of ANNs originated as a result of a goal to approximate the functionality of human brains in solving various problems that cannot be

handled with digital computing techniques. The pioneering work on ANN was carried out by McCulloch and Pitts in the 1940s, and they showed that the neuron can be modeled as a simple threshold device to perform logic function. In the 1960s, the models, such as perceptron, adaline, and learning matrix, were introduced as efforts to realize the concept of neural network. Due to extensive studies involved, neural networks have become a popular and efficient technique in a wide range of applications. The basic elements of a neural network are introduced in the following sections.

4.3.1.1 Neuron

A neuron is the fundamental unit of the neural network. A standard model of a neuron is shown in Fig. 4.4.

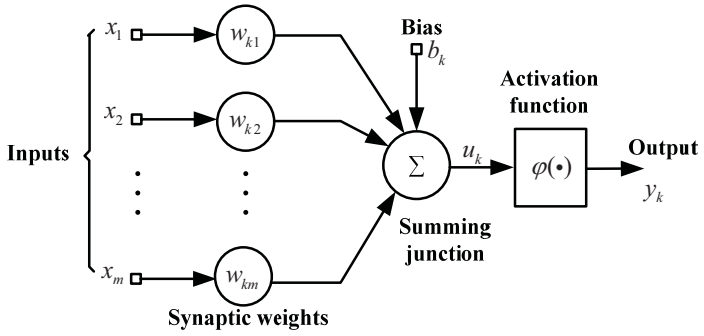

Fig. 4.4 Typical model of a neuron.

It is seen from Fig. 4.4 that a neuron is a nonlinear and parameterized function including three basic elements:

- Connecting links: the connecting links are characterized by weights. For the weight w_{kj}, the first subscript refers to the neuron of interest and the second subscript denotes the input associated with this weight.
- Summing junction: this junction sums the input signals weighted by the

respective connection weights of the neuron. For the neuron shown in Fig. 4.4, it can be described by:

$$u_k = \sum_{j=1}^{p} w_{kj} x_j + b_k \tag{4.24}$$

where x_1,x_2, …, x_p are input signals, w_{k1}, w_{k2}, …, w_{kp} are the input weights, b_k is the bias, and u_k is the summing output.

- Activation function: the activation function defines the output of a neuron in terms of the activity level of its inputs. Four basic types of activation functions are summarized in Fig. 4.5.

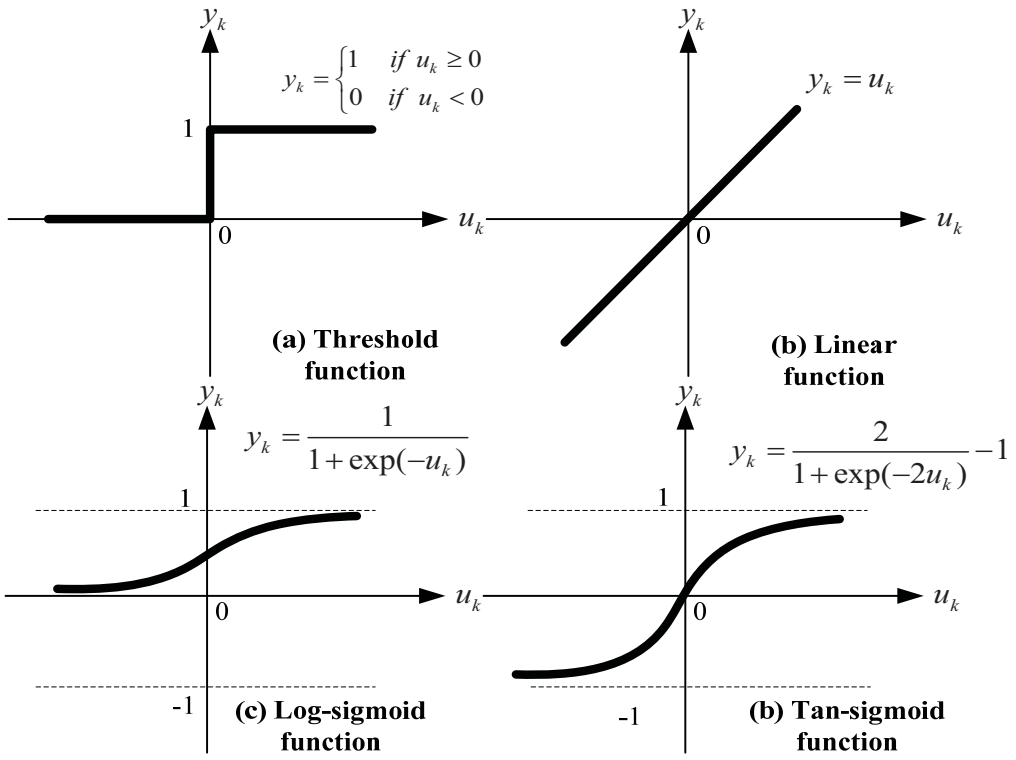

Fig. 4.5 Typical activation functions.

Among these activation functions, the linear and sigmoid functions are widely applied because that they are differentiable and continuous. The first

characteristic makes it possible to derive a gradient search learning algorithm for the network with multiple layers, and the second feature makes the network suitable for the applications requiring a continuous-valued output instead of the binary output. As shown in Fig. 4.5, the amplitude ranges of the output of a neuron are normalized in the interval of [0,1] for the log-sigmoid function and [-1,1] for the tan-sigmoid function.

4.3.1.2 Network Structure

When neurons are structured into a neural network, different layouts yield diverse network behaviors. According to the architecture, neural networks can be divided into two categories:

(a) Feed-forward Network

It produces only one set of outputs rather than a sequence of values from the inputs. In other words, it is memory-less in the sense that its response to the inputs is independent of the previous network states. This category of neural network includes:

- **Multilayer Perceptron-based Network (MLP)**

In Fig. 4.6, the layer manipulating the input signals is called input layer, the layer performing the intermediate computations is called hidden layer, and the layer connected to the outputs is called output layer. For the MLP network in Fig. 4.6, the input layer, hidden layer, and output layer contain n neurons, h neurons, and o neurons, respectively. It is to be noted that the feed-forward network is static in nature. Therefore the outputs can be determined uniquely with the presence of the inputs at a given time instant.

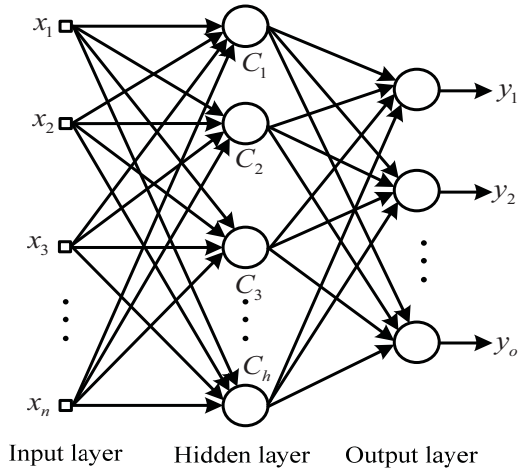

Fig. 4.6 Typical MLP network structure.

- **Radial Basis Function-based Network (RBF)**

Instead of assigning the weights to the connections as in MLP networks, the adjustable parameters in a RFB network are assigned to its nonlinear activation functions. A typical RBF network is shown in Fig. 4.7.

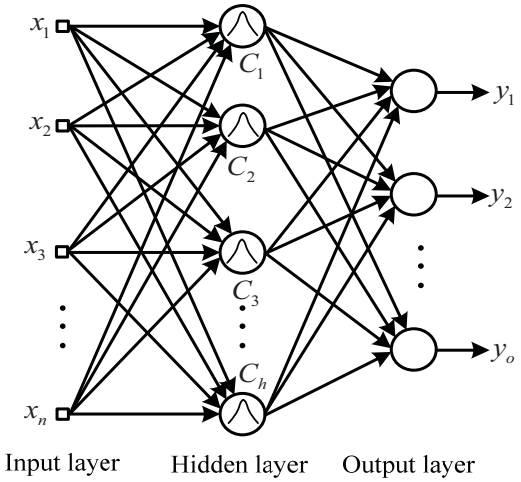

Fig. 4.7 Typical RBF network structure.

As shown in Fig. 4.7, the activation function at the hidden layer is the Gaussian distribution function. For the neuron *i* at the hidden layer, this function is given by:

$$C_i(\mathbf{x}) = \exp\left[-\frac{\sum_{j=1}^{n} \left(x_j - m_i \right)^2}{2\sigma_i^2} \right] \tag{4.25}$$

where $\mathbf{x} = [x_1, x_2, \ldots, x_n]^T$ is the input vector, m_i and σ_i^2 are the mean value and variance of the Gaussian basis function respectively. In addition to the weights from the hidden layer to the output layer, the Gaussian distribution parameters in (4.25) need to be optimized. The study in [35] shows that the RBF networks with Gaussian basis function have been shown to be universal function approximators.

(b) Recurrent Neural Network

The recurrent neural network is different from a feedforward neural network in the sense that it has at least one feedback loop in its structure. It can either be the feedback of the outputs or the feedback of the states at the hidden layer. The presence of feedback loops has a profound impact on the learning capacity and performance of this type of neural network. In fact, the recurrent network becomes a dynamic network, and its outputs depend not only on the present inputs but also the feedbacks derived from the previous time instants. Two types of recurrent neural networks are commonly found in the literature.

- **Locally Recurrent Neural Network (LRNN)**

The basic idea of LRNN is to introduce the system states at the hidden layer to the input layer. A typical LRNN with unit time delay (UTD) function is displayed in Fig. 4.8.

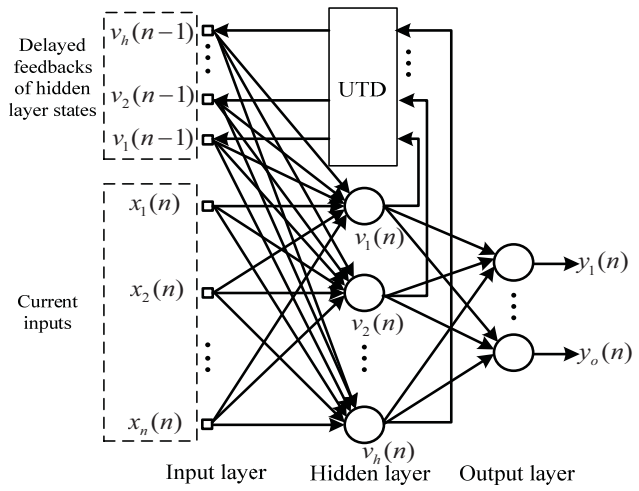

Fig. 4.8 Typical LRNN structure.

As shown in Fig. 4.8, the outputs of the neurons at the hidden layer are fed back to the network inputs through a UTD. Therefore, the order of the model is equal to the number of hidden neurons. The outputs at a specific time instant are nonlinear functions of the external inputs at the present time instant and of the outputs of hidden neurons at the previous time instant. This type of network has been successfully implemented in the studies in [36]-[38].

- **Fully Recurrent Neural Network (FRNN)**

Compared to LRNN, the feedback in a FRNN is achieved by connecting the network outputs to its inputs. A simplified FRNN with a UTD is shown in Fig. 4.9. As can be seen from Fig. 4.9, the order of the mode is determined by the number of output neurons. At a specific time instant, the outputs are the nonlinear functions of the external inputs at the present instant and the network outputs at previous time instant. Because of the inherent dynamic characteristics of FRNN, it has been successfully implemented in different studies [31],[39],[40].

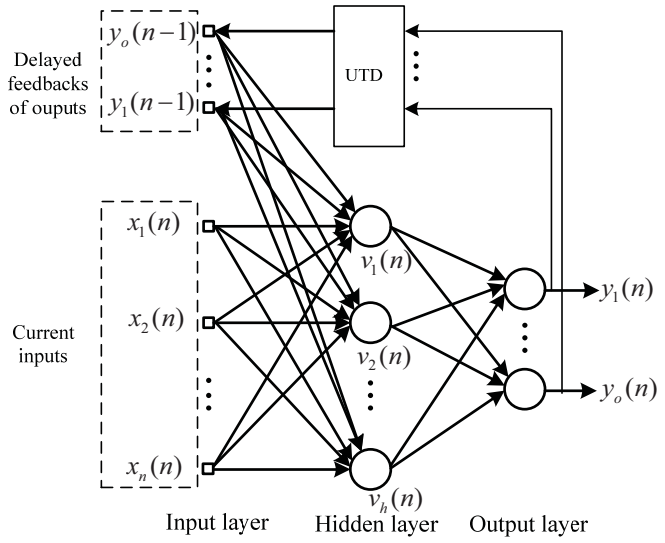

Fig. 4.9 Typical FRNN structure.

4.3.2 Neural Network Structure

As a dynamic system, the present outputs of the ANN-based equivalent depend not only on the present inputs but also the inputs and outputs at previous time instants. To accommodate this characteristic, a FRNN [41] is used as the network model for the ANN-based equivalent. As shown in Fig. 4.10, compared to a typical MLP, the outputs of the FRNN are fed back into the MLP as additional inputs. At the input side, both the bus voltages and the power injection predictions are fed into the network through the tapped-delay-line-memories with *l* and *m* delayed units, respectively. At the time instant *n*, the ANN-based equivalent can be represented by a nonlinear function vector defined as:

$$\mathbf{S}_{ANN,n} = \mathbf{h}(\mathbf{V}_{ANN,n}, \mathbf{V}_{ANN,n-1}, ..., \mathbf{V}_{ANN,n-l}, \mathbf{S}_{ANN,n-1}, ..., \mathbf{S}_{ANN,n-m}) \qquad (4.26)$$

where $\mathbf{V}_{ANN,n-l}$ is the voltage vector at the time instant *n-l*, $\mathbf{S}_{ANN,n-m} = [\mathbf{P}_{ANN,n-m}{}^{T}\ \mathbf{Q}_{ANN,n-m}{}^{T}]^{T}$ is the power injection vector at the time instant *n-m*, and **h** is the vector of nonlinear mapping functions determined by the specific MLP used.

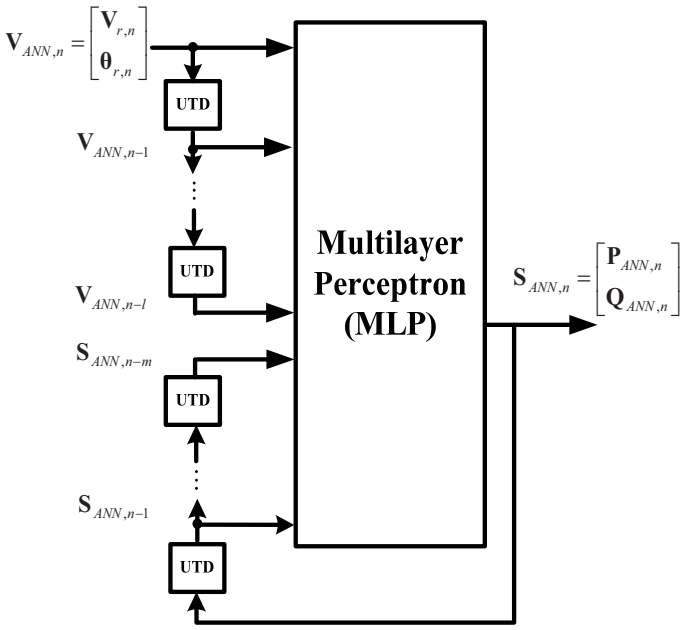

Fig. 4.10 ANN-based equivalent using FRNN.

For the FRNN to achieve a desirable capability of capturing the input-and-output mapping stored in the training set and at the same time to limit the number of neuron parameters to be optimized, the MLP with three layers of neurons is used in the proposed FRNN, as shown in Fig. 4.11.

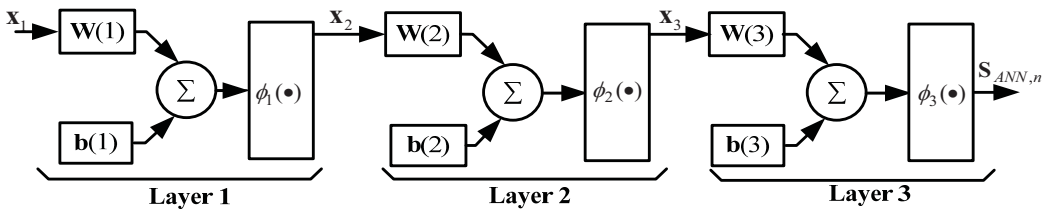

Fig. 4.11 Structure of MLP in ANN-based equivalent.

In Fig. 4.11, the input vector is $\mathbf{x}_1=[\mathbf{V}_{ANN,n}{}^{T},\mathbf{V}_{ANN,n-1}{}^{T},\ldots,\mathbf{V}_{ANN,n-l}{}^{T},\mathbf{S}_{ANN,n-1}{}^{T},\ldots,\mathbf{S}_{ANN,n-m}{}^{T}]^{T}$. $\mathbf{x}_2$ and $\mathbf{x}_3$ are the internal state vectors. $\mathbf{W}(1)$, $\mathbf{W}(2)$, and $\mathbf{W}(3)$ are the weighting matrices. $\mathbf{b}(1)$, $\mathbf{b}(2)$, and $\mathbf{b}(3)$ are the bias vectors. ϕ_1, ϕ_2, and ϕ_3

are the activation functions. The subscript 1, 2, and 3 denote layers 1, 2, and 3 in the neural network, respectively. Assume that $n_1 \times 1$, $n_2 \times 1$, $n_3 \times 1$, and $n_4 \times 1$ are the dimensions of $\mathbf{x}_1$, $\mathbf{x}_2$, $\mathbf{x}_3$, and $\mathbf{S}_{ANN,n}$, respectively, then for layer 1 it can be shown that:

$$x_{2k} = \phi_1\left(\sum_{j=1}^{n_1} w_{kj}(1)x_{1j} + b_k(1)\right),\ k = 1,\ldots,n_2 \tag{4.27}$$

where x_{1j} is the j^{th} element of $\mathbf{x}_1$, $w_{kj}(1)$ is the $(k,j)^{\text{th}}$ element of $\mathbf{W}(1)$, $b_k(1)$ is the k^{th} element of $\mathbf{b}(1)$, and x_{2k} is the k^{th} element of $\mathbf{x}_2$. Similarly, the following equations hold for layers 2 and 3:

$$x_{3k} = \phi_2\left(\sum_{j=1}^{n_2} w_{kj}(2)x_{2j} + b_k(2)\right),\ k = 1,\ldots,n_3 \tag{4.28}$$

where $\mathbf{x}_{3k}$ is the k^{th} element of $\mathbf{x}_3$, $w_{kj}(2)$ is the $(k,j)^{\text{th}}$ element of $\mathbf{W}(2)$, $b_k(2)$ is the k^{th} element of $\mathbf{b}(2)$, and x_{2j} is the j^{th} element of $\mathbf{x}_2$.

$$S_{ANN,nk} = \phi_3\left(\sum_{j=1}^{n_3} w_{kj}(3)x_{3j} + b_k(3)\right),\ k = 1,\ldots,n_4 \tag{4.29}$$

where $S_{ANN,nk}$ is the k^{th} element of $\mathbf{S}_{ANN,n}$, $w_{kj}(3)$ is the $(k,j)^{\text{th}}$ element of $\mathbf{W}(3)$, $b_k(3)$ is the k^{th} element of $\mathbf{b}(3)$, and x_{3j} is the j^{th} element of $\mathbf{x}_3$. Then the characteristic equation $\mathbf{h}$ in (4.26) can be determined uniquely as the combination of (4.27) - (4.29).

4.4 Levengerb-Marquardt (LM) Training Method

To train the FRNN as shown in Fig. 4.10, a variety of training algorithms, such as evolutionary method [42], Kalman filter-based method [43], and particle swarm optimization-based method [44], is proposed in the literature. However, these training methods still need further improvements in order to achieve a

satisfactory computational efficiency. It is noted that the exact outputs in Fig. 4.10 are stored in the training set during the training process. Therefore the FRNN can convert to a normal MLP, in which the exact outputs instead of the feedbacks of the outputs are used for training purpose. As a result, an equivalent MLP in the training process can be formed, as shown in Fig. 4.12.

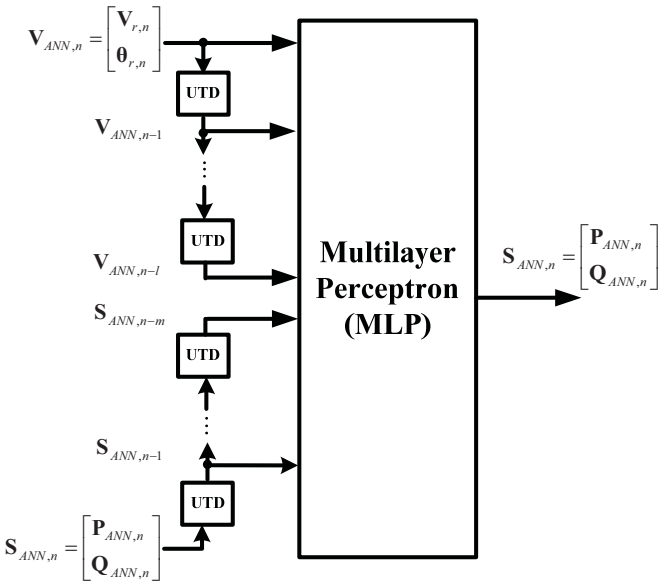

Fig. 4.12 Equivalent network for training.

In Fig. 4.12, the equivalent MLP for the training purpose is simply a feed-forward network, and more efficient static backpropagation algorithms can be applied. A backpropagation algorithm is a specific type of error-correction learning technique with the implementation of the gradient descent in the weight space [41]. The basic idea is to efficiently compute partial derivatives of the total cost function realized by the network with respect to all the elements of the adjustable weight matrix **w** (e.g. neuron weights and biases) for a given value of input vector **x**. At the k^{th} iteration, the total cost function is defined as:

$$E^k = \frac{1}{2}\left(\mathbf{e}^k\right)^T \left(\mathbf{e}^k\right) \tag{4.30}$$

where $\mathbf{e}^k$ is the error vector between the reference and predicted outputs calculated at $\mathbf{w}^k$. Then the gradient vector of E^k can be defined as:

$$\nabla E^k = \left(\frac{\partial \mathbf{e}^k}{\partial \mathbf{w}^k}\right)^T \mathbf{e}^k \tag{4.31}$$

Let $\mathbf{J}^k = \partial \mathbf{e}^k / \partial \mathbf{w}^k$, then the following adjustment to the weight vector $\mathbf{w}^k$ is made in the direction opposite to the gradient vector in (4.31) that reduces the cost function at the k+1th iteration:

$$\mathbf{w}^{k+1} = \mathbf{w}^k - \eta \nabla E^k = \mathbf{w}^k - \eta \left(\mathbf{J}^k\right)^T \mathbf{e}^k \tag{4.32}$$

where η is the learning rate.

The training algorithm in (4.32) is often too slow for practical problems. To improve the training efficiency, the Levenberg-Marquardt (LM) method [45] can be applied. In this method, the second-order training speed can be achieved without computing the exact Hessian matrix. At the k^{th} iteration,

$$\mathbf{w}^{k+1} = \mathbf{w}^k - [\mathbf{H}^k + \mu_i \mathbf{I}]^{-1} \left[(\mathbf{J}^k)^T \mathbf{e}^k \right] \tag{4.33}$$

where $\mathbf{H}^k = (\mathbf{J}^k)^T \mathbf{J}^k$ is the approximation of the Hessian matrix of the total cost function, and μ_i is positive iteration step.

For small values of μ_i in (4.33), the LM algorithm is similar in performance to the Newton method; while for large value of μ_i, the LM algorithm is equivalent in performance to the simple gradient descent with step $1/\mu_i$. During the iteration process, μ_i is decreased after each successful step (reduction in the total cost function) and is increased only when a tentative step would increase the

total cost function. In this way, the total cost function can always decrease in magnitude during the iterative process. The study in [45] shows that for function approximation problems involving the network with up to a few hundred weights, the LM algorithm has the fastest convergence speed. Therefore, the LM algorithm is used as the training method for the proposed ANN-based equivalent.

4.5 Hybrid Reduced System Simulation

With the inclusion of the ANN-based equivalent, the reduced system now becomes a hybrid system in the sense that it contains both the continuous system (described by a set of DAEs) and the discrete system (ANN-based equivalent). The ANN-based equivalent can be regarded as a set of adjustable *P-Q* sources using the terminal voltages as inputs at the fixed time instants. As shown in (4.26), the ANN-based equivalent is represented by a set of nonlinear equations as shown below:

$$\mathbf{S}_{ANN,n} = \mathbf{h}(\mathbf{V}_{ANN,n}, \mathbf{V}_{ANN,n-1}, ..., \mathbf{V}_{ANN,n-l}, \mathbf{S}_{ANN,n-1}, ..., \mathbf{S}_{ANN,n-m}) \tag{4.34}$$

It is to be noted that at the time instant n, the inputs at the previous time instants, namely $[\mathbf{V}_{ANN,n\text{-}1}^{T},\ldots,\mathbf{V}_{ANN,n\text{-}l}^{T}]^{T}$ and $[\mathbf{S}_{ANN,n\text{-}1}^{T},\ldots,\mathbf{S}_{ANN,n\text{-}m}^{T}]^{T}$, have already been calculated and therefore can be treated as constants. Then (4.34) simply becomes a nonlinear mapping from $\mathbf{S}_{ANN,n}$ to $\mathbf{V}_{ANN,n}$ defined by:

$$\mathbf{S}_{ANN,n} = \mathbf{h}'(\mathbf{V}_{ANN,n}) \tag{4.35}$$

where $\mathbf{h}'$ is the simplified nonlinear function vector with the previous inputs in (4.34) fixed.

When combing the DAEs of the conventionally reduced system and the characteristic equation in (4.35), the hybrid system at the time instant n can be represented by:

$$\begin{cases} \dot{\mathbf{x}} = \mathbf{f}(\mathbf{x},\mathbf{y},\mathbf{S}_{ANN,n}) \\ \mathbf{0} = \mathbf{g}(\mathbf{x},\mathbf{y},\mathbf{S}_{ANN,n}) \\ \mathbf{0} = \mathbf{S}_{ANN,n} - \mathbf{h}'(\mathbf{V}_{ANN,n}) \end{cases} \tag{4.36}$$

where $\mathbf{V}_{ANN,n}$ is the vector of the voltages at the connection buses of the ANN-based equivalent at the time instant n that have already been represented in $\mathbf{y}$.

As can be seen in (4.36), the ANN-based equivalent interacts with the conventionally reduced system through $\mathbf{S}_{ANN,n}$ at all the boundary buses. To numerically simulate the hybrid system, two methods have been proposed.

4.5.1 Interactive Integration Method

The basic idea of the interactive integration method is to fix the power injections of the ANN-based equivalent when solving for the remaining system state and algebraic variables. The converged variables are then fed into the neural network in order to update the power injections of the ANN-based equivalent. The iterative process terminates when the difference in the power injections of the ANN-based equivalent obtained from two adjacent iterations is smaller than a specified tolerance. As shown in Fig. 4.13, a detailed procedure is depicted in the flowchart.

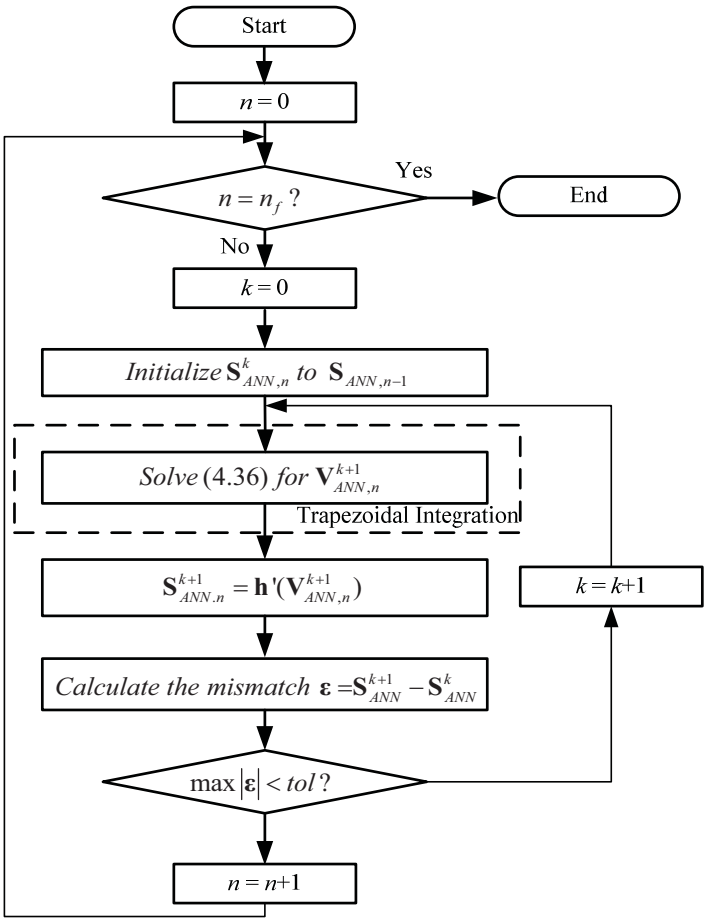

Fig. 4.13 Flowchart of interactive integration method.

As emphasized in Fig. 4.13, the proposed method can be easily realized in any software package for transient stability analysis. Without changing the procedure to build the system Jacobian matrix, only an external loop is added to update the power injections of ANN-based equivalent. However, it is noted that the proposed method could takes a long time to converge because the bus voltages and power injections of the ANN-based equivalent are updated asynchronously.

4.5.2 Simultaneous Integration Method

In comparison to the interactive integration method, the simultaneous integration method has the advantages of fast convergence speed because the

impacts that the ANN-based equivalent has on the power balance equations **g** and system Jacobian matrix $\mathbf{g}_\mathbf{y}$ are modeled. At the time instant *n*, for example, the new power balance equations at bus $i \in B$ are given by:

$$\begin{cases} g_{Pi} = P_{i,n} + P_{ANNi,n} - \sum_{k=1}^{n_t} V_{i,n} V_{k,n} \left(G_{ik} \cos\theta_{ik,n} + B_{ik} \sin\theta_{ik,n} \right) \\ g_{Qi} = Q_{i,n} + Q_{ANNi,n} - \sum_{k=1}^{n_t} V_{i,n} V_{k,n} \left(G_{ik} \sin\theta_{ik,n} - B_{ik} \cos\theta_{ik,n} \right) \end{cases} \tag{4.37}$$

It is noted that in (4.37), $P_{ANNi,n}$ and $Q_{ANNi,n}$ are the functions of $V_{j,n}$ and $\theta_{j,n}$ ($j \in B$) that are described by the input-and-output mapping in the proposed ANN-based equivalent. Then the corresponding partial derivatives, such as $\partial P_{ANNi,n}/\partial V_{j,n}$, $\partial P_{ANNi,n}/\partial \theta_{j,n}$, $\partial Q_{ANNi,n}/\partial V_{j,n}$, and $\partial Q_{ANNi,n}/\partial \theta_{j,n}$, need to be formed. For instance, $\partial P_{ANNi,n}/\partial V_{j,n}$ is given by:

$$\frac{\partial P_{ANNi,n}}{\partial V_{j,n}} = \left(\frac{\partial P_{ANNi,n}}{\partial \mathbf{x}_3} \right) \left(\frac{\partial \mathbf{x}_3}{\partial \mathbf{x}_2} \right) \left(\frac{\partial \mathbf{x}_2}{\partial \mathbf{x}_1} \right) \left(\frac{\partial \mathbf{x}_1}{\partial V_{j,n}} \right) \tag{4.38}$$

Assume ϕ_1 and ϕ_2 are tan-sigmoid activation functions and ϕ_3 is a liner activation function, then the elements of each derivative matrix in (4.38) are given by:

$$\partial P_{ANNi,n} / \partial x_{3m} = w_{km}(3) \tag{4.39}$$

where *k* is the index of $P_{ANNi,n}$ in $\mathbf{S}_{ANN,n}$.

$$\partial x_{3m} / \partial x_{2p} = \left[1 - \left(\sum_{j=1}^{n_2} w_{kj}(2) x_{2j} + b_k(2) \right)^2 \right] w_{mp}(2) \tag{4.40}$$

where $m = 1,\ldots, n_3$, and $p = 1,\ldots, n_2$.

$$\partial x_{2m} / \partial x_{1p} = \left[1 - \left(\sum_{j=1}^{n_1} w_{kj}(1) x_{2j} + b_k(1) \right)^2 \right] w_{mp}(1) \tag{4.41}$$

where $m = 1,\ldots, n_2$, and $p = 1,\ldots, n_1$.

$$\partial \mathbf{x}_1 / \partial V_{j,n} = [0,...,1,....,0]^T \tag{4.42}$$

where the element of $\mathbf{x}_1$ at the position associated with $V_{j,n}$ is 1 and zeros elsewhere.

The same procedures as shown in (4.38) - (4.42) are followed to account for the impact of $Q_{ANNi,n}$ but are omitted for the sake of brevity. In correspondence to the power injections of the ANN-based equivalent in (4.37), the partial derivatives in (4.38) are appended to the original derivative matrix $\mathbf{g}_y$ formed in any dynamic simulation software package. The detailed flowchart of the proposed integration method is depicted in Fig. 4.14.

During the iterative process, both the power balance equations and system Jacobian matrix are updated to model the power injections of the ANN-based equivalent, as shown in Fig. 4.14. Therefore it achieves faster convergence than the interactive integration method. The disadvantage of the proposed method is that the partial derivatives in (4.38) need to be calculated constantly at each iteration. However, it is to be noted that in a realistic setting the number of boundary buses connected with the ANN-based equivalent are substantially smaller than the total number of buses in the reduced system. In addition, the appended derivatives can also be readily formed due to the superior derivative characteristics of the activation functions used. Therefore the additional computational effort to simulate the hybrid reduced system is manageable. As a result of the advantages offered by the simultaneous integration method, it is chosen as the default method to integrate the ANN-based equivalent with the conventional coherency-based equivalent.

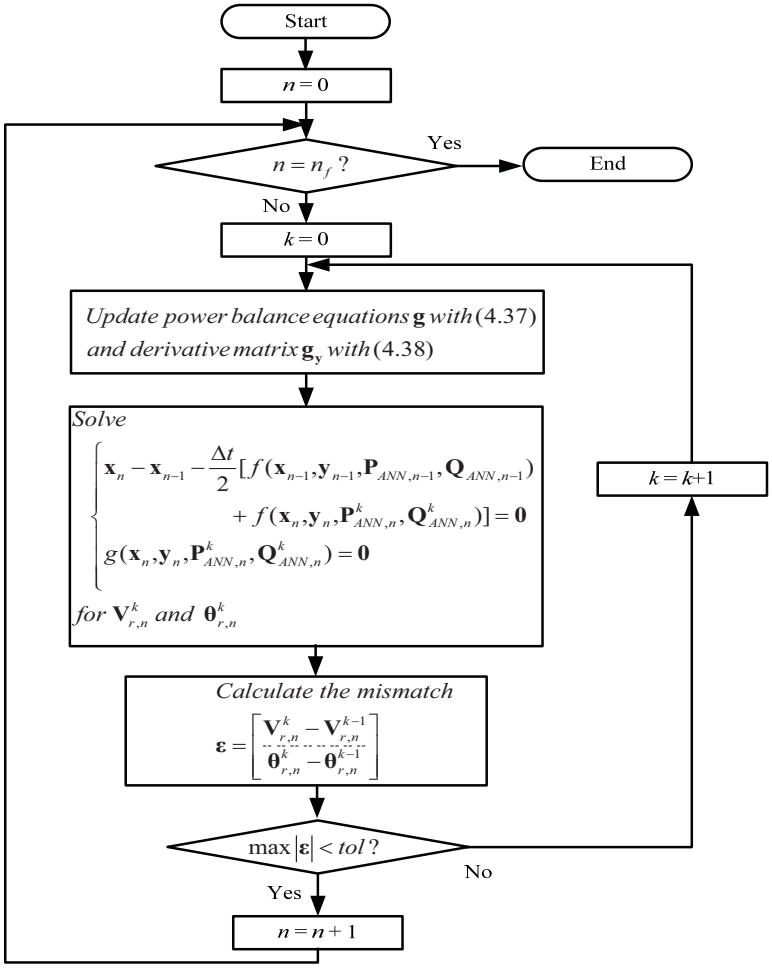

Fig. 4.14 Flowchart of simultaneous integration method.

4.6 Test Case Verification

A portion of the WECC system is tested to validate the proposed hybrid dynamic equivalent method. A schematic diagram of the test system is shown in Fig. 4.15. The test system has a total generation of 56944 MW and 7340 MVAr and a total load demand of 55476 MW and 6447 MVAr. The detailed generator models with exciters, governors, and PSS are used if applicable. In Fig. 4.15, the network at 230 kV and above within the retained area is detailed. The remaining portion is defined as the external area.

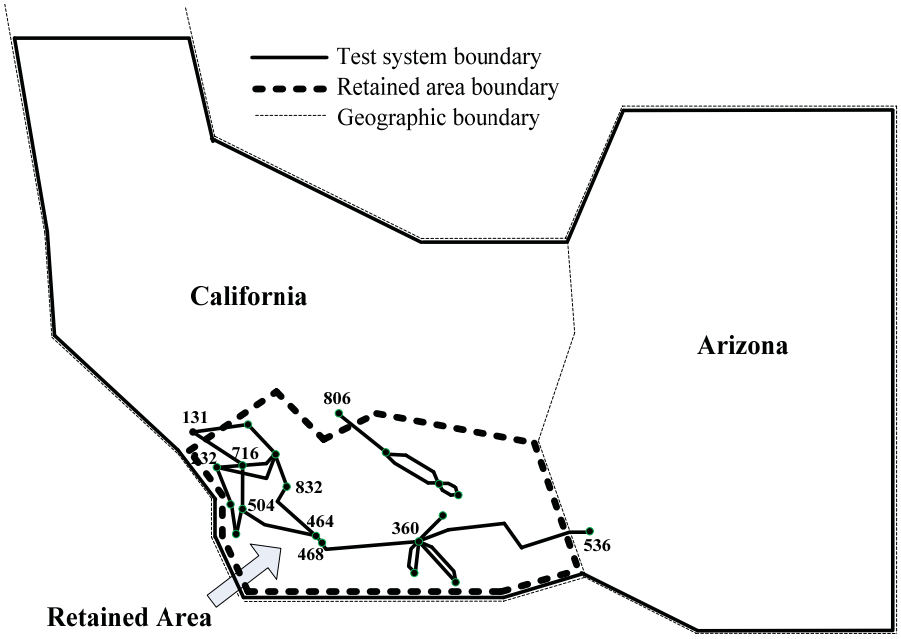

Fig. 4.15 Schematic diagram of the test system [30].

4.6.1 Conventionally Reduced System

After loading the power flow and dynamic data into DYNRED, the coherent generators are identified using the weak-link method [4]. In the external area, a total of 115 groups of coherent generators are identified with 24 of them having only one generator in each group. Then the coherent generators in each group are aggregated and replaced by an appropriate equivalent generator using a classical model representation. In the final step, the network in the external area is reduced using Gaussian elimination, and the loads are appropriately aggregated. As a result, a conventionally reduced system, consisting of both the retained area and the equivalent model of the external area, is formed. The effectiveness of the dynamic equivalent technique in reducing the scale of the system to be simulated is illustrated in Table 4-1.

Table 4-1 Summary of full system and conventionally reduced systems

	Full syst.	Conv. reduced syst.	% of full syst.
Buses	2240	806	36.0%
Branches	3015	1573	52.2%
Loads	913	481	52.7%
Generators	342	145	42.4%

Table 4-1 shows that a significant reduction in the system size can be achieved using the coherency-based dynamic equivalent. Within the entire system, 57.6% of the generators in the full system have been eliminated in the conventionally reduced system. Similar reduction in the total number of buses, branches, and loads can also be found. To validate the equivalencing accuracy of the conventionally reduced system, a three-phase fault is applied on bus 360 at 0.5 s, and it is cleared after 0.1 s by tripping the 500 kV line from bus 360 to bus 468. During the simulation process, the relative rotor angle of generator 15 in the retained area that has the largest RMSE and the voltage magnitude at one of the boundary buses (bus 131) are shown in Fig. 4.16.

It is seen from Fig. 4.16 that the reduced system formed in DYNRED cannot fully capture the dynamic characteristics of the retained area, and the discrepancy becomes significantly large as the simulation evolves. Therefore, the coherency-based equivalent model of the external area needs to be improved.

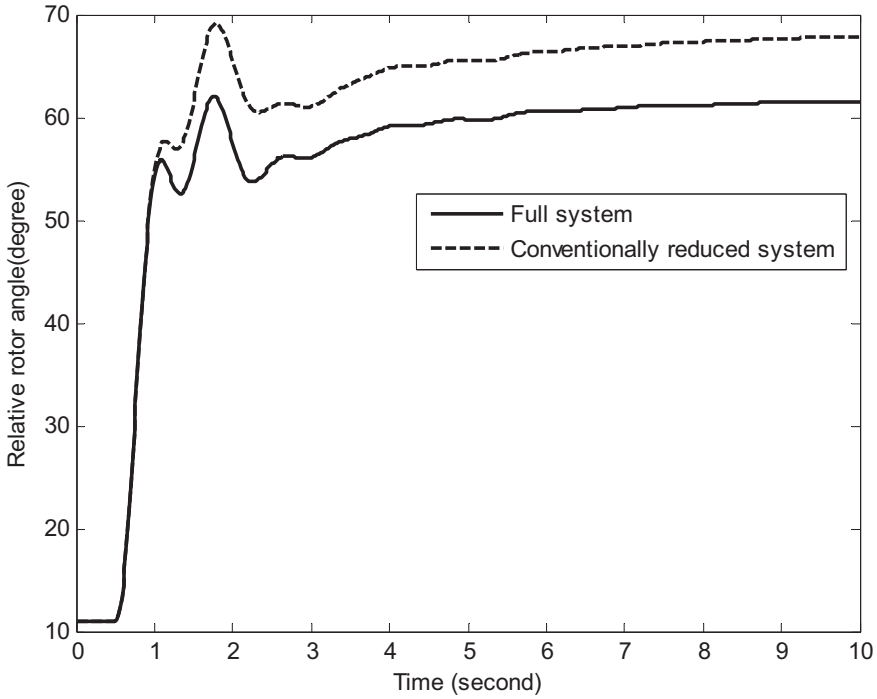

(a) Relative rotor angle response of generator 15

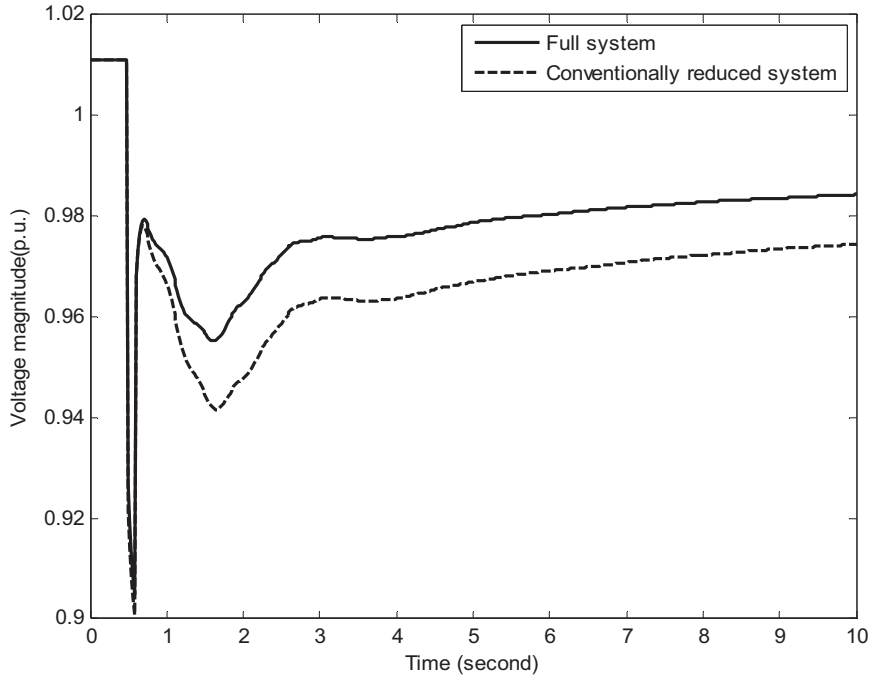

(b) Voltage response at bus 131

Fig. 4.16 Responses in the full system and conventionally reduced system.

4.6.2 Hybrid Reduced System

To account for the observed mismatch between the full system and conventionally reduced system, the ANN-based equivalent is formed. In the test system, all the buses on the original retained area boundary, namely bus 131, 806, and 536, are chosen as the connection buses of the ANN-based equivalent. In forming the samples in the training set, the typical contingencies summarized in Table 4-2 are evaluated. The simulation duration for all cases is 10 s. For the sake of simplicity, only the three-phase faults are considered.

Table 4-2 Summary of trained contingency cases

Case #	Faulted bus	Clearing time (ms)	Line tripped	
			From bus	To bus
1	360	60	360	468
2	360	100	360	468
3	832	100	464	832
4	832	160	464	832
5	716	100	232	716
6	716	160	232	716

For each case in Table 4-2, the trajectory sensitivity-based approach is applied to determine the required power injections of the ANN-based equivalent. The integration time step is fixed at 0.02 s, and a total of 3006 samples are obtained for building the training set. For example, the required power injections of the ANN-based equivalent in Case 2 are shown in Fig. 4.17.

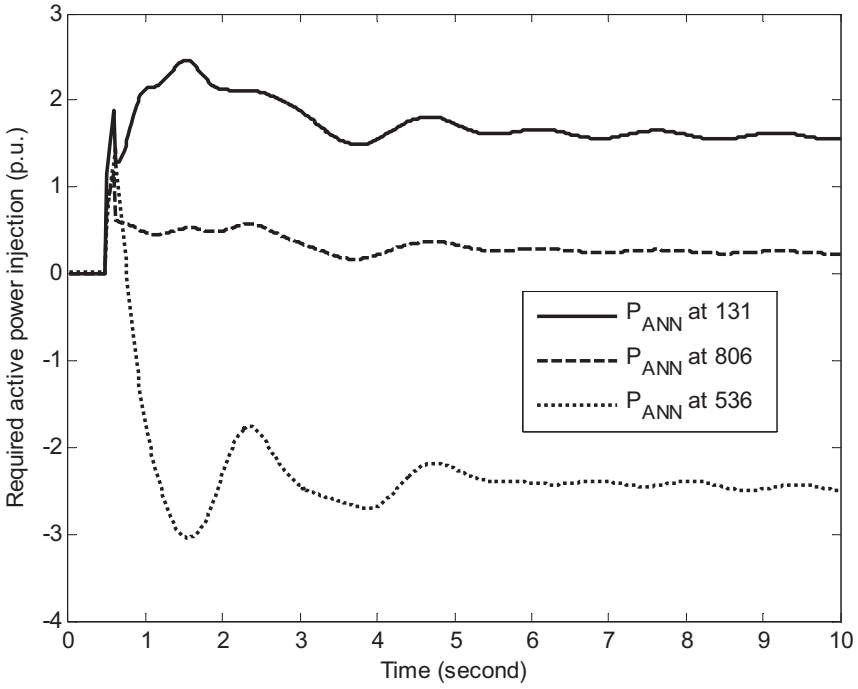

(a) Required active power injections at bus 131, 806, and 536

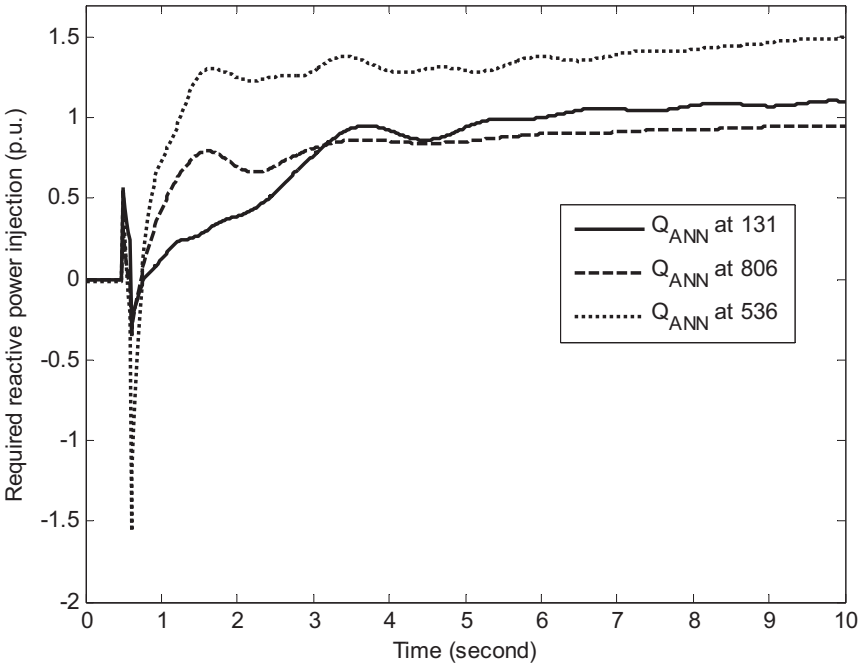

(b) Required reactive power injections at bus 131, 806, and 536

Fig. 4.17 Required power injections of the ANN-based equivalent for Case 2.

For Case 2, the number of iterations required in the sensitivity approach to converge to the required power injections at each time instant is presented in Fig. 4.18.

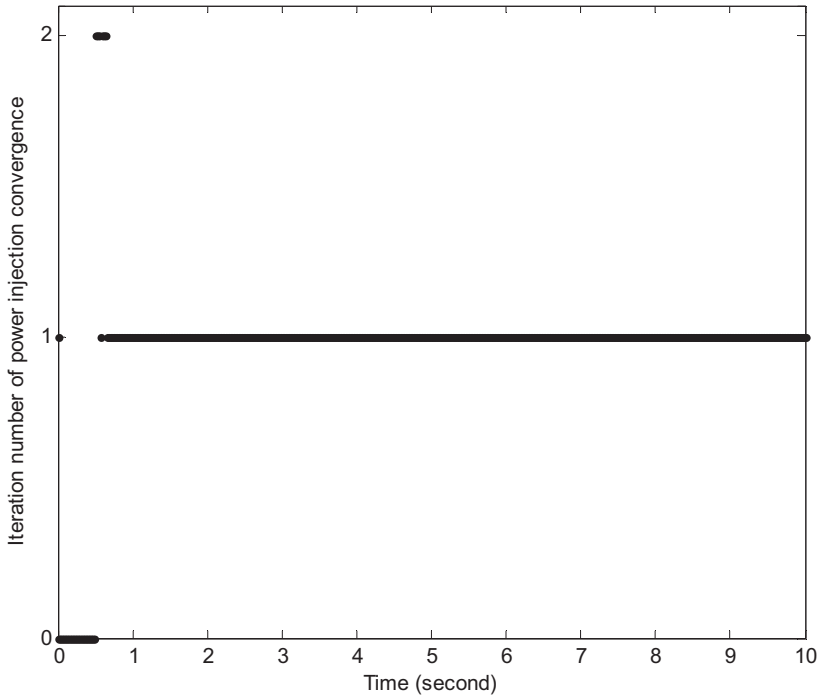

Fig. 4.18 Iteration number of power injection convergence for Case 2.

It is seen from Fig. 4.18 that because the trajectory sensitivity can provide accurate estimate of the system variable deviations, one iteration is needed to match the voltage responses at boundary buses for the majority of the simulation duration. At the worst scenarios, such as the instants of fault occurrence and clearance, two iterations are needed at the most. It can be concluded that the proposed method is proven to be effective in formulating the training set for the ANN-based equivalent.

For the test system, the ANN-based equivalent based on a FRNN is formed, as shown in Fig. 4.19. The inputs include the present and previous

voltage samples at bus i (i=131, 806, and 536), and the remaining inputs are the delayed feedbacks of the power injection predictions at the output side.

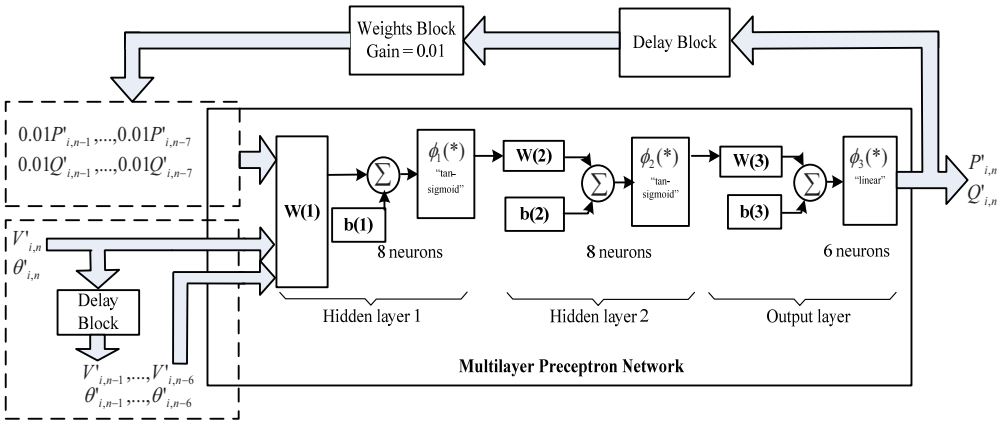

Fig. 4.19 The proposed ANN-based equivalent.

As shown in Fig. 4.19, a three-layer network, consisting of two hidden nonlinear layers and one linear layer, is used as the MLP network in the ANN-based equivalent. To make the entire FRNN numerically stable, a gain of 0.01 is applied to the feedbacks from the output side. In addition, the following pre-processing functions are used to avoid the potential saturation issues with the tan-sigmoid activation functions at layers 1 and 2:

$$\begin{cases} V'_{ANNi,n} = V_{ANNi,n}/3 \\ \theta'_{ANNi,n} = \theta_{ANNi,n}/3 \end{cases} \tag{4.43}$$

$$\begin{cases} P'_{ANNi,n} = P_{ANNi,n}/6 \\ Q'_{ANNi,n} = Q_{ANNi,n}/6 \end{cases} \tag{4.44}$$

where i is the boundary bus number (i=131, 806, and 536). The reduction ratio is determined based on extensive cases studies.

With the pre-processing functions in (4.44) and (4.45), the magnitudes of input and output signals are mapped to the unsaturated section of the tan-sigmoid activation function. After forming the pre-processed training data and opening the feedback loop in the FRNN, the LM routine in MATLAB [45] is deployed to optimize the unknown parameters in the equivalent neural network to simulate the input-and-output mapping stored in the training set. The mean square error (MSE) during the training process is shown in Fig. 4.20.

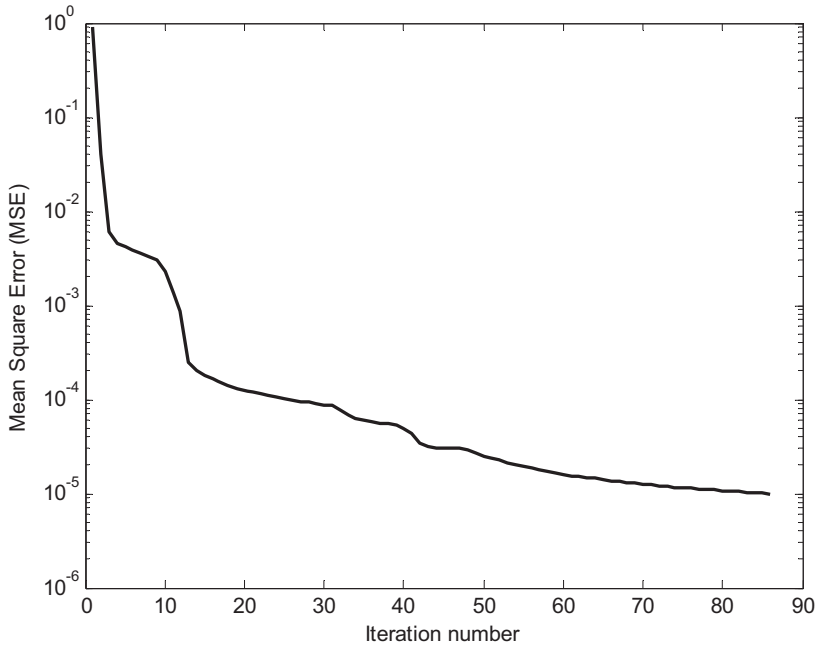

Fig. 4.20 MSE during the training process.

It is seen from Fig. 4.20 that the error decreases dramatically in the initial iterations. It reaches the tolerance of 10^{-5} at the 85^{th} iteration. On an Intel Core Duo Processor (3.16 GHz) PC with 3 GB of RAM, the entire training process takes approximately 129 s. It is to be noted that the number of the neurons at each layer need to be tuned cautiously to avoid the potential over-fitting problem. A trial-and-error method is used to determine the appropriate configuration of the

FRNN used. After being trained, the ANN-based equivalent is connected to the conventionally reduced system at the boundary buses, and the resultant hybrid reduced system is shown in Fig. 4.21.

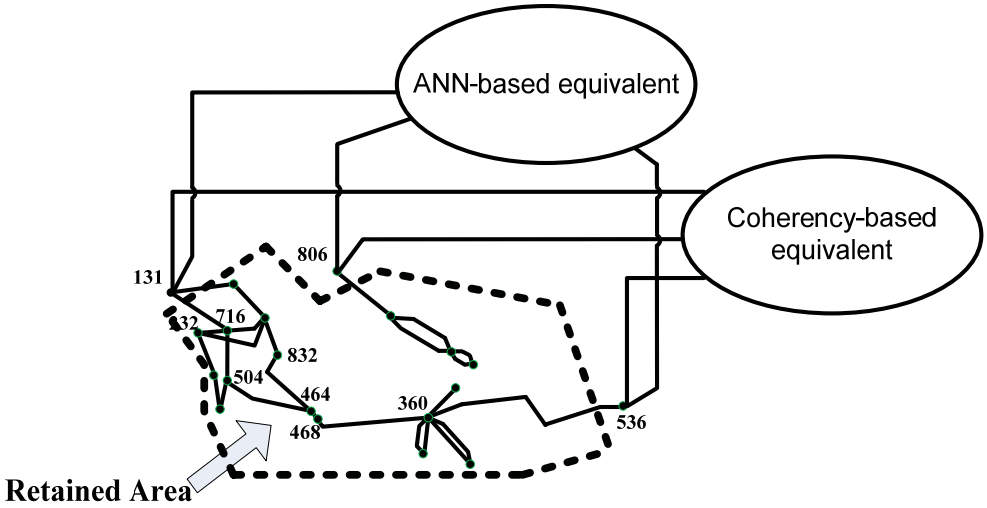

Fig. 4.21 Diagram of hybrid reduced system.

To validate the effectiveness of the proposed hybrid dynamic equivalent method in the improvement of equivalencing accuracy, the same contingency as in Case 2 is tested on the hybrid reduced system. The relative rotor angle response of generator 15 and the voltage response at bus 131 are shown in Fig. 4.22.

It can be seen from Fig. 4.22 that the mismatch between the full system and conventionally reduced system responses is well compensated by the ANN-based equivalent as expected. More accurate responses can be obtained in the hybrid reduced system throughout the entire simulation duration.

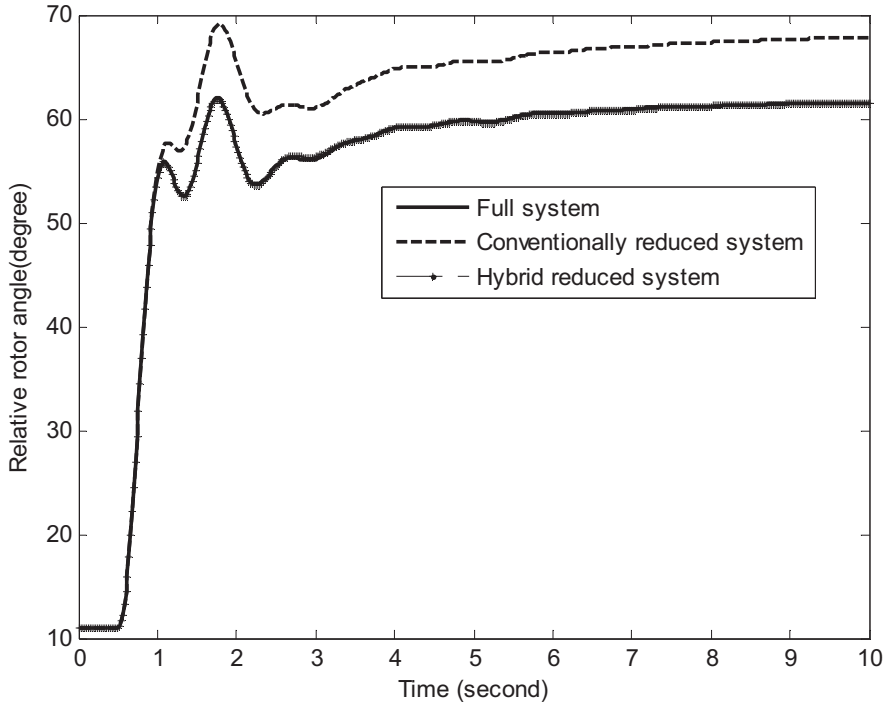

(a) Relative rotor angle response of generator 15

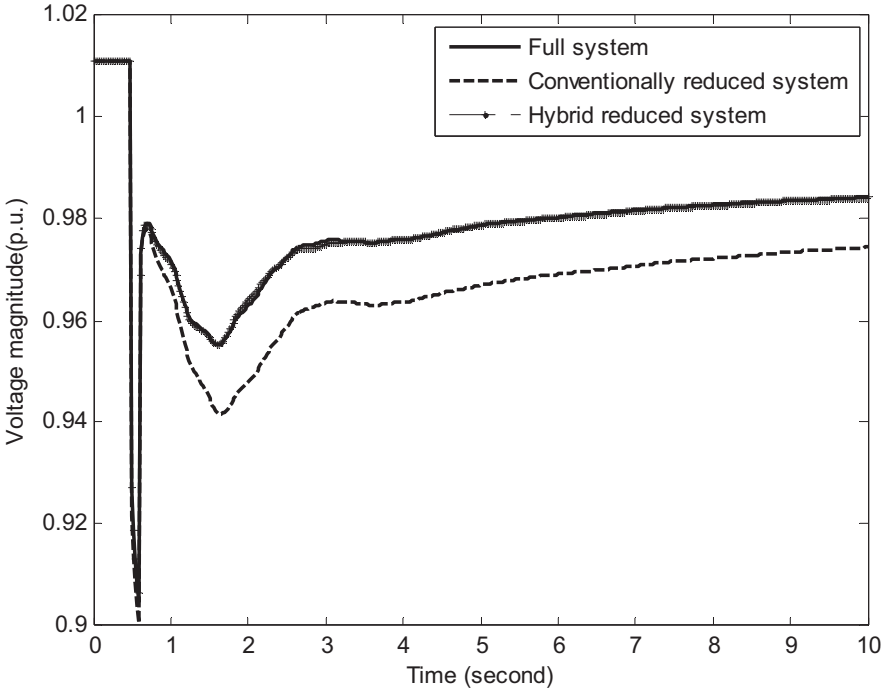

(b) Voltage response at bus 131

Fig. 4.22 Response comparison for Case 2.

For case 2, the RMSEs of the generators in the retained area are compared between the conventionally reduced system and the hybrid reduced system. The results are shown in Fig. 4.23.

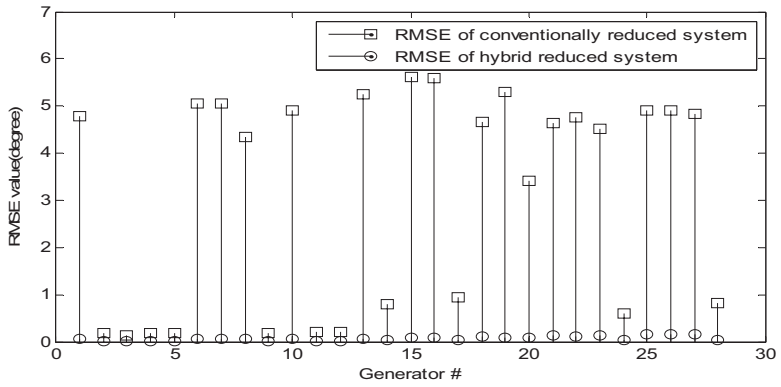

Fig. 4.23 RMSE comparison for Case 2.

It is observed from Fig. 4.23 that with the supplementary power injections provided by the ANN-based equivalent, the RMSEs decrease significantly for most of the retained generators. For all the training cases, the RMSE reductions brought by the hybrid reduced system from the conventionally reduced system are summarized in Table 4-3.

Table 4-3 Summary of RMSE reduction

Case #	Maximum RMSE reduction (deg.)	Minimum RMSE reduction (deg.)	Average RMSE reduction (deg.)
1	5.49	0.11	3.03
2	5.52	0.11	3.04
3	0.38	0.01	0.16
4	0.55	0.03	0.24
5	0.61	0.02	0.26
6	1.03	0.04	0.41

It is seen from Table 4-3 that the ANN-based equivalent can effectively improve the accuracy of the coherency-based equivalent formed in DYNRED.

However, its effectiveness varies in different cases. For a severe contingency, such as Case 2, the improvement is more significant. The execution time for simulating each training case is listed in Table 4-4 .

Table 4-4 Summary of the simulation execution time

Case #	Full syst. (s)	Hybrid reduced syst. (s)	% of full syst.
1	77.01	28.25	36.7%
2	77.28	28.85	37.3%
3	79.80	29.77	37.3%
4	86.49	31.88	36.9%
5	91.53	30.97	33.8%
6	96.16	33.40	34.7%

It is observed from Table 4-4 that significant time saving in simulating the contingencies of interest can be achieved using the hybrid reduced system. The reduction ratio for different cases varies from 33.8% to 37.3% on the same PC as described before. To validate the accuracy of the hybrid equivalent for the cases that are not included in the training set, the following new contingencies are tested:

- *Case 7*: a three-phase fault is applied on bus 360, and it is cleared after 0.12 s by tripping the line from bus 360 to bus 468.
- *Case 8*: a three-phase fault is applied on bus 504, and it is cleared after 0.10 s by tripping the line from bus 504 to bus 464.

It is seen that Case 7 is different from Case 1 and 2 in terms of the fault clearing time; while a new faulted bus is introduced in Case 8. For Case 7, the responses in the full system and reduced systems are shown in Fig. 4.24, and the RMSEs of the generator relative rotor angle responses are compared in Fig. 4.25.

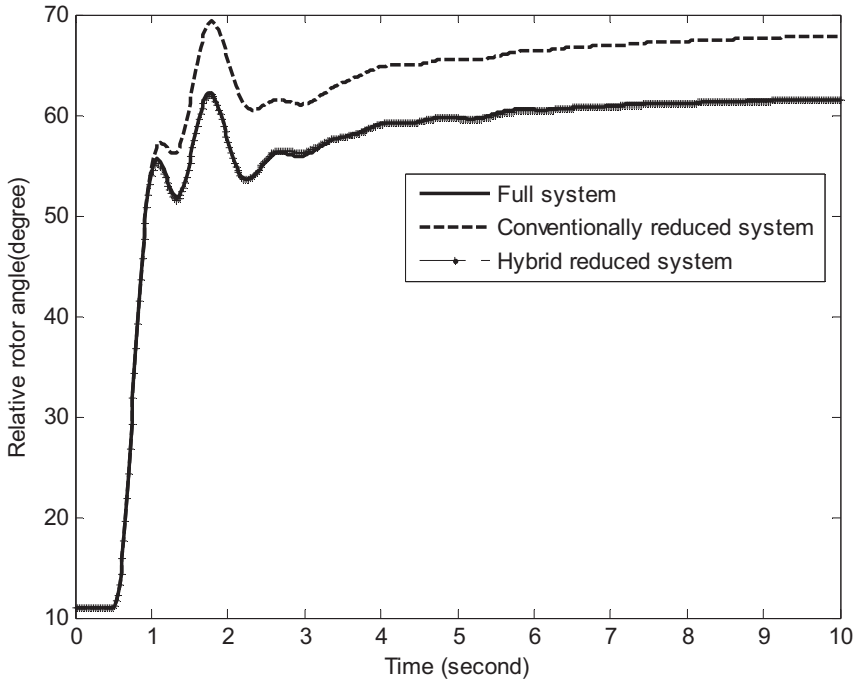

(a) Relative rotor angle response of generator 15

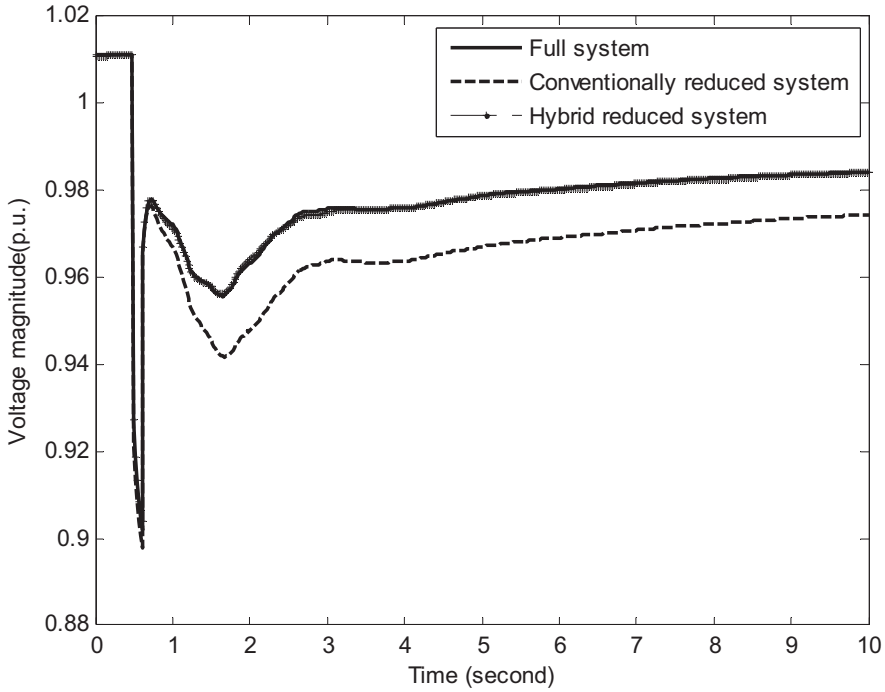

(b) Voltage response at bus 131

Fig. 4.24 Response comparison for Case 7.

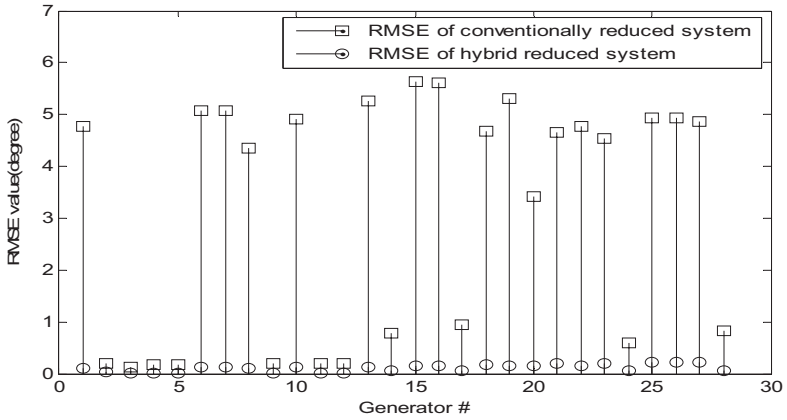

Fig. 4.25 RMSE comparison for Case7.

Similarly, for the untrained Case 8, the responses in the full system and the reduced systems are presented in Fig. 4.26. A comparison of the RMSEs in the conventionally reduced system and the hybrid reduced system is also given in Fig. 4.27.

It can be seen from Fig. 4.24 - Fig. 4.27 that for the disturbances not included in the training set (e.g. Case 7 and 8), the ANN-based equivalent is still able to generalize its input-and-output mapping from the most similar cases in the training set and achieve better equivalencing accuracy by providing essential power injection compensation to the conventionally reduced system. Because the generalization accuracy of a neural network is highly dependent on its training samples, the improvement of the ANN-based equivalent might not be significant for certain untrained cases. Once this issue occurs, including these inadequate cases into the training set would become necessary for practical implementation.

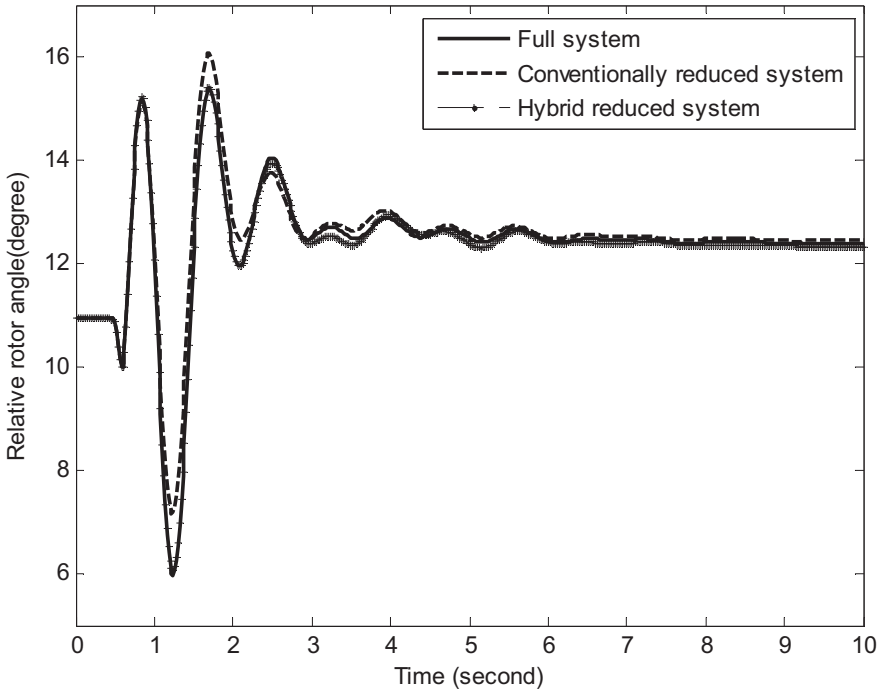

(a) Relative rotor angle response of generator 15

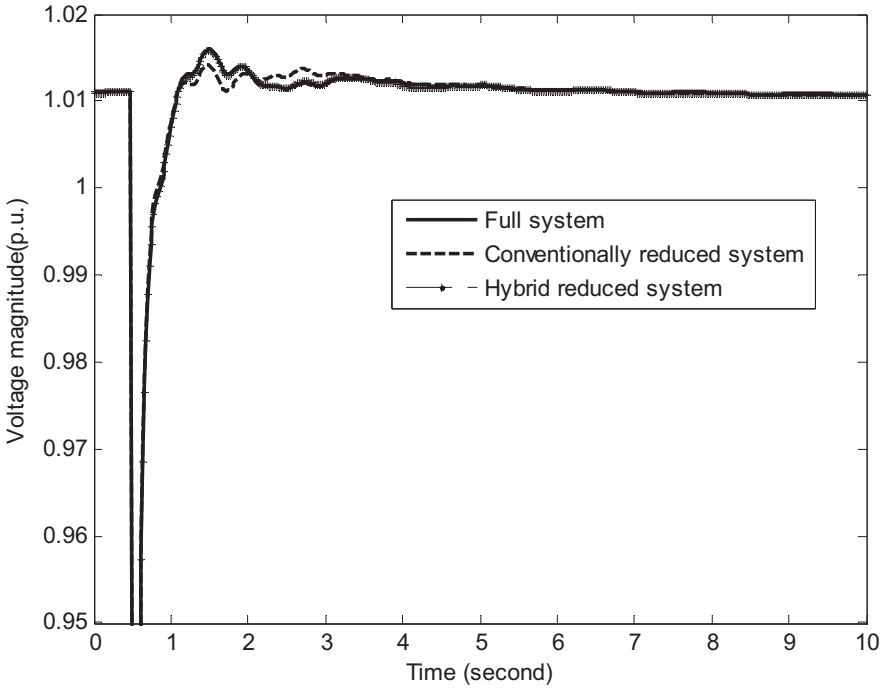

(b) Voltage response at bus 131

Fig. 4.26 Response comparison for Case 8.

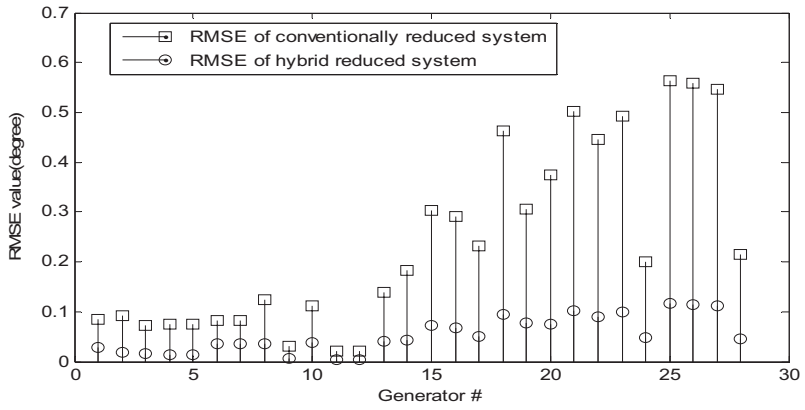

Fig. 4.27 RMSE comparison for Case 8.

4.7 Conclusion

In the hybrid dynamic equivalent model proposed in this chapter, the ANN-based equivalent works in conjunction with the coherency-based equivalent at all the buses on the retained area boundary. It is trained to compensate for the discrepancy between the full system and the conventionally reduced system formed in DYNRED. The proposed method is tested on a portion of the WECC system. The results indicate that the ANN-based equivalent can effectively compensate for the errors accumulated during the coherency identification and generator aggregation processes. Therefore, the hybrid dynamic equivalent can improve the accuracy of the coherency-based dynamic equivalent methodology that has been widely used in power industry. It is to be noted that the original boundary is formed based on the ownership within the test system. A well defined retained area as studied in Chapter 2 might be beneficial to the hybrid equivalent as it can improve the equivalencing accuracy of the coherency-based equivalent and reduce the amount of compensations provided by the ANN-based equivalent.

Chapter 5

CONCLUSIONS AND FUTURE WORK

5.1 Conclusions

Power system dynamic equivalents play a critical role in on-line DSA with the rapid expansion of modern electric power systems. To improve the feasibility of the conventional coherency-based dynamic equivalent, the following topics have been discussed thoroughly in this dissertation:

- A systemic method to determine an appropriate retained area boundary

In the proposed method, the PTDF-based criterion, the rotor acceleration-based criterion, and the mode participation-based criterion have been applied to identify the critical generators in the initial external area that have significant impacts on the dynamic performance of the study area. The identified generators are retained additionally, leading to the revised equivalent model. The proposed approach has been tested on the system representing the entire US/Canada eastern interconnection. The results show that the proposed algorithm is capable of identifying the critical generators in forming the buffer area and achieving a good comprise between the equivalencing accuracy and system complexity.

- An efficient method to trace generator slow coherency behavior and to adjust retained area boundary for operating condition changes

A systematic approach based on the eigen-sensitivity is proposed to evaluate the varying patterns of generator slow coherency as system operating condition changes. The changes in load, generation, and network topology have been considered. The critical generators in the initial external area that become

slowly coherent with the initial study area are identified and retained in forming a new equivalent system. The proposed approach has been applied to a portion of the WECC system. The studies show that the system topology change could have more impacts on the generator slow coherency behavior than load or generation change. In certain cases, including the identified critical generators into study area is beneficial to the improvement of equivalencing accuracy.

- A novel hybrid dynamic equivalent method

The concept of a novel hybrid dynamic equivalent method has been developed. In the proposed model, the coherency-based equivalent still plays a dominant role, and the ANN-based equivalent is only used to capture additional dynamic characteristics that have not been represented in the conventionally reduced system. The methods to build the training set, to form an appropriate network structure, and to integrate the ANN-based equivalent with the existing transient simulation software packages have been presented in detail. The test on a portion of the WECC system indicates that the ANN-based equivalent can provide desirable compensations to the coherency-based equivalent for improved equivalencing accuracy.

5.2 Contributions

As an innovative study on improving the feasibility of coherency-based dynamic equivalent, the research presented in this dissertation has made the following contributions:

Firstly, a systematic procedure to identify the critical generators in determining an appropriate retained area boundary has been innovatively

developed. It is to be noted that the criteria, such as PTDF and mode participation factor, can be readily accessed in various commercial software packages (e.g. PowerWorld, PSS/E, DSA Tools); while the rotor acceleration during fault duration can be easily calculated without the need of integrating the DAEs of the original full system as in a time-domain simulation.

Secondly, the eigensensitivity-based method has been innovatively used to trace the change in generator slow coherency patterns. Instead of computing the slow coherency from scratch for a new operating condition, the proposed method is proven to be effective in tracing the generator slow coherency after either the generation level, load level, or system topology is changed. The advantage of the proposed method in terms of computational time saving for a changed operating condition is significant.

Thirdly, a novel concept of hybrid dynamic equivalent has been proposed and developed. This study is different from the other researches on the same subject in the fact that the proposed ANN-based equivalent works in conjunction with the conventional equivalent model. Therefore, the detrimental impacts of a poorly trained ANN-based equivalent on the reduced system can be limited. In addition, the trajectory sensitivity-based method to determine the training set for ANN-based equivalent and the method to simulate the resultant hybrid system are proven to be efficient and effective.

5.3 Future Work

To further improve the feasibility of the proposed methods, work focusing on the following aspects need to be conducted in the future:

Firstly, other criteria that can be applied in a near real-time setting to evaluate the necessity of adjusting the retained area need to be investigated. For better equivalencing accuracy, new coherent generator aggregation methodologies that take into account the effects of exciters, governors, and PSS also need to be developed

Secondly, because the choice of modes affects the evaluation results of generator slow coherency, an approach to identify the critical modes needs to be investigated. For practical implementation, the proposed approach to trace the generator slow coherency changes needs to be modified in such a manner that an efficient mechanism to support large data structures and to manipulate large volumes of data is provided for large-scale power systems.

Thirdly, in formulating the training set and simulating the hybrid reduced system, the integration time step has to be fixed. To achieve adequate accuracy through the entire simulation duration, a small step is of necessity. This is true especially during the interval of system disturbance. This limitation results in low computational efficiency when the scale of the hybrid system is large and the simulation duration is considerably long. To address this drawback, a faulted network and a post-fault neural network with different sampling time intervals need to be designed. The technique to transit seamlessly between these two networks in a time-domain simulation also needs to be studied.

Last but not least, other types of neural networks need to be tested for the ANN-based equivalent. An echo state network [46] can be a good candidate because it includes multi-direction connections among the neurons at different

layers, resulting in better functionality of capturing the input-and-output mapping presented in the training set. A study using the voltage response measured by PMUs as the voltage reference in determining the required power injections of the ANN-based equivalent can also be considered for the application of the proposed hybrid dynamic equivalents for on-line DSA. Correspondingly, efficient training methods in the on-line setting need to be developed in the future.

REFERENCES

[1] S. T. Y. Lee, and F. C. Schweppe, "Distance measures and coherency recognition for transient stability equivalents," *IEEE Trans. Power App. Syst*., vol. PAS-92, no. 5, pp. 1550 – 1557, Sept. 1973.

[2] R. Billinton, and P. Wang, "Deregulated power system planning using a reliability network equivalent technique," in *Proc. 1999 IEEE Gener. Transm. Distrib*., vol. 153, no. 6, pp. 25 – 30.

[3] R. Podmore, "Identification of coherent generators for dynamic equivalents," *IEEE Trans. Power App. Syst*., vol. PAS-97, pp. 1344 – 1354, July 1978.

[4] R. Nath, S. S. Lamba, and K. S. P. Rao, "Coherency based system decomposition into study and external areas using weak coupling," *IEEE Trans. Power App. Syst*., vol. PAS-104, pp. 1443 – 1449, June 1985.

[5] L. Wang, M. Klein, S. Yirga, and P. Kundur, "Dynamic reduction of large power systems for stability studies," *IEEE Trans. on Power Syst.*, vol. 12, no. 2, pp. 889 – 895, May 1997.

[6] J. H. Chow, J. R. Winkelman, M. A. Pai, and P. W. Sauer, "Model reduction and energy function analysis of power system using singular perturbation techniques," In *Proc. 25th IEEE Conf. on Decision and Control*, pp.1206 – 1211, 1986.

[7] P. Kundur, G. J. Rogers, D. Y. Wong, J. Ottevangers, and L. Wang, "Dynamic reduction," EPRI TR-102234 Project 2447-01, 1993.

[8] S. K. Joo, C. C. Liu, L. E. Jones, and J. W. Choe, "Coherency and aggregation techniques incorporating rotor and voltage dynamics," *IEEE Trans. on Power Syst.*, vol. 19, no. 2, pp.1068 – 1075, May 2004

[9] R. Podmore, and A. Germond, "Development of dynamic equivalent for transient stability studies," EPRI EL – 456 Project 763, 1977.

[10] M. L. Ourari, L. A. Dessaint, and V. Q. Do, "Dynamic equivalent modeling of large power systems using structure preservation technique," *IEEE Trans. on Power Syst.*, vol.21, no.3, pp. 1284 – 1295, Aug. 2006.

[11] P. Kundur, G. J. Rogers, D. Y. Wong, J. Ottevangers, and L. Wang, "Dynamic reduction, " EPRI, TR – 102234 Project 2447 – 01, 1993.

[12] W. W. Price, A. W. Hargrave, B. J. Hurysz, J. H. Chow, and P. M. Hirsch, "Large-scale system testing of a power system dynamic equivalencing program," *IEEE Trans. Power Syst*., vol. 13, no. 3, pp. 768 – 773, Aug. 1998.

[13] F. Ma, and V. Vittal, "Right-sized power system dynamic equivalents for power system operation," to appear in *IEEE Trans. on Power Syst.*, TPWRS.2011.2138725.

[14] F. Ma, X. Luo, and V. Vittal, "Application of dynamic equivalencing in large-scale power systems," to appear in *Proc. 2011 IEEE PES General Meeting*, Paper no. 2011GM0804.

[15] V. S. S. Vankayala, and N. D. Rao, "Artificial neural networks and their applications to power system - a bibliographical survey," *Electric Power System Research*, vol. 28, no. 1, pp. 67 –79, Oct. 1993.

[16] D. P. Kothari, "Application of neural networks to power systems," *in 2000 IEEE Proc. Int. Conf. on Industrial Technology*, vol. 2, pp. 621 – 626.

[17] A. M. Stankovic, A. T. Saric, and M. Milosevic, "Identification of non-parametric dynamic power system equivalents with artificial neural networks," *IEEE Trans. on Power Syst.*, vol. 18, no. 4, pp. 1478 – 1486 , Nov. 2003.

[18] A. M. Stankovic, and A. T. Saric, "Transient power system analysis with measurement-based gray box and hybrid dynamic equivalents," *IEEE Trans. on Power Syst.*, vol. 19, no. 1, pp.445 – 462 , Feb. 2004.

[19] E. D. Tuglie, L. Guida, F. Torelli, D. Lucarella, M. Pozzi, and G. Vimercait, "Identification of dynamic voltage-current power system equivalents through artificial neural networks," in *Proc. 2004 Bulk Power System Dynamics and Control–VI*, pp. 220 – 226.

[20] H. Shakouri, and HH. R. Radmanesh, "Identification of a continuous time nonlinear state space model for the external power system dynamic equivalent by neural networks," *Electrical Power and Energy System*, vol. 31, no. 7-8, pp. 334 – 344, 2009.

[21] Y. Liang, X. Lin, A. M. Gole, and M. Yu, "Improved coherency-based wide-band equivalents for real-time digital simulators," *IEEE Trans. on Power Syst*., vol. 26, no. 3, pp. 1410 – 1417, Aug. 2011.

[22] L. Wang, and G. Zhang, "DYNRED enhancement project," EPRI Tech. Rep. for Software Product ID # 1020268, 2010.

[23] X. Cheng, and T. J. Overbye, "PTDF-based power system equivalents," *IEEE Trans. on Power Syst.*, vol. 20, no. 4, pp. 1868 – 1876, Sept. 2005.

[24] P. Kundur, Power system stability and control, New York: McGraw-Hill, 1994.

[25] X. M. Wang, V. Vittal, and G. T. Heydt, "Tracing generator coherency indices using the continuation method: a novel approach," *IEEE Trans. on Power Syst.*, vol. 20, no. 3, pp. 1510 – 1518, Aug. 2005.

[26] Y. K. Wu, "A novel algorithm for ATC calculations and applications in deregulated electricity markets," *Electrical Power and Energy Systems*, vol. 29, no. 10, pp. 810 – 821, Dec. 2007.

[27] A. A. Fouad et al, "Transient stability margin as a tool for dynamic security assessment," EPRI EL-1755 Project 1355-3, 1981.

[28] M. Jankovic, "Exact nth derivatives of eigenvalues and eigenvectors," *Journal of Guidance, Control, and Dynamics*, vol. 17, no. 1, pp. 136 – 144, Jan.- Feb. 1994.

[29] X. Wang, and V. Vittal, "System islanding using minimal cutsets with minimum net flow, " *in Proc. 2004 IEEE PES Power System Conf. Expo.*, London, vol. 1, pp. 379 – 384.

[30] G. Xu, "Controlled islanding algorithms and demonstrations on the WECC system," Ph.D. dissertation, School of electrical, computer, and energy engineering, Arizona State University, 2010.

[31] A. M. Azmy, I. Erlich, and P. Sowa, "Artificial neural network-based dynamic equivalents for distribution systems containing active sources," in *Proc. 2004 IEEE Gener. Transm. Distrib.*, vol. 151, no. 6, pp. 681– 688.

[32] T. B. Nguyen, and M. A. Pai, "Dynamic security-constrained rescheduling of power systems using trajectory sensitivities," *IEEE Trans. on Power Syst*., vol. 18, no.2, pp. 848 – 854, May 2003.

[33] A. Zamora-Cardenas, and C. R. Fuerte-Esquivel, "Multi-parameter trajectory sensitivity approach for location of series-connected controllers to enhance power system transient stability," *Electric Power Systems Research*, vol. 80, no. 9, pp. 1096 – 1103, Sept. 2010.

[34] F. Milano, "An open source power system analysis toolbox," *IEEE Trans. on Power Syst*., vol. 20, no. 3, pp. 1199 – 1206, Aug. 2005.

[35] A. H. Alavi, A. H. Gandomi, M. Gandomi, and S. S. Sadat Hosseini, "Prediction of maximum dry density and optimum moisture content of stabilized soil using RBF neural networks," *The IES Journal Part A: Civil & Structural Engineering*, vol. 2, no. 2, pp. 98 – 106, May 2009.

[36] J. He, and O. P. Malik, "An adaptive power system stabilizer based on recurrent neural networks," *IEEE Trans. on Power Syst.*, vol. 12, no. 4, pp.413 – 418 , Dec. 1997.

[37] T. G. Barbounis, J. B. Theocharis, M. C. Alexiadis, and P. S. Dokopoulos, "Long-term wind speed and power forecasting using local recurrent neural network models," *IEEE Trans. on Energy Conversion*, vol. 12, no. 1, pp. 273 – 284 , March 2006.

[38] A. Yona, T. Senjyu, and T. Funabashi, "Application of recurrent neural network to short-term-ahead generating power forecasting for photovoltaic system," In *Proc. 2007 IEEE PSE General Meeting*, pp.1 – 6.

[39] J. Vermaak, and E. C. Botha, "Recurrent neural networks for short-term load forecasting," *IEEE Trans. on Power Syst*., vol. 13, no. 1, pp. 126 – 132 , Feb. 1998.

[40] B. K. Bose, "Neural network applications in power electronics and motor drives - an introduction and perspective," *IEEE Trans. on Industrial Electronics*, vol. 54, no. 1, pp. 14 – 33, Feb. 2007.

[41] S. S. Haykin, Neural Networks: A Comprehensive Foundation. Englewood Cliffs, NJ: Prentice-Hall, 1999.

[42] P. J. Angeline, G. M. Saunders, and J. B. Pollack, "An evolutionary algorithm that constructs recurrent neural networks," *IEEE Trans. on Neural Networks*, vol. 5, no. 1, pp.54 – 65, Jan. 1994.

[43] G. V. Puskorius, and L. A. Feldkamp, "Neurocontrol of nonlinear dynamic systems with Kalman filter trained recurrent networks", *IEEE Trans. on Neural Networks*, vol. 5, no. 2, pp. 279 – 297, Mar. 1994.

[44] C. F. Juang, "A hybrid of genetic algorithm and particle swarm optimization for recurrent network design," *IEEE Trans. on System, Man, and Cybernetics*, vol. 32, no. 2, pp. 997 – 1006, April 2004.

[45] The Math Works Inc, Neural Network Toolbox for use with MATLAB User's Guide, Version7, 2010.

[46] G. K. Venayagamoorthy, "Online design of an echo state network based wide area monitor for a multimacine power system," *Neural Networks*, vol. 20, no. 3, pp. 404 – 413, April 2007.